AD-A192 345 NUMERICAL ASSESSMENT OF ROCKBURSTING(U) AGBABIAN ASSOCIATES EL SEGUNDO CA J P BARDET 27 MAY 87 R-8618-6171 DNA-TR-87-158 DNA001-86-C-0059 1/2

UNCLASSIFIED F/G 8/9 NL

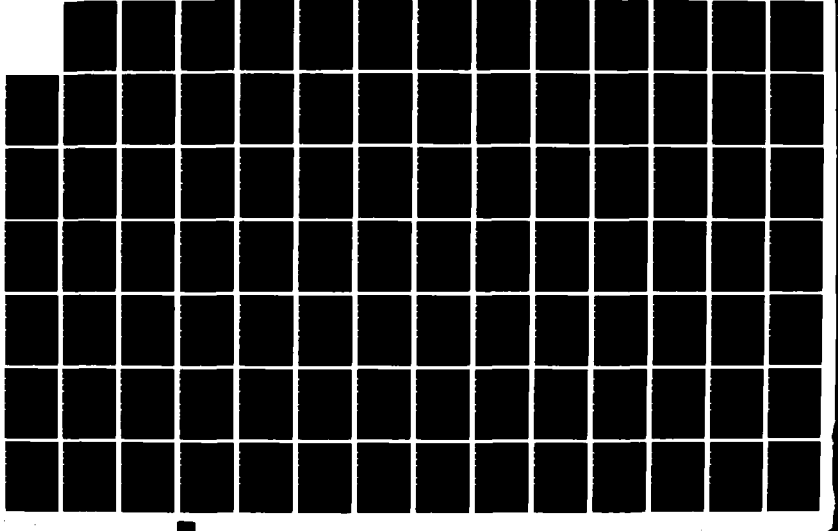

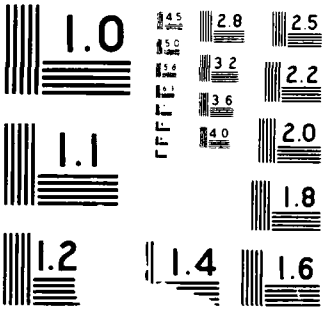
1.0
1.1
1.2
1.4
1.6
1.8
2.0
2.2
2.5
2.8
3.2
3.6
4.0
4.5
5.0

(4)

DNA-TR-87-158

NUMERICAL ASSESSMENT OF ROCKBURSTING

J.P.Bardet
Agbabian Associates
250 North Nash Street
El Segundo, CA 90245-0956

27 May 1987

Technical Report

CONTRACT No. DNA 001-86-C-0059

Approved for public release;
distribution is unlimited.

THIS WORK WAS SPONSORED BY THE DEFENSE NUCLEAR AGENCY
UNDER RDT&E RMC CODE B3410854662 RS RC 00037 25904D.

Prepared for
Director
DEFENSE NUCLEAR AGENCY
Washington, DC 20305-1000

Destroy this report when it is no longer needed. Do not return to sender.

PLEASE NOTIFY THE DEFENSE NUCLEAR AGENCY ATTN: TITL, WASHINGTON, DC 20305 1000, IF YOUR ADDRESS IS INCORRECT, IF YOU WISH IT DELETED FROM THE DISTRIBUTION LIST, OR IF THE ADDRESSEE IS NO LONGER EMPLOYED BY YOUR ORGANIZATION.

REPORT DOCUMENTATION PAGE

Form Approved
OMB No 0704-0188
Exp Date Jun 30 1986

1a REPORT SECURITY CLASSIFICATION UNCLASSIFIED	1b RESTRICTIVE MARKINGS
2a SECURITY CLASSIFICATION AUTHORITY N/A since Unclassified	3 DISTRIBUTION/AVAILABILITY OF REPORT Approved for public release; distribution is unlimited.
2b DECLASSIFICATION/DOWNGRADING SCHEDULE N/A since Unclassified	
4 PERFORMING ORGANIZATION REPORT NUMBER(S) R-8618-6171	5 MONITORING ORGANIZATION REPORT NUMBER(S) DNA-TR-87-158
6a NAME OF PERFORMING ORGANIZATION Agbabian Associates 6b OFFICE SYMBOL (If applicable)	7a NAME OF MONITORING ORGANIZATION Director Defense Nuclear Agency
6c ADDRESS (City, State, and ZIP Code) 250 North Nash Street El Segundo, CA 90245-0956	7b ADDRESS (City, State, and ZIP Code) Washington, DC 20305-1000
8a NAME OF FUNDING/SPONSORING ORGANIZATION 8b OFFICE SYMBOL (If applicable) SPED/Reed	9 PROCUREMENT INSTRUMENT IDENTIFICATION NUMBER DNA 001-86-C-0059
8c ADDRESS (City, State, and ZIP Code)	10 SOURCE OF FUNDING NUMBERS PROGRAM ELEMENT NO: 62715H; PROJECT NO: RS; TASK NO: RC; WORK UNIT ACCESSION NO: DH009111

11 TITLE (Include Security Classification)
NUMERICAL ASSESSMENT OF ROCKBURSTING

12 PERSONAL AUTHOR(S)
Bardet, J.P.

13a TYPE OF REPORT	13b TIME COVERED	14 DATE OF REPORT (Year, Month, Day)	15 PAGE COUNT
Technical	FROM 860210 TO 861231	870527	140

16 SUPPLEMENTARY NOTATION
This work was sponsored by the Defense Nuclear Agency under RDT&E RMC Code B3410854662 RS RC 00037 25904D.

17 COSATI CODES		
FIELD	GROUP	SUB-GROUP
12	3	
19	9	

18 SUBJECT TERMS (Continue on reverse if necessary and identify by block number)
Rockbursting; Numerical Instability; Surface Instability; Bifurcation

19 ABSTRACT (Continue on reverse if necessary and identify by block number)

A numerical approach for analyzing rockbursting phenomenon as a surface instability has been developed. Computer program modules that can be incorporated into general purpose nonlinear finite element codes have been created. The numerical approach has been successfully applied for a simple case of the wedge test.

20 DISTRIBUTION/AVAILABILITY OF ABSTRACT ☐ UNCLASSIFIED/UNLIMITED ☒ SAME AS RPT ☐ DTIC USERS	21 ABSTRACT SECURITY CLASSIFICATION UNCLASSIFIED
22a NAME OF RESPONSIBLE INDIVIDUAL Sandra E. Young	22b TELEPHONE (Include Area Code) (202) 325-7042 22c OFFICE SYMBOL DNA/CSTI

DD FORM 1473, 84 MAR 83 APR edition may be used until exhausted
All other editions are obsolete

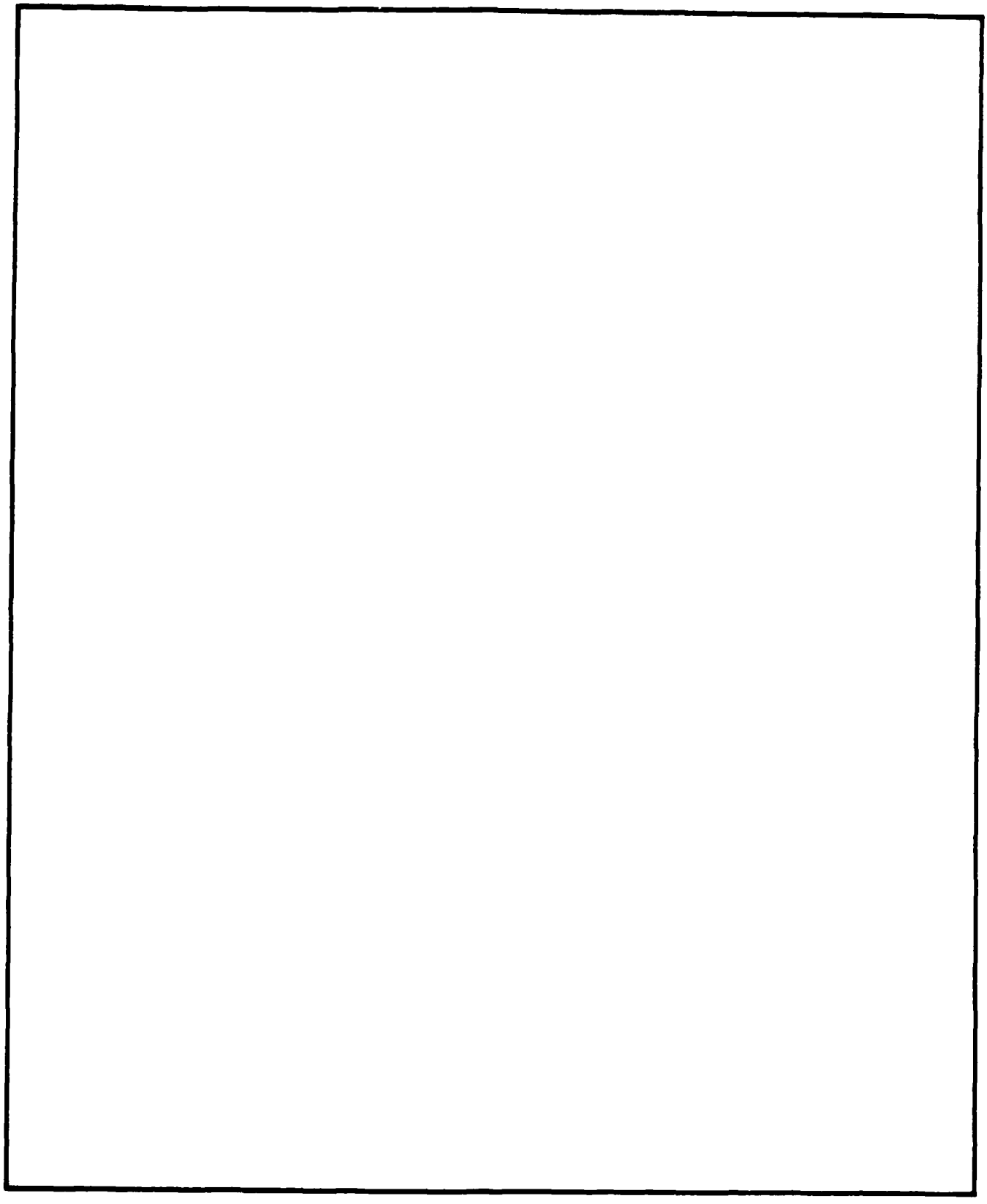

PREFACE

This technical report was prepared by Agbabian Associates under Contract No. DNA 001-87-C-0059 with the Defense Nuclear Agency. The objective of the contract is to develop numerical techniques for analyzing rockbursting in underground excavations.

Project Monitor for the Defense Nuclear Agency was Capt. Michael Reed. Project Manager for Agbabian Associates was D.P. Reddy and Principal Investigator was J.P. Bardet.

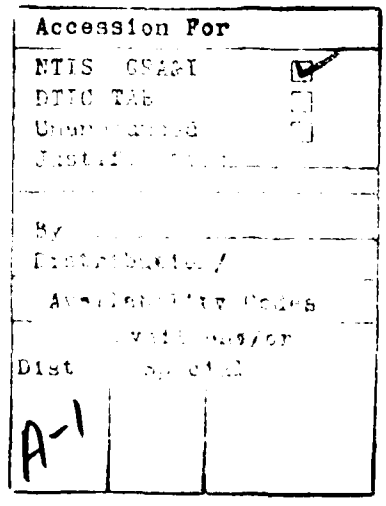

Conversion factors for U.S. customary to metric (SI) units of measurement.

To Convert From	To	Multiply By
angstrom	meters (m)	1.000 000 X E -10
atmosphere (normal)	kilo pascal (kPa)	1.013 25 X E +2
bar	kilo pascal (kPa)	1.000 000 X E +2
barn	meter^2 (m^2)	1.000 000 X E -28
§ritish thermal unit (thermochemical)	joule (J)	1.054 350 X E +3
cal (thermochemical)/cm^2§	mega joule/m^2 (MJ/m^2)	4.184 000 X E -2
calorie (thermochemical)§	joule (J)	4.184 000
calorie (thermochemical)/g§	joule per kilogram (J/kg)*	4.184 000 X E +3
curie§	giga becquerel (GBq)+	3.700 000 X E +1
degree Celsius‡	degree kelvin (K)	$t_K = t°_C + 273.15$
degree (angle)	radian (rad)	1.745 329 X E -2
degree Fahrenheit	degree kelvin (K)	$t_K = (t°_F + 459.67)/1.8$
electron volt§	joule (J)	1.602 19 X E -19
erg§	joule (J)	1.000 000 X E -7
erg/second	watt (W)	1.000 000 X E -7
foot	meter (m)	3.048 000 X E -1
foot-pound-force	joule (J)	1.355 818
gallon (U.S. liquid)	meter^3 (m^3)	3.785 412 X E -3
inch	meter (m)	2.540 000 X E -2
jerk	joule (J)	1.000 000 X E +9
joule/kilogram (J/kg) (radiation dose absorbed)§	gray (Gy)*	1.000 000
kilotons§	terajoules	4.183
kip (1000 lbf)	newton (N)	4.448 222 X E +3
kip/inch^2 (ksi)	kilo pascal (kPa)	6.894 757 X E +3
ktap	newton-second/m^2 ($N-s/m^2$)	1.000 000 X E +2
micron	meter (m)	1.000 000 X E -6
mil	meter (m)	2.540 000 X E -5
mile (international)	meter (m)	1.609 344 X E +3
ounce	kilogram (kg)	2.834 952 X E -2
pound-force (lbf avoirdupois)	newton (N)	4.448 222
pound-force inch	newton-meter (N·m)	1.129 848 X E -1
pound-force/inch	newton/meter (N/m)	1.751 268 X E +2
pound-force/foot^2	kilo pascal (kPa)	4 788 026 X E -2
pound-force/inch^2 (psi)	kilo pascal (kPa)	6.894 757
pound-mass (lbm avoirdupois)	kilogram (kg)	4.535 924 X E -1
pound-mass-foot^2 (moment of inertia)	kilogram-meter^2 ($kg·m^2$)	4.214 011 X E -2
pound-mass/foot^3	kilogram-meter^3 (kg/m^3)	1.601 846 X E +1
rad (radiation dose absorbed)§	gray (Gy)*	1.000 000 X E -2
roentgen§	coulomb/kilogram (C/kg)	2.579 760 X E -4
shake	second (s)	1.000 000 X E -8
slug	kilogram (kg)	1.459 390 X E +1
torr (mm Hg, 0° C)	kilo pascal (kPa)	1.333 22 X E -1

*The gray (Gy) is the accepted SI unit equivalent to the energy imparted by ionizing radiation to a mass of energy corresponding to one joule/kilogram.
+The becquerel (Bq) is the SI unit of radioactivity; 1 Bq = 1 event/s.
‡Temperature may be reported in degree Celsius as well as degree kelvin.
§These units should not be converted in DNA technical reports; however, a parenthetical conversion is permitted at the author's discretion.

TABLE OF CONTENTS

TABLE OF CONTENTS (CONTINUED)

LIST OF ILLUSTRATIONS

LIST OF ILLUSTRATIONS (CONTINUED)

LIST OF ILLUSTRATIONS (CONTINUED)

LIST OF ILLUSTRATIONS (CONTINUED)

LIST OF ILLUSTRATIONS (CONCLUDED)

LIST OF TABLES

SECTION 1

INTRODUCTION

1.1 OBJECTIVES OF WORK.

This report documents the results of an investigation with the long term objective of developing a general approach for analyzing rockbursting in underground excavations. Specifically, the objective of this project was to assess the applicability of finite element techniques to the problem of rockbursting. Rockbursting was to be analyzed as a surface instability by applying numerical stability techniques similar to those used to address the buckling problems of Structural Dynamics. A major objective of this investigation was to assess the applicability of finite element methods in describing surface instability, which has been done for structures such as shells and truss frames but not for the bulkier material mass encountered in underground excavations. To achieve this objective, four tasks were defined as follows:

Task 1 - Develop computer program modules which can be used in finite element codes to analyze the problem of rockbursting as a surface instability of underground excavations.

Task 2 - Validate the application of the numerical approach to rockbursting by performing a stability analysis of a simple boundary value problem - the wedge test.

Task 3 - Investigate the influence of the material modelling on the critical loads during the wedge test.

Task 4 - Examine how much surface instability is influenced by the friction at the boundaries on the wedge test.

It is to be noted here that the first task forms the major portion of the overall project. The work under this task consisted of developing computer program modules that can be used in general purpose nonlinear finite element programs to analyze the surface instability of underground excavations. The objective of the second, third and fourth tasks was to assess the applicability of our numerical approach in the case of a simple boundary value problem. The numerical analysis had to be calibrated for a simple boundary value problem before extending it to the complex geometries and material properties encountered in the case of real excavations. The calibration test chosen is a plane strain compression of rock sample. It will be referred to as the wedge test. During the second task, the program modules developed in the first task are used to obtain numerical results in the particular case of the wedge test. The performance of these finite element modules are tested by comparing their results with analytical results or other simpler numerical solutions. These additional results were obtained by using the program BIF, which was especially written to carry out the parametric study under the third task. The parametric study consisted of investigating the influence of the parameters of various constitutive equations on the buckling load of the wedge test. The fourth and last task was to investigate how much surface instability was influenced by the introduction of friction forces at the boundaries of the wedge test.

The numerical method which has been developed in this report has only been applied to analyze surface instability of the wedge test but not of real excavations. The extension of the method to real excavations, which are more complex boundary value problems, is the long term objective of the project. This extension will be the object of future research.

1.2 REPORT ORGANIZATION.

The main body of this report is comprised of 5 major sections covering respectively

1. the definition and past work on rockbursting and surface instability,
2. the finite element techniques used to describe the phenomenon of surface instability,
3. the numerical results obtained in the particular case of the wedge test,
4. the influence of material modeling on surface instability, and
5. the influence of friction boundary conditions on surface instability.

Mathematical derivations have been documented in appendices.

1.3 DEFINITION OF ROCKBURSTING.

The term rockburst is used to designate a violent failure of rock which is sometime experienced in deep underground excavations. It involves a rapid convergence and oscillation of the excavation walls, followed by slabbing and failure of the rock immediately adjacent to the excavation (Ortlepp, 1978). This violent release of energy has been observed on a scale ranging from the expulsion of small fragment of rock to major collapse of the excavation. It is often observed to follow enlargement of the cavity by blasting. Rockburst appears to be more frequent in rock which are hard and brittle.

The nature and the circumstances accompanying this phenomenon suggest that underground excavations in hard rock subject to dynamic loading caused by nuclear explosion are prone to rockbursting. In mining operations the mitigation of rock burst relies on designing the layout of the mine excavation and the

sequence of extraction in order to reduce as much as possible the vertical stress concentration around the mine (method of energy release rate, Jaeger and Cook, 1977, Salamon, 1974). Although the method provides a practical design tool for reducing the hazards of rockburst, it does not provide a mean of calculating whether rockburst will occur or not.

1.4 PAST WORK ON ROCKBURSTING.

Several phenomenological models have been proposed for explaining rockbursting phenomena. They are based upon limiting static equilibrium, nonlinear elasticity, strain-softening material, unstable propagation of pre-existing cracks, and finally surface instability. Lippman, 1978, Avershin et al., 1972, examine the static equilibrium of rock block adjacent to the excavation. The rockburst occurs in circumstances where the resisting forces do not balance the lateral forces tending to propel the block inside the cavity. Freudenthal, 1977, use nonlinear elasticity (hyperelasticity) to account for shear induced volume expansion. He considered that rockburst and spalling of the opening walls are caused by crack propagation associated with the tensile stress around the excavation. Salamon, 1974, and Pietruszczak and Mroz, 1980, Pariseau, 1979, characterize the rock as a strain-softening material. Instability becomes possible once the rock has experienced its peak strength. This mechanism can however be refuted on the ground that the softening observed in compression of brittle rock specimen is test dependent and is always associated with localized failure mechanisms (Drescher and Vardoulakis, 1982). Nemat-Nasser and Horii, 1982, analyze rock bursting as buckling of slabs. The slabs become detached from the rock by tensile extension, parallel to the free surface of pre-existing cracks, which are caused by far-field compressive

stress. Finally, Vardoulakis, 1984, uses the theory of bifurcation to analyze rockburst as surface instability.

1.5 PAST WORK ON SURFACE INSTABILITY.

The pioneering work on surface instability was carried out by Biot, 1965, who examined the half-plane problem with incompressible isotropic and anisotropic elastic material. A simple example of the surface instability treated by Biot in 1965 is summarized in Appendix A. In this example, Biot showed how the elastic half-space looses its rigidity for some value of compressive stress τ_1, and that this loss of rigidity corresponds to the phenomenon of surface buckling or surface instability. The buckling modes of the half-space are surface waves, the amplitude of which decays rapidly with depth. Hutchinson and Tvergaard, 1980, extended Biot's results for elastoplastic materials. They noted that the existence of surface buckling strongly depends on the type of plasticity which is employed to describe material behavior. The instability was found to occur at low loads for solids characterized by a deformation theory of plasticity and at high and unrealistic loads for solids characterized by the flow theory of plasticity. Vardoulakis, 1984, basing his analysis on a deformation of plasticity showed that the bifurcation load marks the beginning of dynamic instable conditions and that the existence of surface buckling is related to the ratio of the tensile over the compressive strength. This ratio can be used as a measure of the brittleness of the rock; the smaller the ratio, the more brittle the rock is. Horii and Nemat-Nasser, 1982, departing from the assumption of incompressibility made in the previous investigations, introduced dilatancy and showed that the inclusion of this material property reduces the magnitude of the bifurcation load. Horii and Nemat-Nasser also noted that the occurrence of

surface instability could be sensitive to the existence of a non-coaxiality parameter in the constitutive equation.

SECTION 2

NUMERICAL METHOD FOR ASSESSING SURFACE INSTABILITY

The following section summarizes the numerical methods which have been used in the numerical assessment of rockbursting. This section only outlines major results. Mathematical derivations are documented either in appendices or in the publications referenced in the text. The methods presented in this section have been implemented in the nonlinear finite element code, LINOS. The computer code LINOS was developed at the University of Southern California three years ago. Its main objective is to serve as a vehicle for applying nonlinear constitutive equations of soils and rocks especially in the range of large deformation and in presence of bifurcations. LINOS was therefore especially suited for the analysis of surface instability. According to the modular structure of LINOS, which is common to most of the large finite element codes, the library of element and material subroutines can be easily expanded without alteration of the main code. In the context of this project, a new element module and two new material modules were added to the element and material library. In addition to these three new modules, two other modules have been coded to perform the calculation of the eigenvalues and eigenvectors of the stiffness matrix. All these modules can certainly be modified to fit into other finite element codes such as ADINA (Bathe, 1982).

This section is divided into six subsections:

1. updated Lagrangian variational formulation
2. calculation of tangential stiffness matrix
3. detection of bifurcation point

4. calculation of eigenvalues and eigenvectors of tangential stiffness matrix
5. constitutive models
6. finite element implementation of constitutive models

2.1 UPDATED LAGRANGIAN VARIATIONAL FORMULATION.

Biot, 1965, Horii and Nemat-Nasser, 1982, and Vardoulakis, 1984, based their analysis of surface instability upon the partial differential equations of equilibrium for incremental stresses. They did not use the variational principles which are the fundamental basis of finite element methods. One of the first and most important point of the numerical assessment of surface instability was to verify the compatibility of the nonlinear variational principle of our finite element code, LINOS, with the nonlinear partial differential equations used by previous investigators. This compatibility, which is rather straightforward to derive in the case of small deformation, becomes less obvious in the case of large deformation due to the multiple choices of accounting for material and geometrical nonlinearities. In fact the variational principle used in LINOS is identical to the variational principle derived by Biot (1965, pp 73-79), and by McMeeking and Rice, 1978. This formulation, which requires the update of the body configuration as it deforms, is referred to as updated Lagrangian. The position of the finite element mesh changes after each time step in order to perform the volume and surface integrations on the deformed, not initial, body configuration. The updated Lagrangian method is detailed by Bathe, 1982, (pp 335-406).

2.2 CALCULATION OF TANGENTIAL STIFFNESS MATRIX.

The finite element analysis of bifurcation problems requires more accurate and numerous calculation of the tangential stiffness matrix than most conventional nonlinear finite element analysis. In nonlinear computations, accurate results can be obtained with an approximate stiffness matrix if an iterative technique balances the internal and external forces. For example, in the case of the modified Newton-Raphson method, the tangential stiffness matrix can be reformed only once, at the first time step, or a few times, at some later time steps. For modified Newton-Raphson, iterations are carried out until the out-of-balance or residual forces become negligible. Out-of-balance or residual forces are equal to the difference between internal and external forces. Modified Newton-Raphson methods are sometimes preferred to full Newton-Raphson technique since they are less time-consuming, i.e., the stiffness matrix does not have to be reformed as many times as for full Newton-Raphson.

However, in the case of bifurcation analysis, the stiffness matrix must be calculated frequently and accurately. The objective of a finite element analysis of bifurcation problems is to detect the loss of uniqueness of the incremental solution Δd for the following general type of nonlinear matrix problem of n dimension

$$\mathbf{K(d)}.\Delta d = \Delta F \qquad (2)$$

where

Δd = increment of nodal displacement at time t

$\mathbf{d}$ = nodal displacement at time t
(cumulated value of Δd between times 0 and t)

ΔF = residual or out-of-balance force
(difference between internal and externally applied loads)

$\mathbf{K}(\mathbf{d})$ = tangential stiffness matrix
(dependent on the nodal displacement $\mathbf{d}$ at time t)

n = number of degrees of freedom

The bifurcation of the increment Δd from one to another type of solution is only possible when the problem (2) admits more than one solution. This loss of uniqueness can only take place when the matrix $\mathbf{K}(\mathbf{d})$ becomes singular, which is associated with a zero determinant. Therefore, the detection of possible points of bifurcation requires an accurate evaluation of the stiffness matrix, especially in the vicinity of the bifurcation. In order to compute the stiffness matrix accurately, a new element has been developed. This element is a two-dimensional plane-strain isoparametric four-node element with four stress point which can handle large deformation. The four stress points are located at the gaussian points of the element. One stress point can also be selected at the element centroid. The integration rules which are used to evaluate the volume integrals at the element level can be chosen with two by two or one Gaussian points. In the present work, only four stress points and four integration points were used. The influence of reduced integration and stress points on the surface instability has not been investigated and could be the object of future research.

2.3 DETECTION OF BIFURCATION POINT.

The bifurcation point, which corresponds to the loss of uniqueness of the incremental matrix problem (2), is possible when the determinant of the increment tangential matrix becomes equal to zero. In the present numerical approach, the bifurcation point can be detected by choosing one out of three techniques. It can be found by checking the sign change of either the pivots, the determinant, or the eigenvalues of the stiffness matrix. The first

method of detection is rather simple and efficient. It takes place right after the factorization of the stiffness matrix into upper, lower triangular and diagonal matrices:

$$\mathbf{K}(\mathbf{d}) = \mathbf{L}.\mathbf{D}.\mathbf{U} \tag{3}$$

$\mathbf{L}$ = lower triangular matrix
$\mathbf{D}$ = diagonal matrix
$\mathbf{U}$ = upper triangular matrix

By definition, the pivots of $\mathbf{K}$ are the diagonal entries of $\mathbf{D}$, noted D_{ii}, i=1,n. In the case of symmetric matrix,

$$\mathbf{L} = \mathbf{U}^t \tag{4}$$

where $\mathbf{U}^t$ represents the transpose of $\mathbf{U}$.
The *second method* computes the determinant of the stiffness matrix $\mathbf{K}$ by calculating the products of the pivots. Since for triangular matrices $\mathbf{L}$ and $\mathbf{U}$

$$\det(\mathbf{L}) = \det(\mathbf{U}) = 1 \tag{5}$$

then the determinant of $\mathbf{K}$ is the products of the pivots:

$$\det(\mathbf{K}) = \det(\mathbf{D}) = D_{11}.D_{22}.D_{33}. \ \ldots \ .D_{nn} \tag{6}$$

The third and last method is more time consuming than the first two methods; it requires the calculation of the eigenvalues of the stiffness matrix. This calculation is carried out just after the formation of the tangential stiffness matrix but before its factorization. If the selected bifurcation condition is met at time t_{n+1}, then bifurcation takes place between times t_n and t_{n+1}.

If the bifurcation time is needed with more accuracy, the step-by-step analysis can be restarted from time t_n by using a smaller time interval, and stopped when the bifurcation condition is met again. Theoretically, this process could be repeated several times until the time interval $[t_n, t_{n+1}]$ becomes small enough. Alternate techniques of detection use Regula-Falsi method or the method proposed by M. Fujikake (1985). Iterative techniques to refine the bifurcation time was not required in the present analysis since very small loading steps were used.

2.4 CALCULATION OF EIGENVALUES AND EIGENVECTORS OF THE TANGENTIAL STIFFNESS MATRIX.

Two program modules have been coded to compute the eigenvalues and eigenvectors of the tangential stiffness matrix. One modules calculates only the eigenvalues during the step-by-step integration in order to detect the bifurcation point. The second module calculates both the eigenvalues and the eigenvectors of the stiffness matrix after the detection of the bifurcation point. With the help of the interactive capability of the second module, the user can select and plot the eigenvectors as it is important to understand the significance of the eigenvectors corresponding to the lowest eigenvalues. Both modules use subroutines from the EISPACK package (Smith, 1976).

2.5 CONSTITUTIVE MODELS.

In the context of this analysis, the following general class of rate-type constitutive equations are considered:

$$\hat{r}_{ij} = C_{ijkl}\, \hat{D}_{kl} \tag{7}$$

where $\overset{\wedge}{\tau}$ is the Jauman rate of Kirchhoff stress, **D** the rate of deformation, and C_{ijkl} may be any function of states of stress and strain which characterizes the incremental material response. In the following section, three types of constitutive equations (7) will be specified: isotropic and anisotropic hypo-elastic materials, and isotropic elasto-plastic materials of the flow theory of plasticity. The selected constitutive models have two, three, or five material constants, respectively, which quantify the response of a particular material.

2.5.1 Isotropic hypo-elastic solids: (two material constants).

$$\overset{\wedge}{\tau}_{ij} = \left(G(\delta_{ik}\delta_{jl}+\delta_{il}\delta_{jk}) + \lambda.\delta_{ij}\delta_{kl} \right).D_{kl} \qquad \text{sum on } k,l=1,2,3 \qquad i,j=1,2,3 \quad (8)$$

where δ_{ij} is Kroneker symbol:

$$\delta_{ij} = 1 \quad \text{if } i=j, \quad \text{and} \quad \delta_{ij} = 0 \quad \text{if } i\neq j \qquad i,j=1,2,3 \quad (9)$$

and G and λ are shear and Lame's moduli, respectively.

2.5.2 Anisotropic hypo-elastic solids (three material constants).

As a particular case of anisotropy, transverse anisotropy in plane strain can be accounted for by introducing a transverse shear modulus G_t. In the case of incompressible material with the plane of isotropy normal to the x_2 direction, the plane strain constitutive equation is:

$$\overset{\wedge}{\tau}'_{ij} = 2GD'_{ij} \qquad i=j=1,2 \qquad (10a)$$

$$\hat{\tau}'_{ij} = 2G_t D'_{ij} \qquad i \neq j \qquad \text{(10b)}$$

$$D_{kk} = 0 \qquad \text{incompressibility} \qquad \text{(10c)}$$

$$\hat{\tau}'_{ij} = \hat{\tau}_{ij} - \delta_{ij}\hat{\tau}_{kk}/3 \qquad \text{deviatoric stress rate} \qquad \text{(10d)}$$

$$D'_{ij} = D_{ij} - \delta_{ij}D_{kk}/3 \qquad \text{deviatoric strain rate} \qquad \text{(10d)}$$

A new material model is introduced by modifying relation (10) in order to have *compressibility:*

$$\hat{\tau}_{ij} = 2GD_{ij} + \lambda D_{kk} \qquad i=j=1,2 \qquad \text{(11a)}$$

$$\hat{\tau}_{ij} = 2G_t D_{ij} \qquad i \neq j \qquad \text{(11b)}$$

This material model, which is not transversely isotropic in a rigorous sense, is referred to as anisotropic hypo-elastic. If the shear moduli are equal

$$G = G_t \qquad \text{(11c)}$$

then the equation (11) is the one of the fully isotropic case.

2.5.3 Elastoplastic solid (five material constants).

Adopting the notation of Rudnicki and Rice (1975), the following elastoplastic constitutive relations of the flow theory of plasticity are considered:

$$\hat{\tau}_{ij} = \Big(G(\delta_{ik}\delta_{jl}+\delta_{il}\delta_{jk}) + (B-2G/3).\delta_{ij}\delta_{kl} - \frac{1}{H + G + \mu\beta B}\Big(G\frac{s_{ij}}{\tau} + \beta B\delta_{ij}\Big).\Big(G\frac{s_{kl}}{\tau} + \mu B\delta_{kl}\Big)\Big) D_{kl} \qquad (12a)$$

$$i,j=1,2,3 \quad \text{sum on } k,l=1,2,3$$

where

G = shear modulus
B = bulk modulus
H = plastic modulus
μ = friction coefficient
β = dilatancy parameter

$$s_{ij} = \sigma_{ij} - \frac{1}{3}\sigma_{kk}\delta_{ij} \qquad \text{deviator stress} \qquad (12b)$$

$$\tau = \Big(\frac{1}{2}s_{ij}s_{ij}\Big)^{0.5} \qquad \text{invariant of deviator stress} \qquad (12c)$$

$$\sigma = \sigma_{kk}/3 \qquad \text{mean pressure} \qquad (12d)$$

As shown in the stress space (σ,τ) of Fig.1, the friction coefficient μ and dilatancy parameter β are the slope of yield surface and normal of plastic potential surface, respectively. The relation (12.a) is isotropic and depends only on two stress invariants, σ and τ. They are independent of the third stress invariant, which is sometime referred to as Lode's angle.

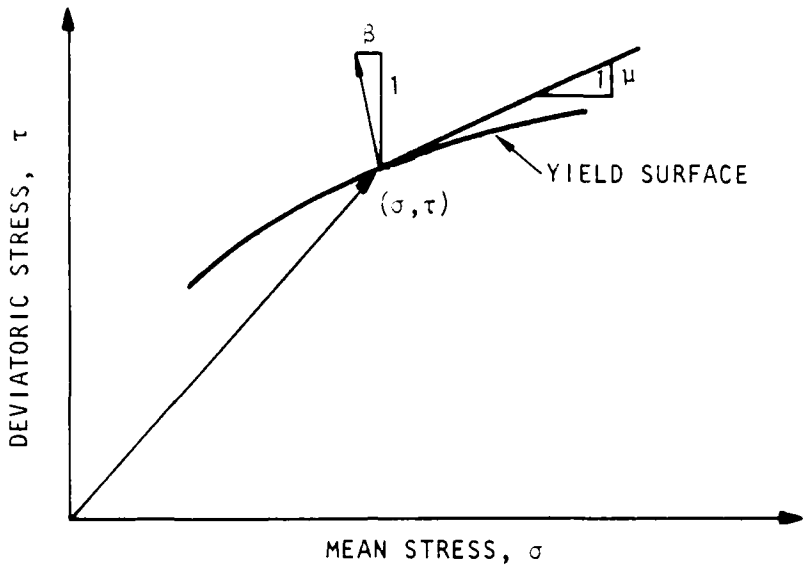

Figure 1. Geometrical interpretation of the coefficient of friction μ and the dilatancy factor β (after Rudnicki and Rice, 1978).

The deformation theory of plasticity has not been considered in this analysis, although it was found to yield more realistic prediction of buckling load than the flow theory of plasticity (Hutchinson and Tvergaard, 1980, Vardoulakis, 1984). The superiority of the deformation theory over the flow theory in the particular case of buckling analysis results from the dependence of the incremental response upon the stress rate direction. However, in some models of the deformation theory, the constitutive matrix is a discontinuous function of the stress increment direction. Such a discontinuity may cause numerical problems in the context of finite element analyses. Therefore, the deformation theory was not considered for this reason.

A particular case of the general elastoplastic relation has

been specified by Horii and Nemat-Nasser (1982). Their model describes the particular experimental data obtained on sandstones. The plastic modulus H is a function of the first stress invariant σ and the effective strain γ. The coefficient μ is a constant, while the dilatancy angle β depend on the stress states (see Horii and Nemat-Nasser, 1982, for further detail)

2.6 FINITE ELEMENT IMPLEMENTATION OF CONSTITUTIVE MODEL.

From the point of view of nonlinear finite element methods the constitutive models are required in two operations: (1) formation of the stiffness matrix and (2) calculation of the residual forces. Consequently the material modules must perform two main tasks: (1) calculation of the constitutive equation C_{ijkl} and (2) stress calculation. The first task is done by evaluating the coefficients C_{ijkl} as specified by the relations (8), (9) and (10). The second task is less straightforward than the first task. The strain increment $\Delta\epsilon$ and rigid rotation **R** which result from incremental nodal displacement are not infinitesimal but finite. Appropriate numerical techniques are therefore required to integrate the rate equations (8),(9) and (10) between time t_n and t_{n+1}. This integration is performed by a module which is referred to as a stress calculation subroutine. Stress calculation subroutines play an important role in the convergence of the iterative scheme which balances out internal and external forces. If the stress are not calculated with sufficient accuracy, convergence may be hard to achieve. This absence of convergence is especially to be expected in the vicinity of bifurcation point, where the stiffness matrix is about to become singular. Error in the stress calculation subroutine may generate artificial out-of-balance force which prevents the system from reaching a bifurcation point.

In the case of finite deformation the stress increment calculation are carried out by using Hughes and Winget (1981) method. The objective stress rate of relation (7) involves the spin **W** in order to account for the rigid body rotations of a material point relative to the spatial coordinates. In incremental form, instead of rate form, the spin **W** becomes an orthogonal rotation through an incremental angle. Hughes and Winget (1981) have given a modern account of this process and have provided a direct way to evaluate the orthogonal rotation matrix **R** from the spin **W**. Thus

$$\mathbf{R} = (\delta - \Delta t\mathbf{W}/2)^{-1}.(\delta + \Delta t\mathbf{W}/2) \tag{13a}$$

where δ is Kroneker's symbol, and Δt the time interval. In two-dimension **R** can be written as:

$$R = \begin{vmatrix} \cos\theta & -\sin\theta \\ \sin\theta & \cos\theta \end{vmatrix} \tag{13b}$$

Half angle trigonometric formulas are used to get $\mathbf{R}^{1/2}$ the square root of **R**. With these constructions the rate-type constitutive models (7) can be integrated over the increment from t_n to t_{n+1} in the following way. First the stresses σ_n, which represent the stress at all the stress points at time t_n, are advanced to the time $t_{n+1/2} = (t_n+t_{n+1})/2$ by

$$\sigma_{n+1/2} = \mathbf{R}^{1/2}.\sigma_n.(\mathbf{R}^{1/2})^t \tag{14}$$

Using the intermediate configuration between time t_n and t_{n+1}, and the time step Δt, the strain increments $\Delta\epsilon_{n+1/2}$ are calculated at all the stress points from the nodal displacement between times t_n and t_{n+1}. Then the constitutive equation is integrated and new stresses $\sigma_{n+1/2}$ are obtained. These are then

rotated from $t_{n+1/2}$ to t_{n+1} by the same process as in equation (14). The integration of the constitutive equation is carried out by using a subincremental technique dividing the prescribed strain increment $\Delta\epsilon_{n+1/2}$ into several subincrements. Each subincrement is integrated with an improved Euler method without iteration. In our computations, the subincrementation was not fully exploited; only one increment was used.

SECTION 3

NUMERICAL RESULTS ON SURFACE INSTABILITY OF THE WEDGE TEST

The following section summarizes the numerical results which are obtained on the surface instability of a particular boundary value problem - the plane-strain compression of a cube, which is referred to as the wedge test. The calculations were carried out by using computer modules which are based on the methods and principles presented in the previous sections. The objectives of the present section are (1) to verify that our computer modules are correctly implemented and, (2) to check that the selected finite element method is appropriate to describe surface instability in the particular case of the wedge test. The performance of the computer modules, especially the new element and material model subroutines, are tested by comparing finite element results with analytical or numerical results derived for hypo-elastic and elastoplastic material models.

This section is divided into six subsections:

1. Geometry and boundary conditions of the wedge test
2. Finite element mesh
3. Analytical solutions for stress-strain response and bifurcation load
4. Integration algorithm
5. Change of eigenvalues versus applied displacement
6. Eigenvalues and eigenvectors at the bifurcation point

3.1 GEOMETRY AND BOUNDARY CONDITIONS OF THE WEDGE TEST.

The geometry and boundary conditions of the wedge test are shown in Fig.2. The cubical body has a one to one aspect ratio.

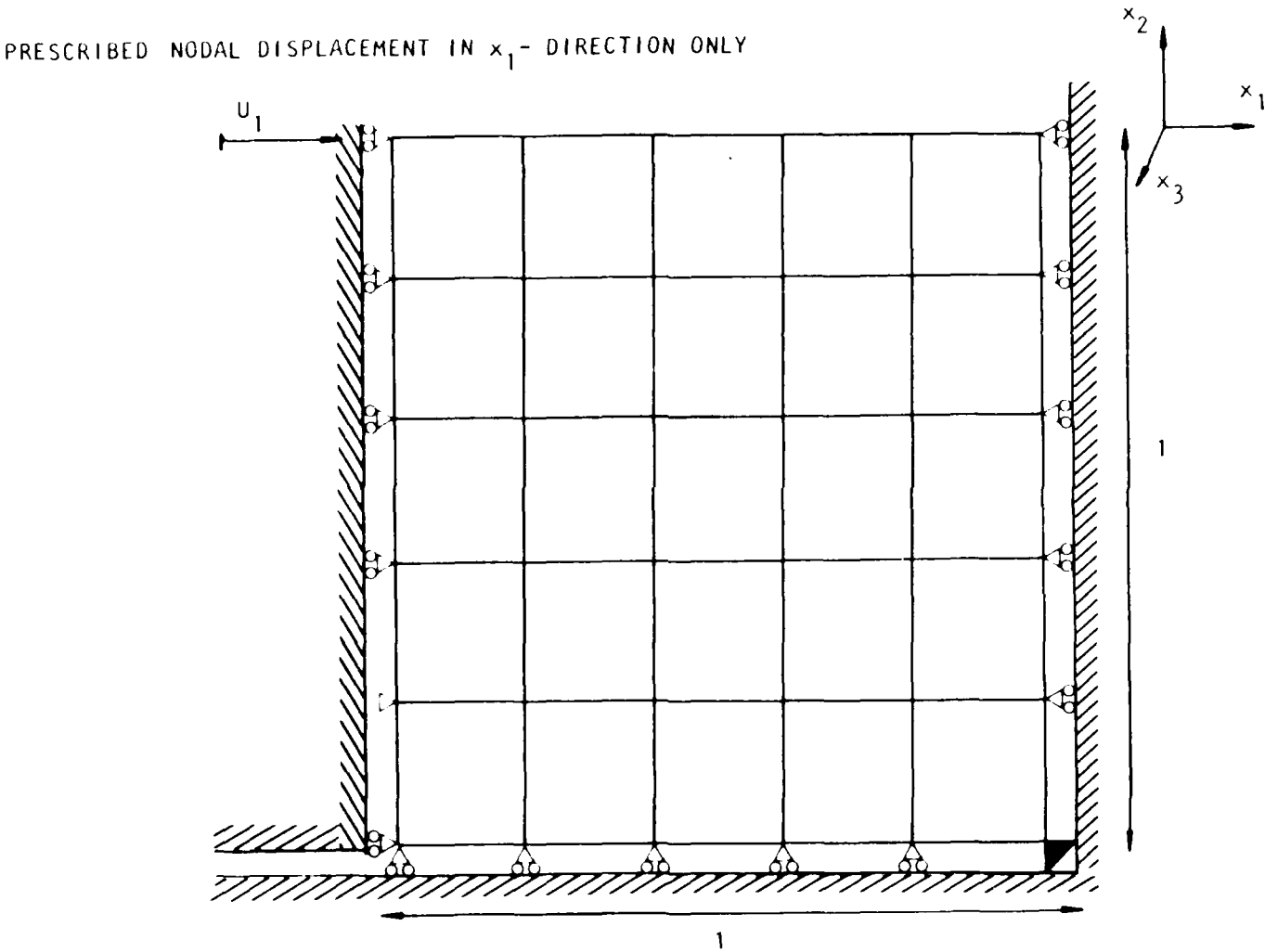

Figure 2. Geometry, boundary conditions, and finite element mesh of the wedge test.

The initial length of its sides is equal to unit length. The left, right, and lower boundaries are frictionless. The upper boundary is free of traction. The block is subjected to plane strain deformation by preventing displacement in the x_3 direction. The horizontal displacement of the nodes located on the left boundary are prescribed while their vertical displacement is free. The horizontal displacement u_1 on the left boundary is specified by applying a selected displacement increment Δu_1, the size of which is 0.0025. Therefore 200 increments are required to reach the horizontal displacement of 0.5. In this deformation range - 50% - the strain is finite, which results in nonlinear relationships between strain and displacement gradient. Such a geometrical nonlinearity constitutes a meaningful test for the updated Lagrangian technique. The vertical nodal displacements on the left boundary will be fixed in a later section to investigate the effect of nonuniform stress field on surface instability. The geometry and boundary conditions of Fig.2 correspond to the compression of a material block between five lubricated rigid plates with only one free surface. For such an idealized test condition, the trivial solution is a uniform state of stress and strain within the sample even for large deformation.

3.2 FINITE ELEMENT MESH.

Four different meshes, with one, four, nine and twenty five elements respectively, are used. Fig.2 shows only the 25 elements model. All the elements for a given mesh have the same initial size. They are four nodes isoparametric elements with four stress points per element located at the Gaussian points of the element. The number of degrees of freedom of the problem varies with the number of elements as indicated in Table 1. As shown in Table 1, the number of nodal degrees of freedom increases rapidly with the

number of elements, which causes a rapid increase of the computation time to extract the eigenvalues and eigenvectors, especially in the case of matrices which are neither symmetric nor positive definite. Mainly for this reason, the number of elements n^2 was limited to 25. Higher order elements or nonuniform mesh are not used in this project. A more detailed analysis of the effect of the mesh refinement on surface instability need to be carried out in the future. Surface instability, which Biot associates to the emergence of surface waves the amplitude of which decays exponentially with depth, could certainly be described more accurately by refining the mesh in the vicinity of the free surface.

Table 1. Degree of freedom versus number of elements in the wedge test

number of elements (on 1 side)	(total)	number of degrees of freedom (size of stiffness matrix)
1	1	2
2	4	9
3	9	20
4	16	35
5	25	54
n	n^2	$2n^2 + n - 1$

3.3 ANALYTICAL SOLUTION FOR STRESS-STRAIN RESPONSE AND BIFURCATION LOAD.

The idealized hypo-elastic model with constant moduli was considered in order to obtain simple analytical solutions. This material may not represent the behavior of any real material but it leads to simple analytical solutions, even for large displacement, when compared to other realistic models. The analytical derivation is detailed in tne Appendix B. The material

parameters of hypo-elastic models are listed in Table 2. The buckling stress of the free surface of the half-space made of such an idealized material can also be calculated analytically or numerically. The values of stress and displacement at the onset of surface instability are shown in Table 3 and Fig.3. The stress-displacement response of Fig.3 calculated by the finite element analysis of hypo-elastic material agree perfectly with the analytical results described in the appendix B, which demonstrates that the element and material model were correctly implemented.

Table 2. Material constants of hypo-elastic and elastoplastic models

model	material constant		
isotropic hypo-elastic	shear modulus	G	1.
	Poisson ratio	ν	0.3
anisotropic hypo-elastic	shear modulus	G	1.
	transverse modulus	G_t	0.1
	Poisson ratio	ν	0.3
elastoplastic	Young's modulus	E	200.
	Poisson ratio	ν	0.3
	Friction coefficient	μ	0.39
	variable dilatancy $\beta = \sqrt{3\mu + \tau/\sigma}$	β	
	variable plastic modulus H $H = \exp(1.8-0.36\sigma+e^{0.6-20\gamma-22\gamma})$		
	$\gamma = \int_0^t (2\, D'_{ij}.D'_{ij})^{0.5}\, dt$		

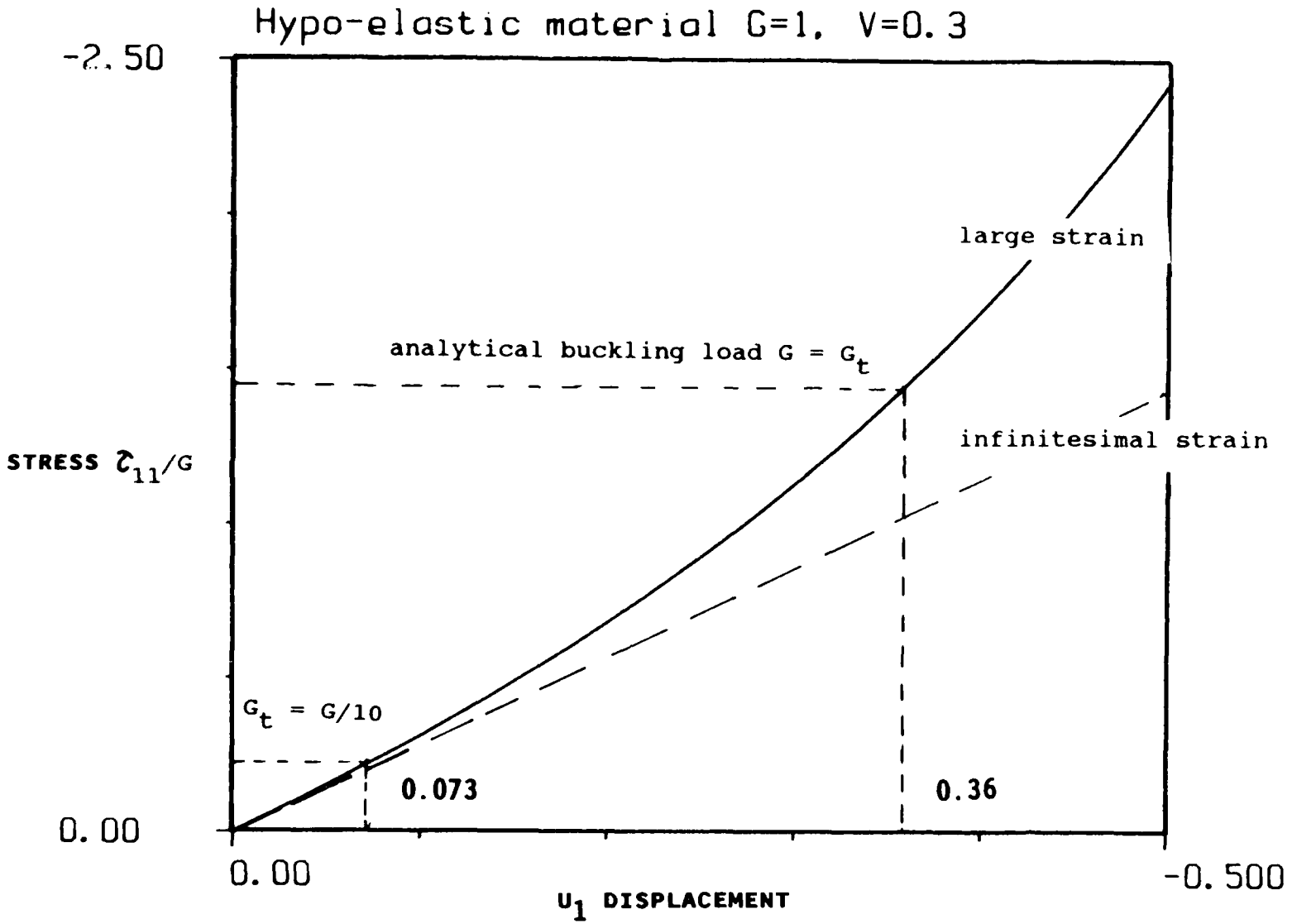

Figure 3. Stress-displacement response and buckling load of isotropic and anisotropic hypo-elastic models during the wedge test.

Table 3. Analytical values of displacement u_1 and normalized stress σ_{11}/G at the buckling of the half space for hypo-elastic and elastoplastic models.

material model	u_1	σ_{11}/G
isotropic	-0.3593	-1.4484
anisotropic	-0.07336	-0.2225
elastoplastic	-0.058	-0.0334

It is important to notice that, for the particular case of the anisotropic hypo-elastic material subjected to the wedge test, the transverse shear modulus G_t affects only the buckling stress but not the stress-strain response. Isotropic and anisotropic hypo-elastic material give the same stress-strain response but different buckling stress. Therefore a good fit of the stress-strain response of the wedge test does not necessarily mean a correct prediction of the buckling load since surface buckling depends on an aspect of the material behavior which is not apparent in the stress-strain response.

In the case of the elastoplastic model of Horii and Nemat-Nasser, 1982, the stress-displacement of Fig.4 has been obtained by integrating step-by-step the plane strain constitutive equation for the material constants specified in Table 2 (see Horii and Nemat-Nasser, 1982, for detail). Surface instability was detected by using a technique similar to the one employed in the computer code BIF. The values of displacement and normalized stress are shown in Table 3.

It is worth noting that, for both hypo-elastic and elastoplastic models, the stress-strain response was derived for

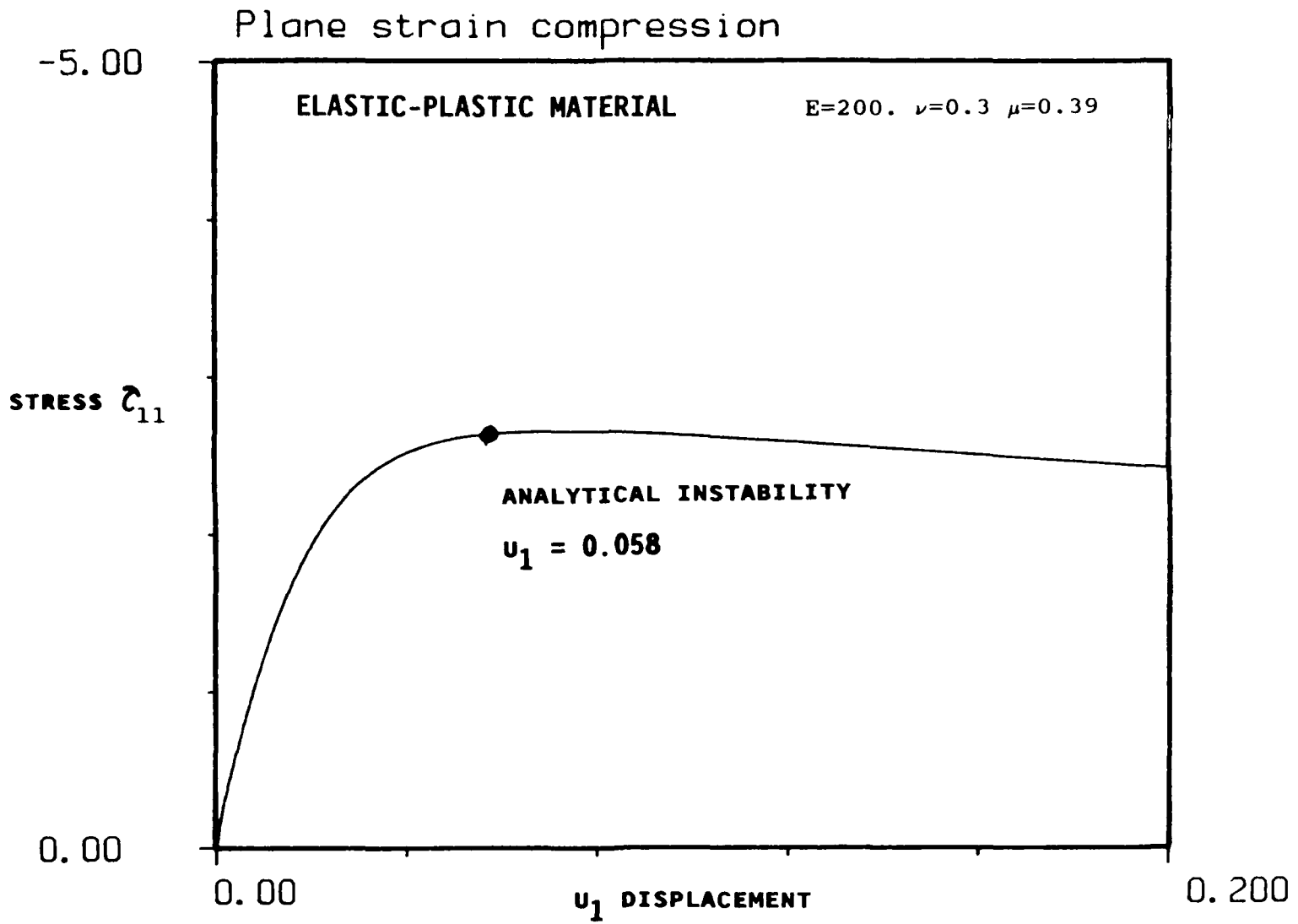

Figure 4. Stress-displacment response and buckling load of the elastic-plastic model of Horii and Nemat-Nasser, 1982, during the wedge test.

the block of finite size shown in Fig.2, and that the buckling stress was obtained for the infinite half-space.

3.4 INTEGRATION ALGORITHM.

Two integration schemes were alternately used to integrate step-by-step the nonlinear finite element problem of the wedge test: full and modified Newton-Raphson methods. During the modified Newton-Raphson computations, the stiffness matrix was reformed only once each time step, which was less time consuming than full Newton-Raphson, but accurate enough due to the small size of the loading increment. At a prescribed boundary displacement u_1, the convergence of both methods is measured by the norm of the residual load vector after a certain number of iterations. Iterative calculations stop when the norm of the residual force is less than some given convergence parameter TOL. Generally TOL is about equal to 10^{-7}. Such a value was sufficiently small to maintain a uniform stress and strain state within the sample of the wedge test, and to obtain the bifurcation point. In some circumstances, larger values of TOL were found to lead to heterogeneous solutions. The error in the computed solution has no important effect far away from the bifurcation point. However as the applied displacement u_1 gets larger, the error becomes larger and larger, and the stress and strain fields become more and more heterogeneous. In the vicinity of the bifurcation point the error is treated as an artificial geometrical imperfection within the finite element mesh. This artificial imperfection is amplified and causes heterogeneous stress and strain solution. This geometrical imperfection, which comes from approximate computation, causes the same effect as the introduction of an eccentricity in the problem of the buckling of an Euler beam. A difficulty in convergence of the solution is also

observed when the applied displacement on the left boundary is too large. In the case of updated Lagrangian techniques which update nodes position, this divergence may cause the annihilation of a few elements (negative volume), which precedes generally a fatal computational crash.

3.5 CHANGE OF EIGENVALUES VERSUS APPLIED DISPLACEMENT.

In order to detect the bifurcation point, the minimum eigenvalue of the stiffness matrix is calculated at each step of prescribed displacement u_1. The minimum eigenvalue is plotted in Figs.5 and 6. versus u_1 for three different meshes and for isotropic and anisotropic materials. As shown in Figs. 5 and 6, the minimum eigenvalue decreases monotonously and becomes zero for some value of the applied displacement u_1. The intersection of λ_{min} with the u_1 axis corresponds to the bifurcation point, where the stiffness matrix becomes singular. As shown in Figs.5 and 6, the mesh refinement has a very important influence on the detection of the bifurcation point. The analytical value of the bifurcation indicated in Table 3 is overestimated when the block is not enough discretized. However 25 elements are sufficient to obtain an approximate value of the buckling stress of the half-space made of hypo-elastic material.

In the case of the elastoplastic model of Horii and Nemat-Nasser, 1982, the minimum eigenvalue of Fig.7 remains positive even for a 25 elements model. As shown in Fig.7, first, λ_{min} starts decreasing, increases when u_1 is about 0.1, and then decreases again for larger value of u_1. Since λ_{min} does not become negative, no surface instability can be detected for this elastoplastic material during the wedge test. This disagreement of analytical and numerical solutions in the case of elastoplastic material will be analyzed in a later section.

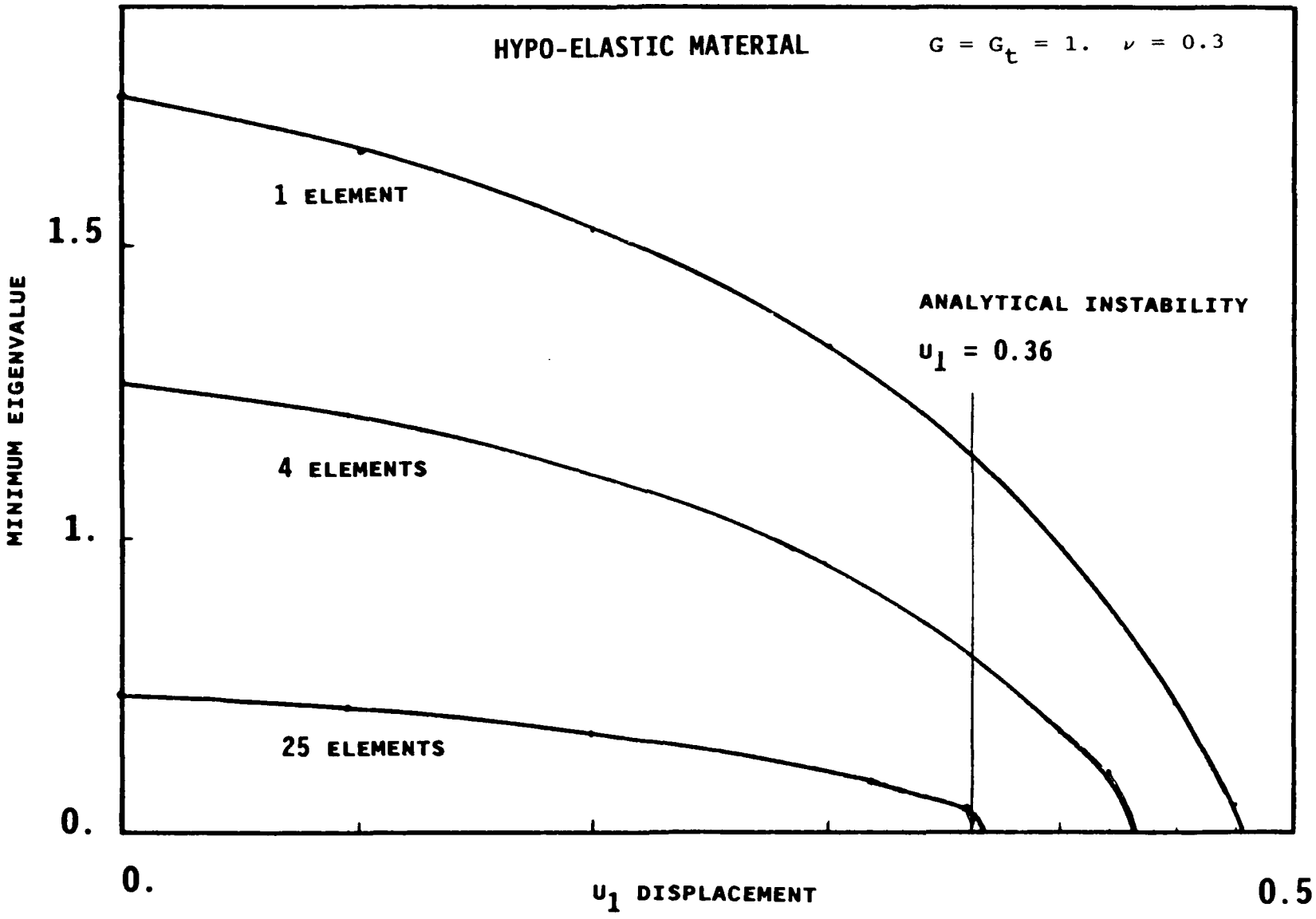

Figure 5. Minimum eigenvalue λ_{min} of stiffness matrix versus applied displacement u_1 for isotropic hypo-elastic material and for 1, 4 and 25 elements models.

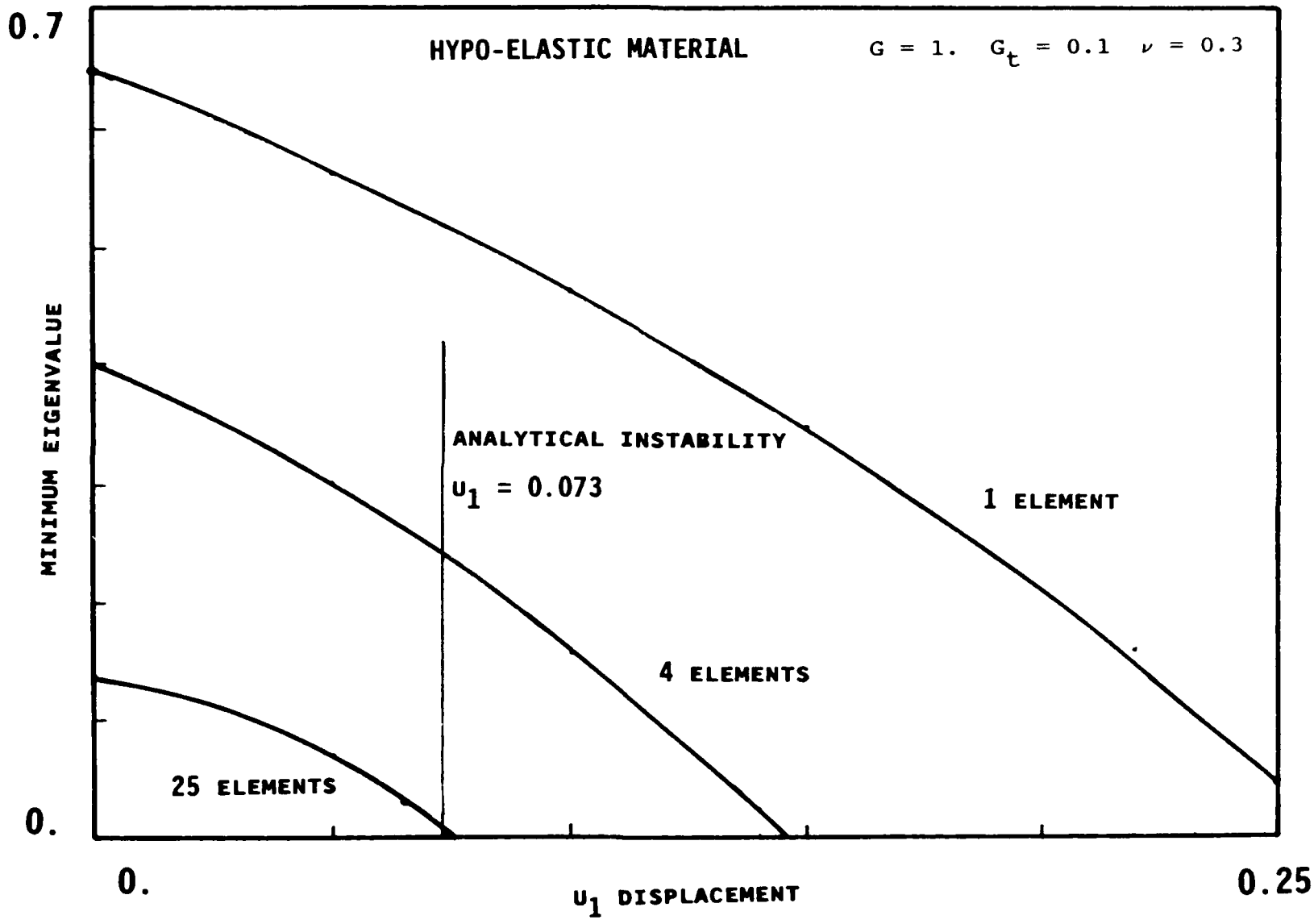

Figure 6. Minimum eigenvalue λ_{min} of stiffness matrix versus applied displacement u_1 for anisotropic hypo-elastic material and 1, 4, and 25 elements models.

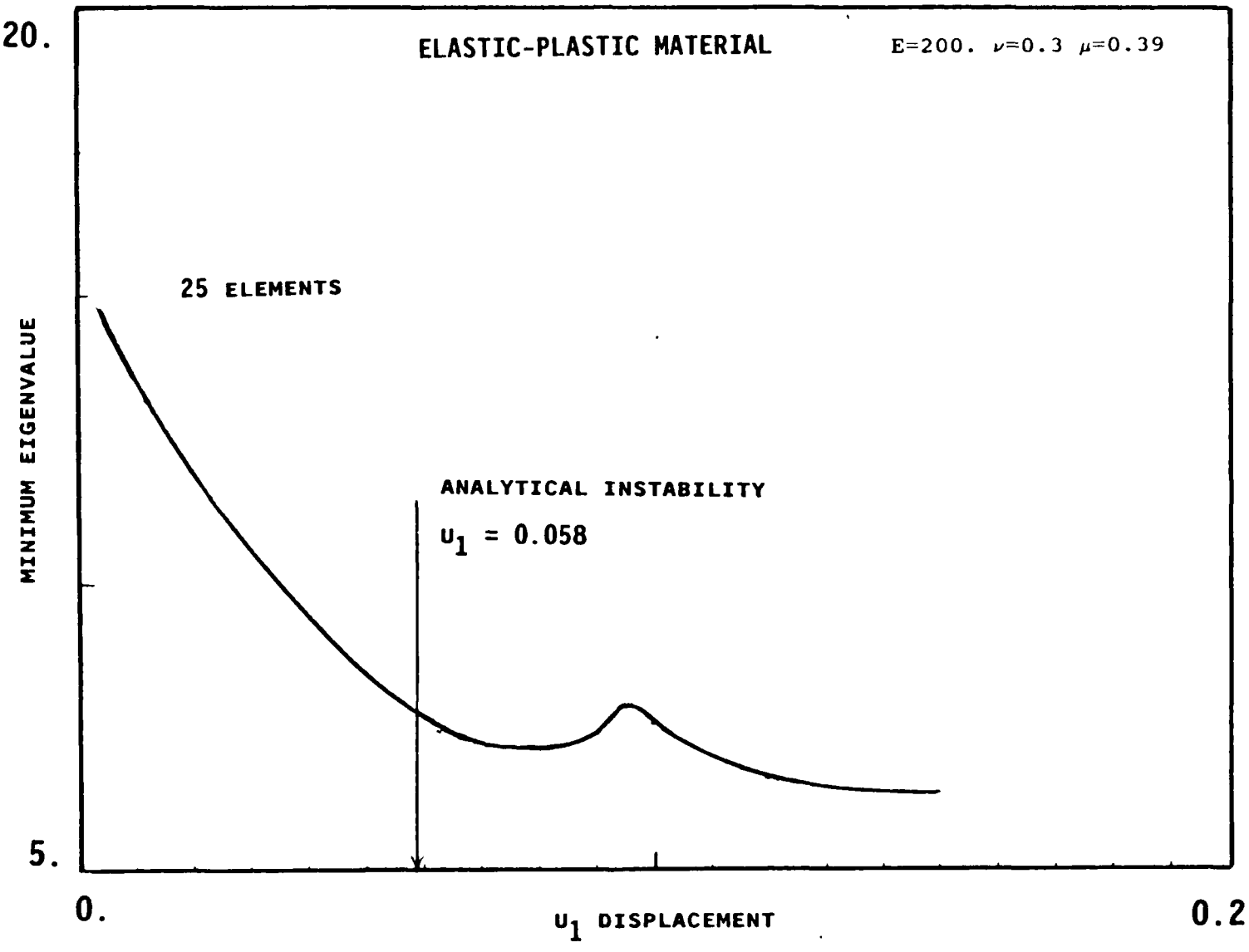

Figure 7. Minimum eigenvalue λ_{min} of stiffness matrix versus applied displacement u_1 for the elastoplastic model of Horii and Nemat-Nasser, 1982, for a 25 elements model.

3.6 EIGENVALUES AND EIGENVECTORS AT THE BIFURCATION POINT.

Once the bifurcation point has been detected between times t_n and t_{n+1}, iterations may be performed to define more accurately the bifurcation time. However these iterations were not necessary in our analysis since the prescribed displacement increment was as low as 0.0025. The calculations were stopped at time t_{n+1} when the tangential stiffness matrix was found to have a negative eigenvalue. The eigenvalues and eigenvectors of the stiffness matrix were calculated at the onset of bifurcation time t_n. Tables 4 and 5 display all the eigenvalues in the case of 4 elements of isotropic hypo-elastic material and 25 elements of anisotropic hypo-elastic material. The eigenvalues, which are sorted according to their values, are listed in the tables 4 and 5. The corresponding eigenvectors, which are identified by the mode number of the eigenvalue, are plotted in Figs. 8 and 9. The eigenvectors are plotted with respect to the deformed mesh, which describes the position of the body at the onset of bifurcation. This representation of eigenmodes is similar to the one used for displaying the natural modes of vibration of structural systems. Figs.8 and 9 show the direction and amplitude of the increment of nodal displacement which are an alternate solution to the constant deformation gradient solution. As shown in Fig.8a to 8d for a 4 elements model, the modes associated with the lowest eigenvalues are surface modes for which the amplitude decays with depth. The mode of Fig.8e, which corresponds to a larger eigenvalue, is a volume mode. Its amplitude does not decay within the material. In addition to the eigenmodes of the coarse mesh of Figs.8, the eigenmodes of a finer 25 elements mesh are examined in Figs.9. The first two modes of Figs 9a and 9b are symmetric w.r.t to a the central vertical axis. The amplitude of the surface wave decays

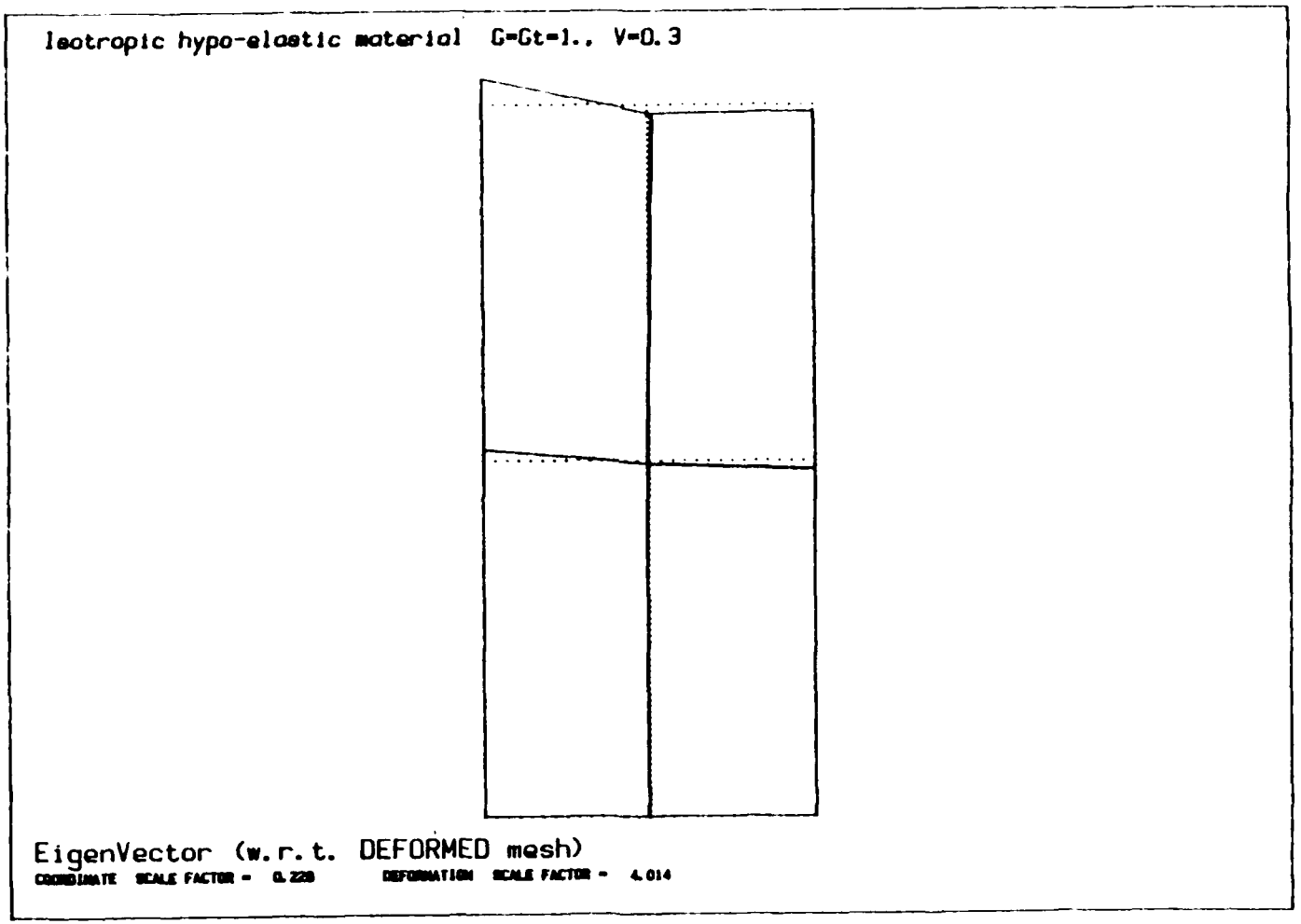

Figure 8a. First eigenmode for a 4 elements model of isotropic hypo-elastic material.

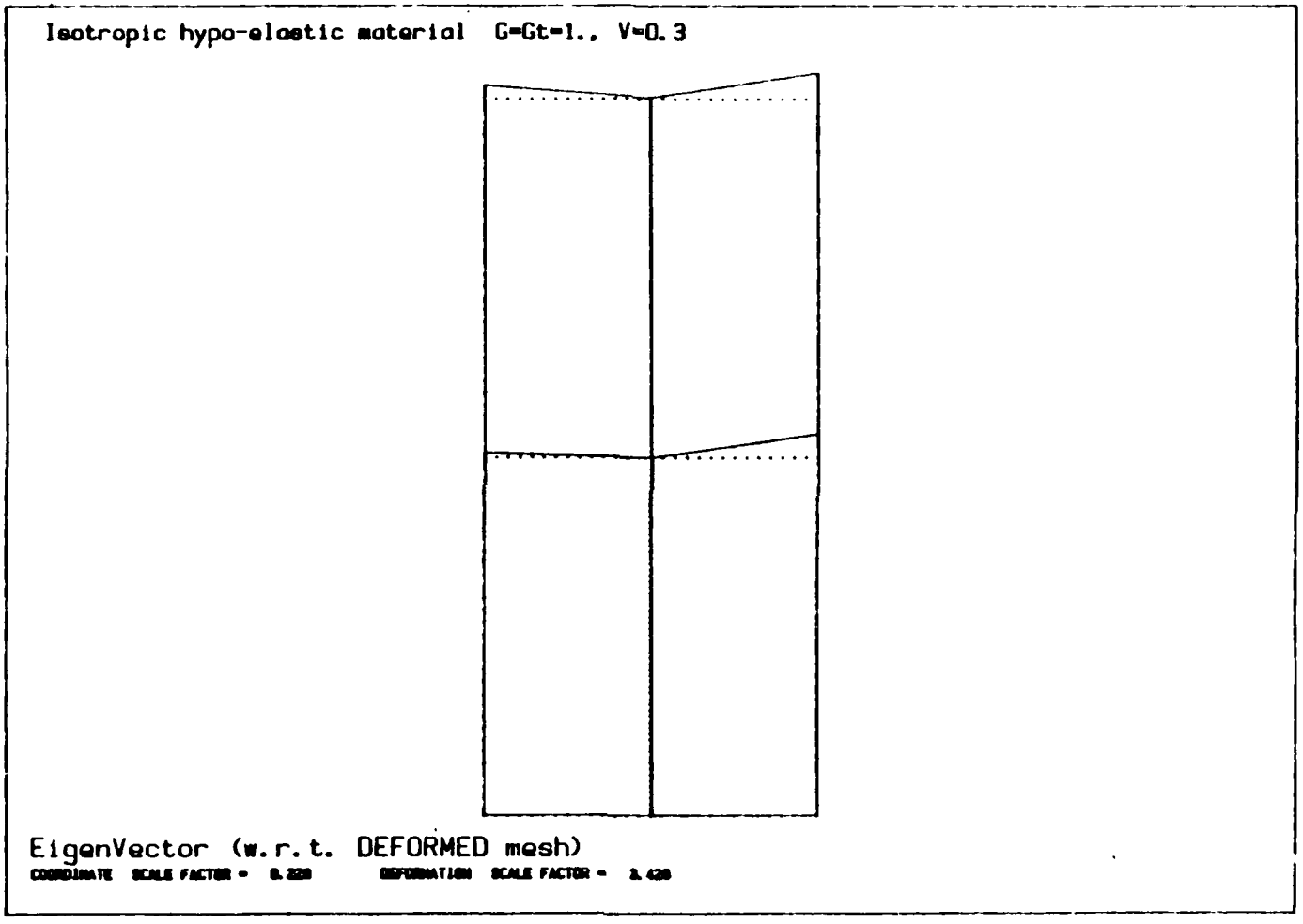

Figure 8b. Second eigenmodes for a 4 elements model of isotropic hypo-elastic material.

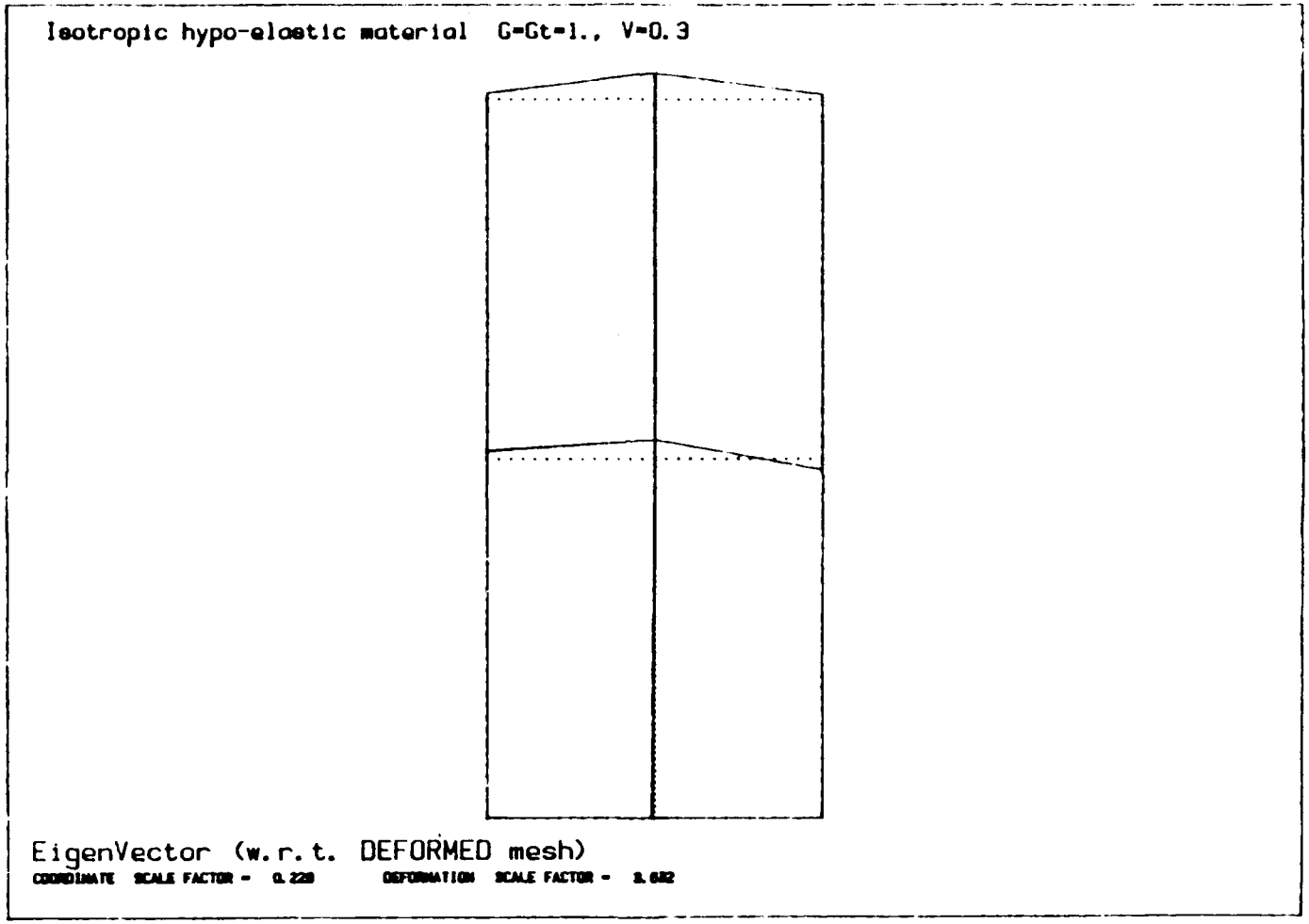

Figure 8c. Third eigenmode for a 4 elements model of isotropic hypo-elastic material.

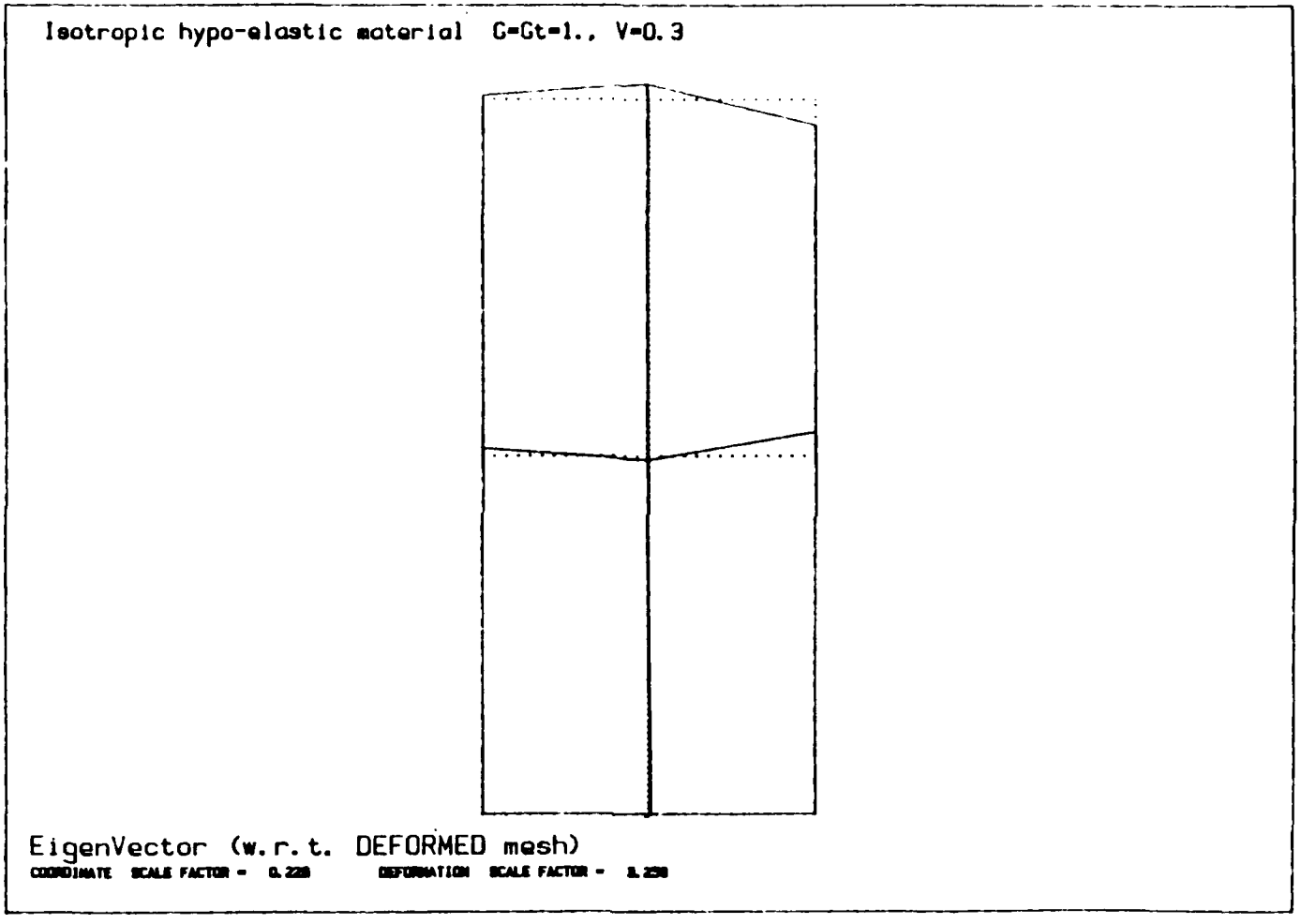

Figure 8d. Fourth eigenmode for a 4 elements model of isotropic hypo-elastic material.

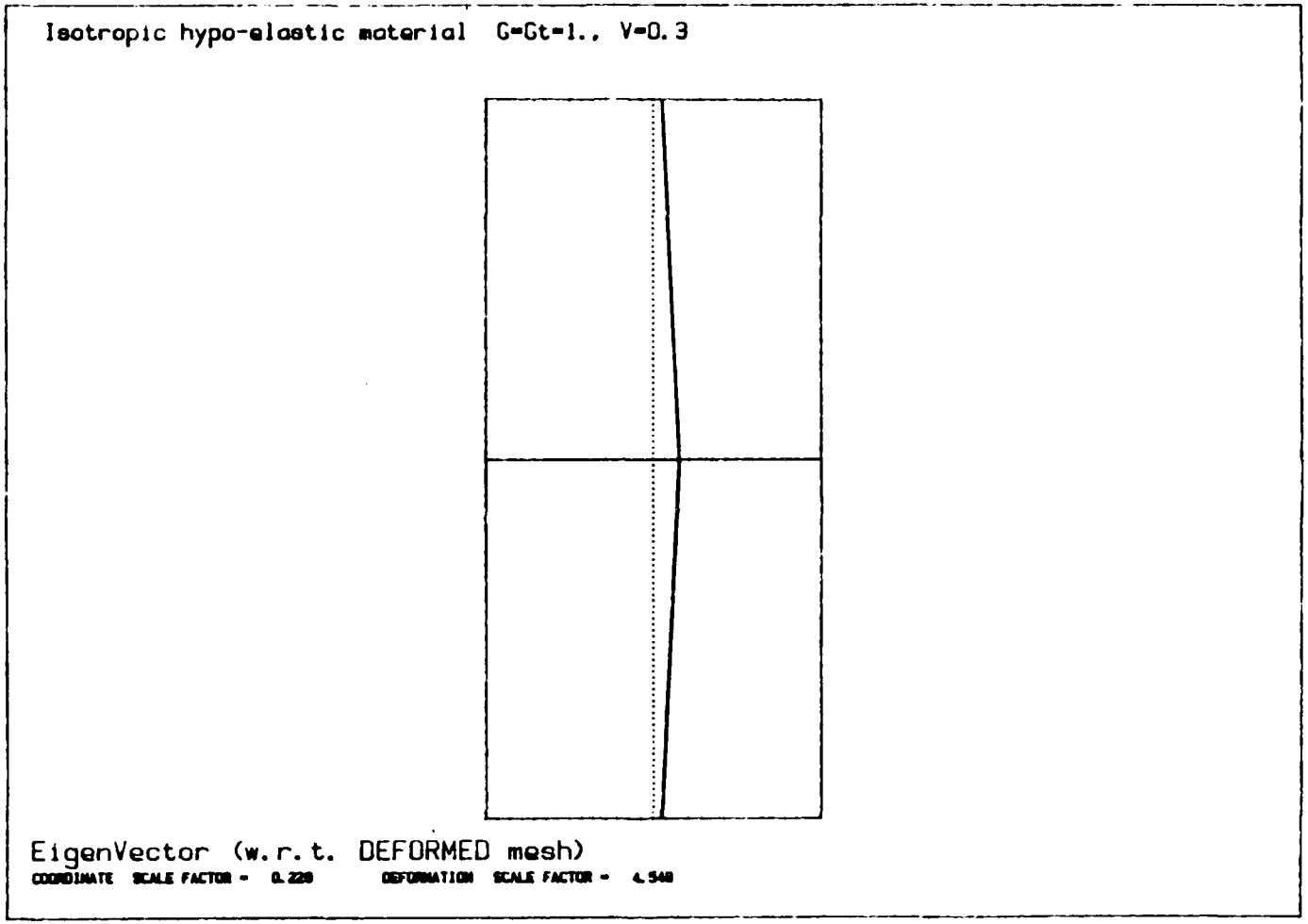

Figure 8e. Ninth eigenmode for a 4 elements model of isotropic hypo-elastic material.

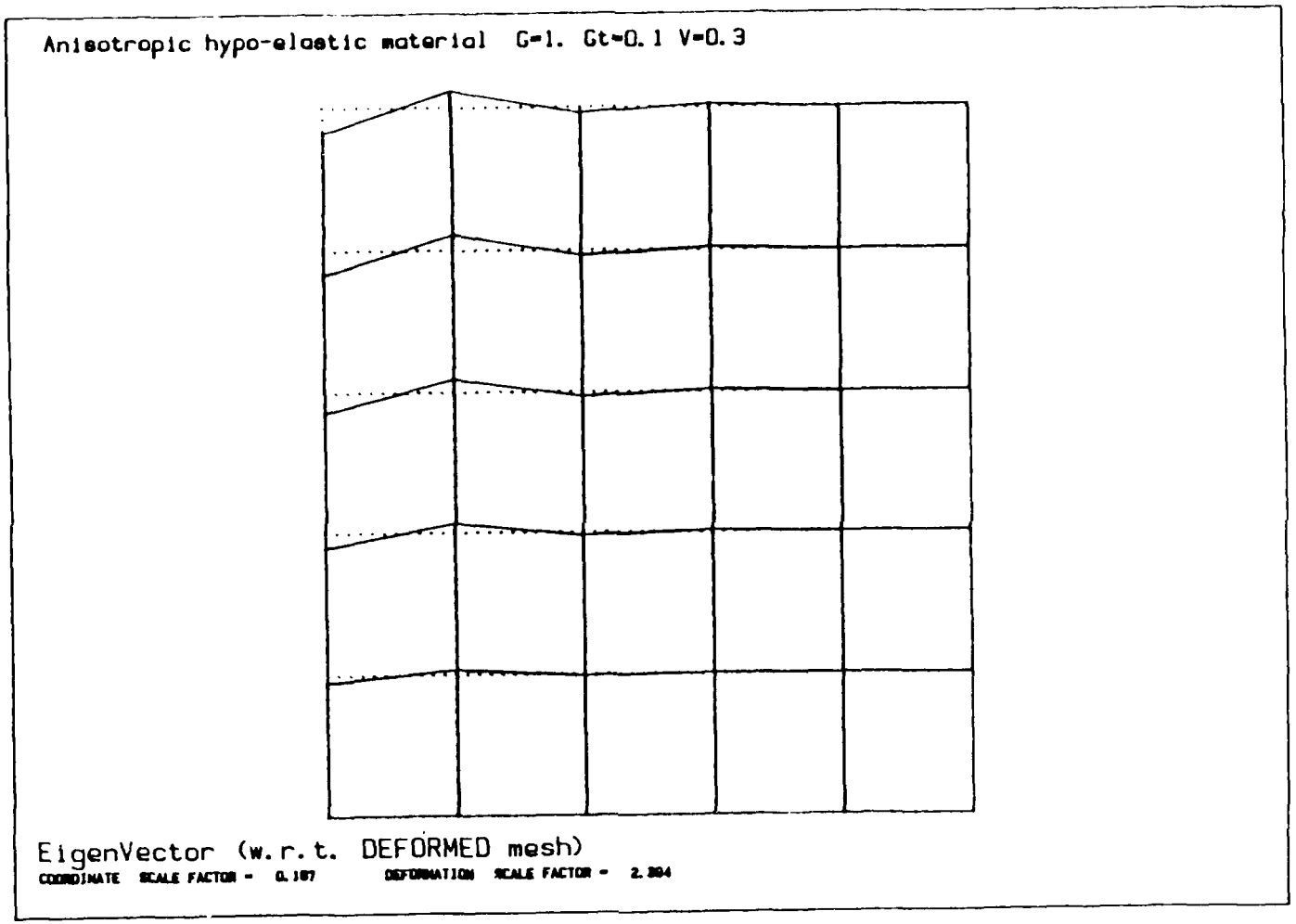

Figure 9a. First eigenmode for a 25 elements model of anisotropic hypo-elastic material.

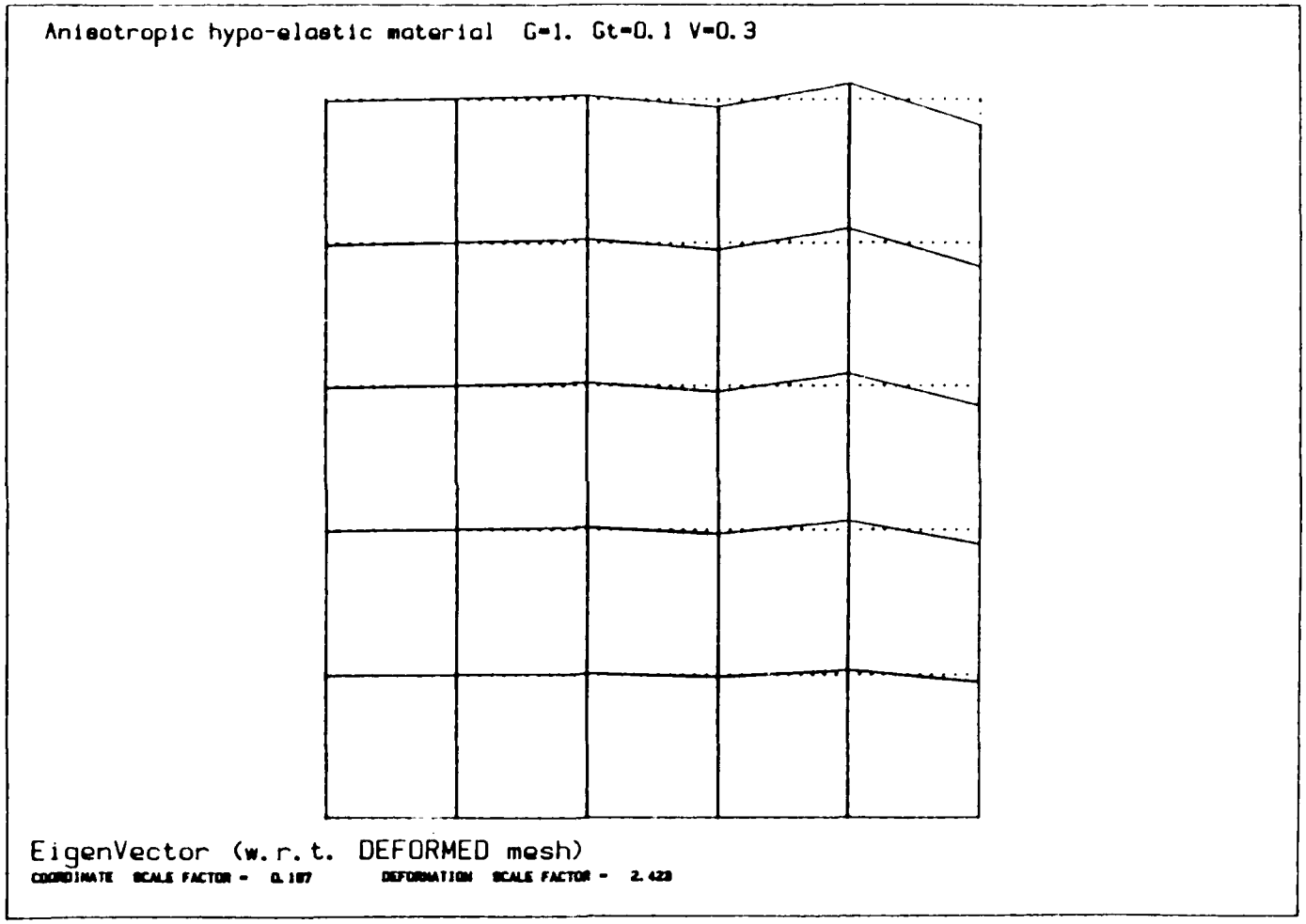

Figure 9b. Second eigenmode for a 25 elements model of anisotropic hypo-elastic material.

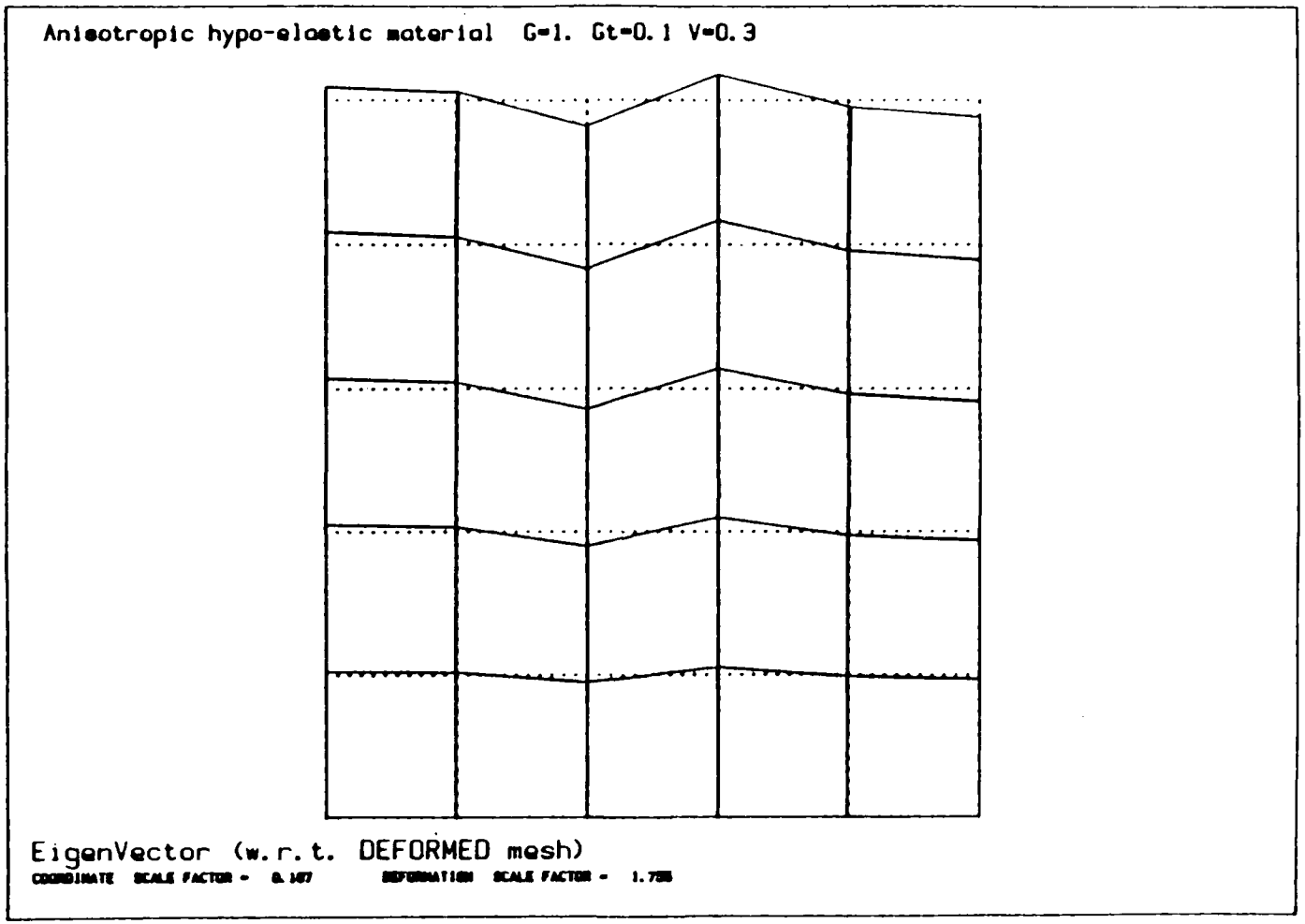

Figure 9c. Third eigenmode for a 25 elements model of anisotropic hypo-elastic material.

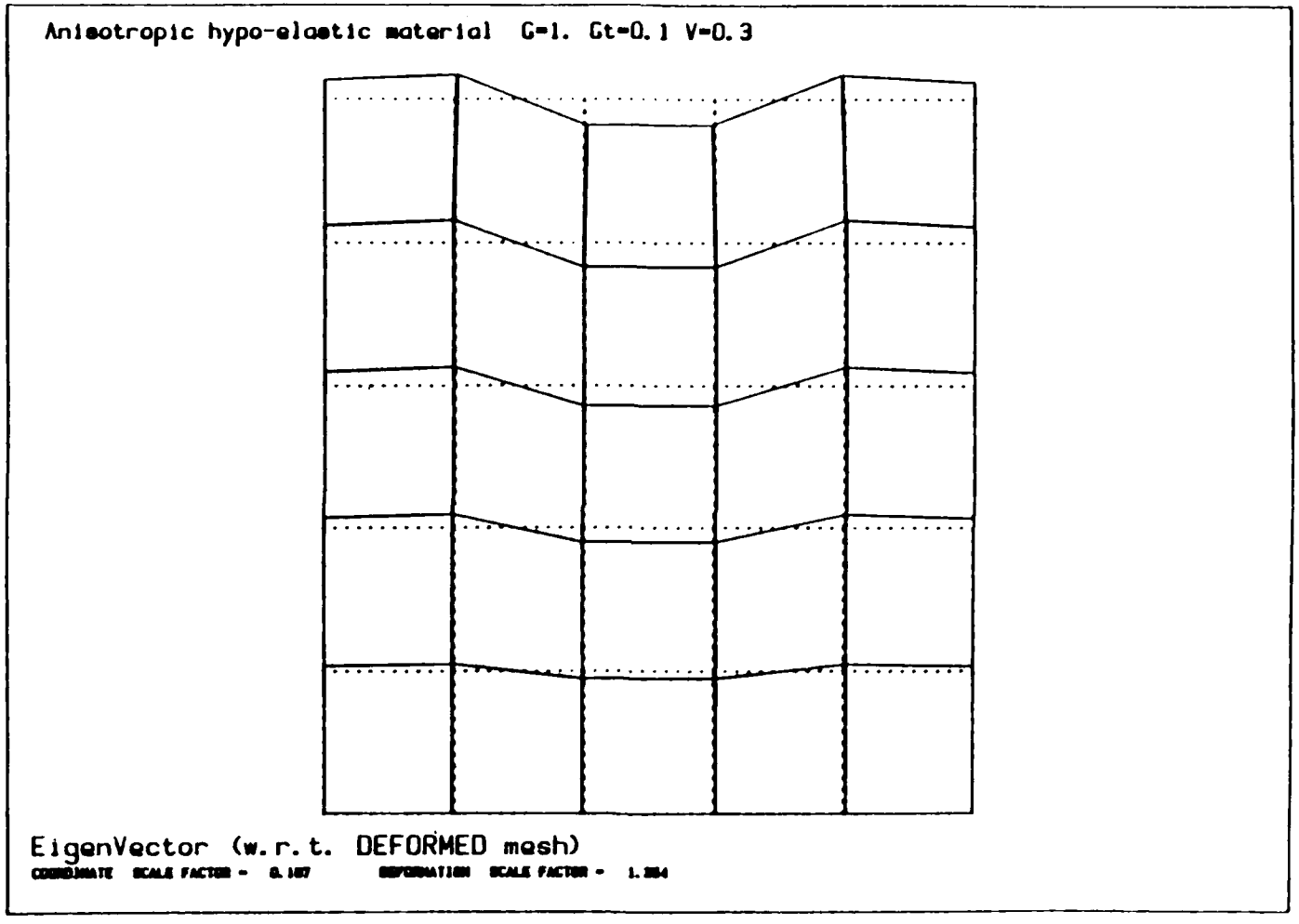

Figure 9d. Fourth eigenmode for a 25 elements model of anisotropic hypo-elastic material.

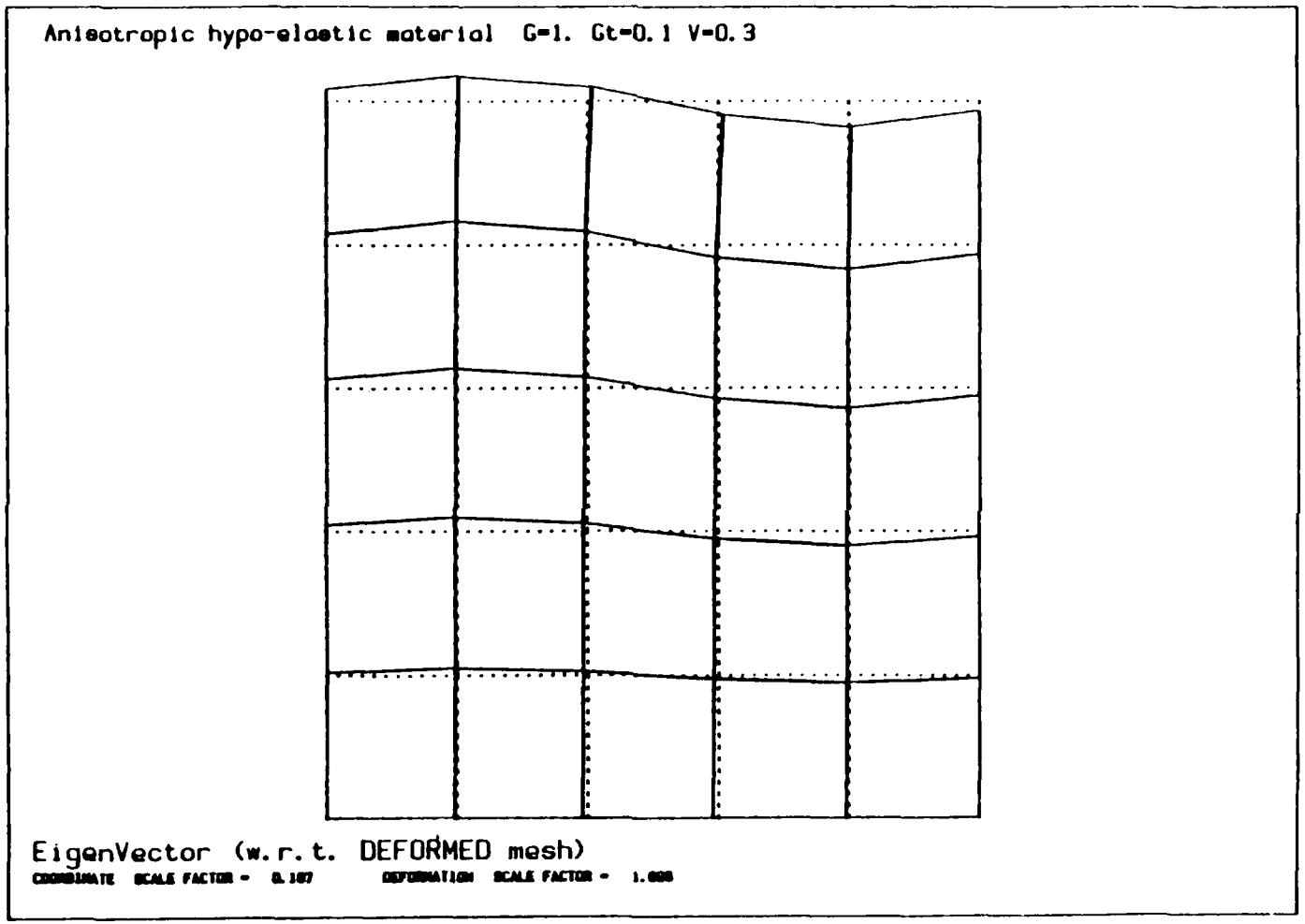

Figure 9e. Fifth eigenmode for a 25 elements model of anisotropic hypo-elastic material.

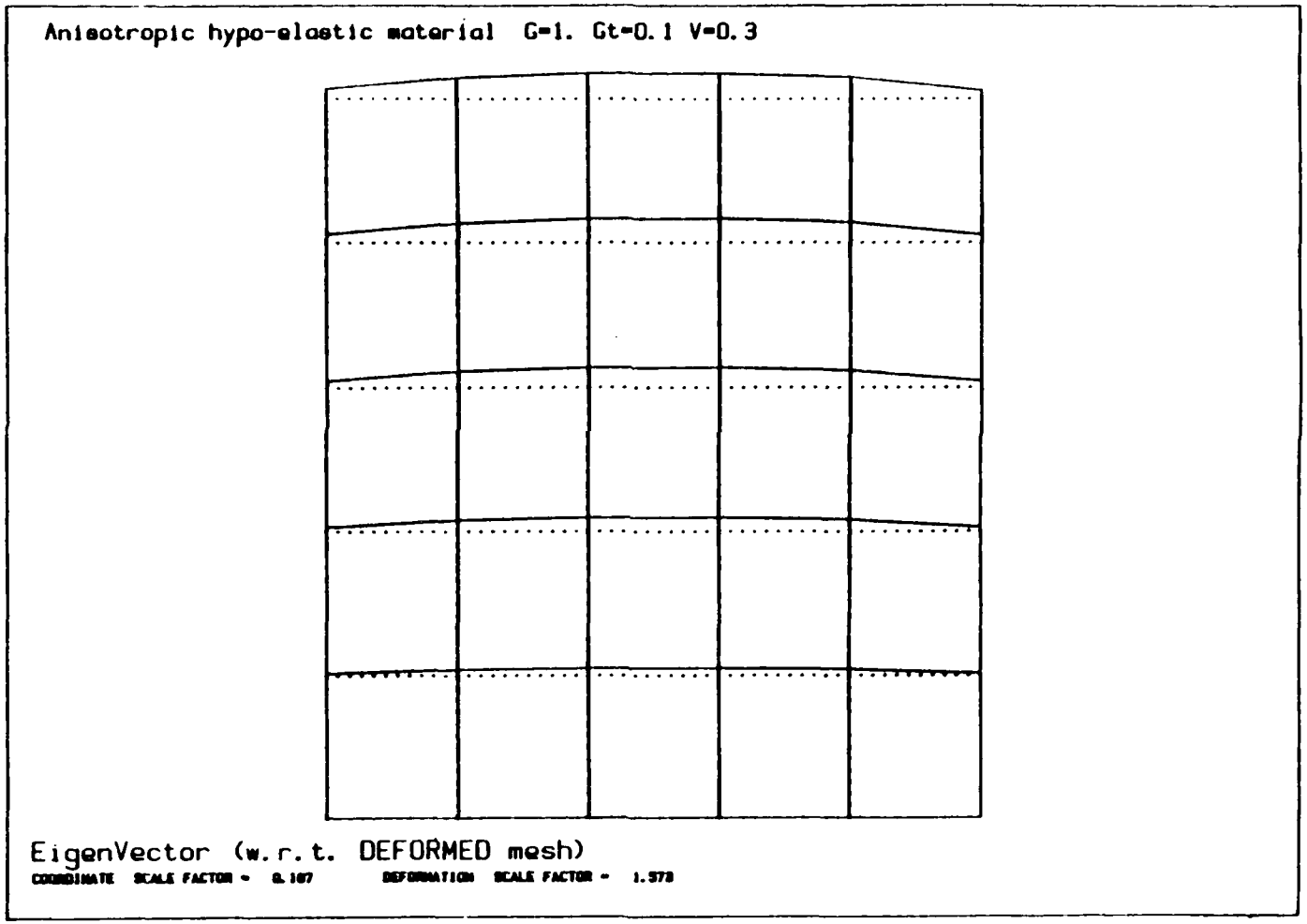

Figure 9f. Sixth eigenmode for a 25 elements model of anisotropic hypo-elastic material.

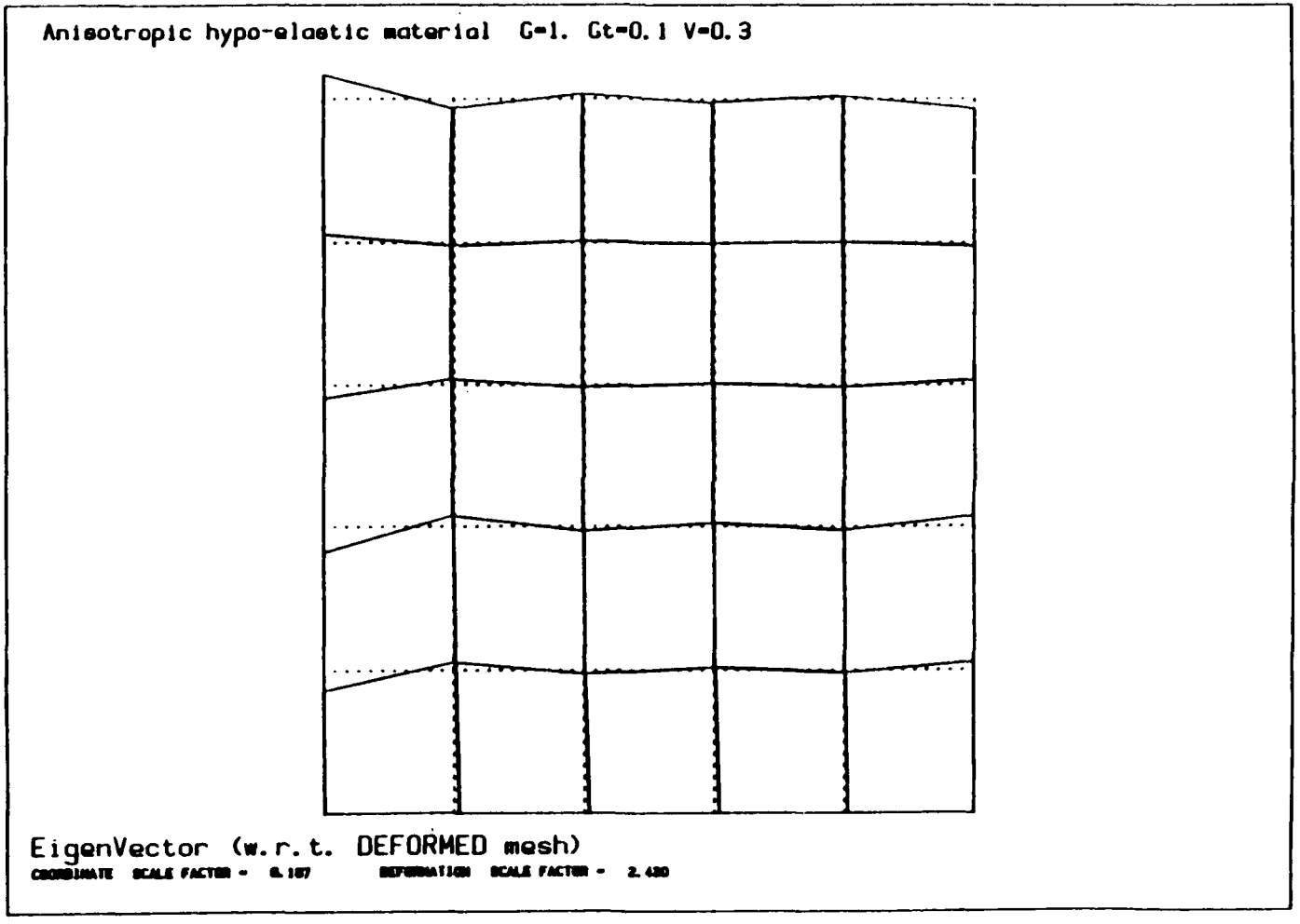

Figure 9g. Seventh eigenmode for a 25 elements model of anisotropic hypo-elastic material.

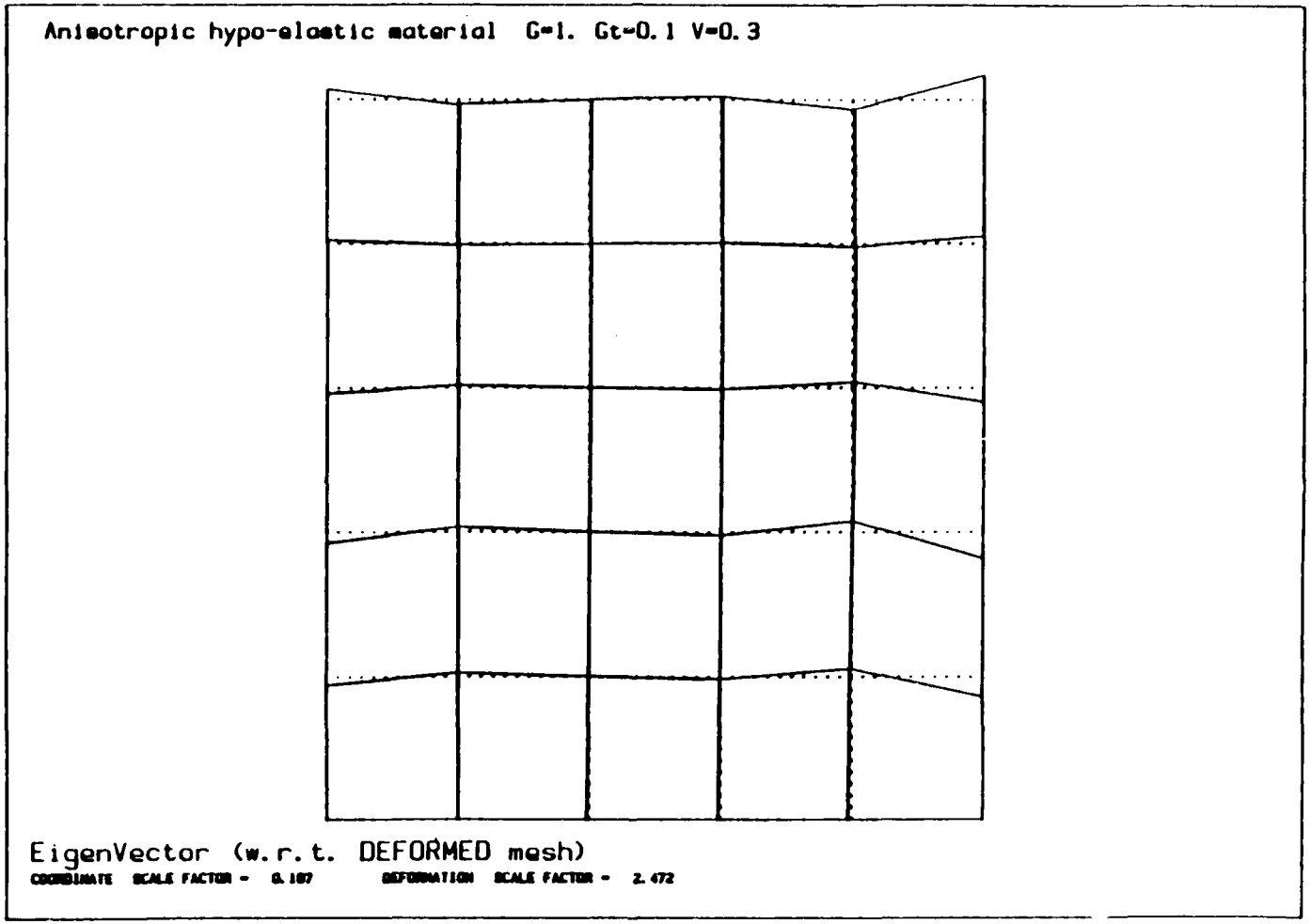

Figure 9h. Eigth eigenmode for a 25 elements model of anisotropic hypo-elastic material.

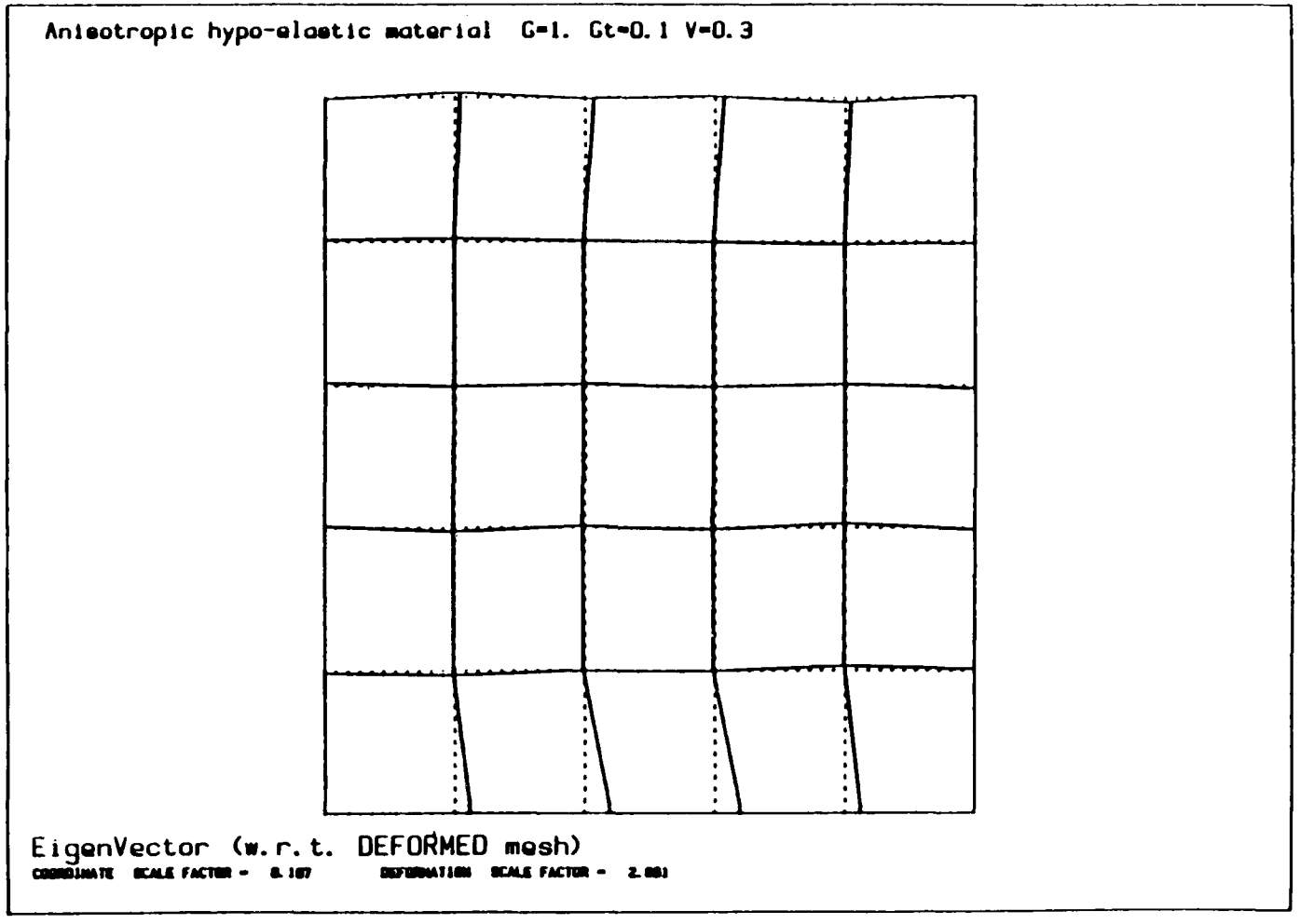

Figure 9i. Ninth eigenmode for a 25 elements model of anisotropic hypo-elastic material.

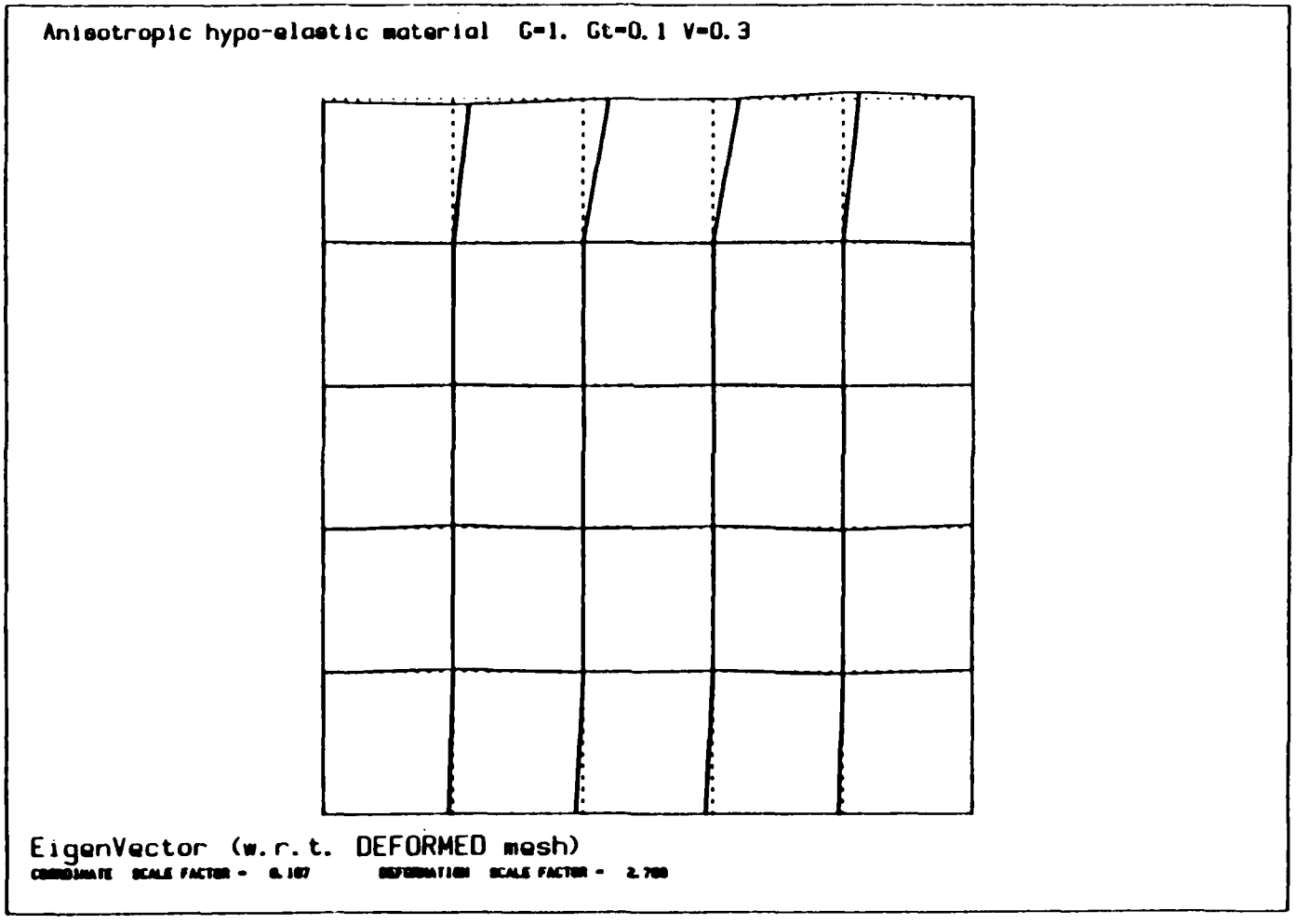

Figure 9j. Tenth eigenmode for a 25 elements model of anisotropic hypo-elastic material.

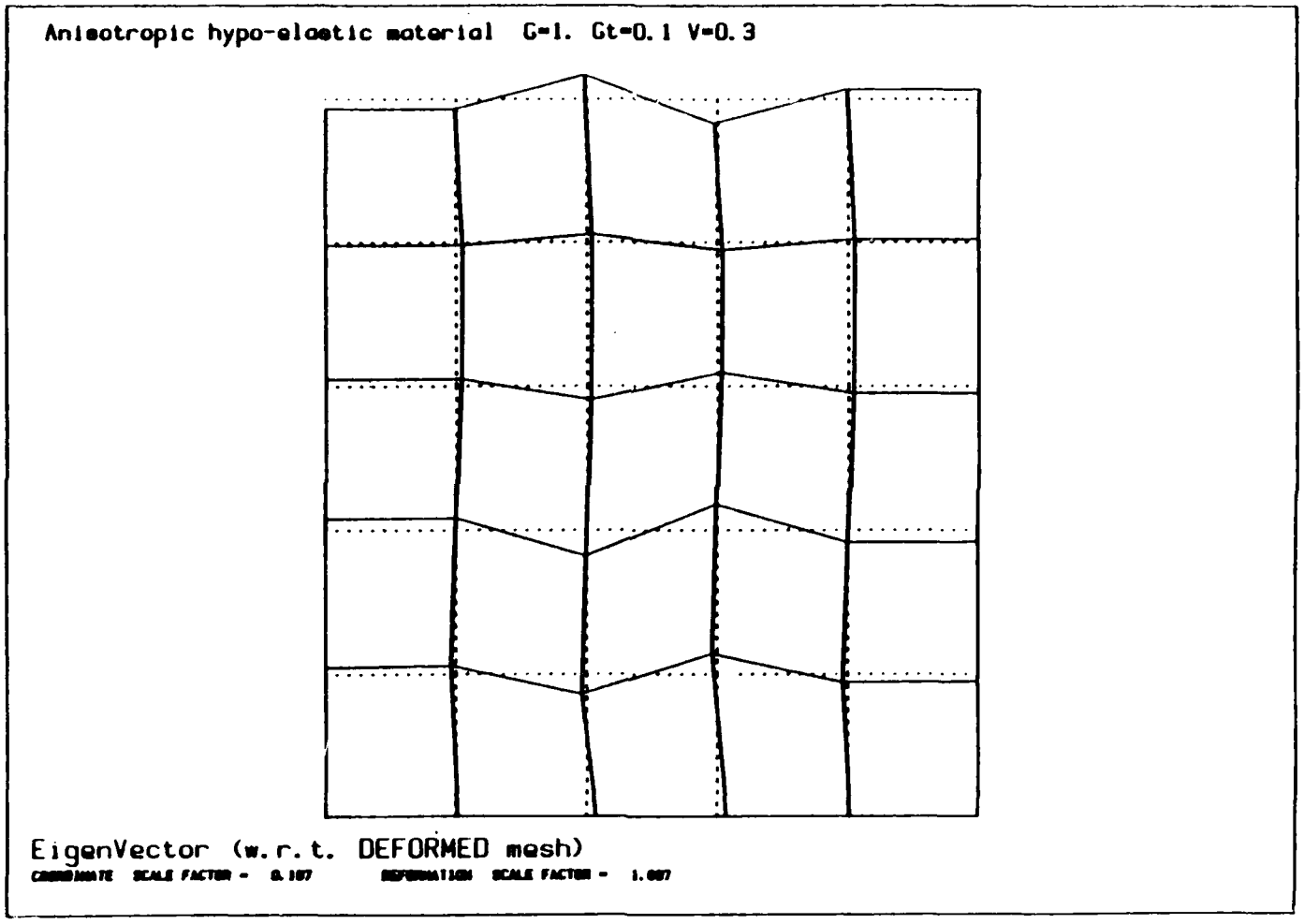

Figure 9k. Eleventh eigenmode for a 25 elements model of anisotropic hypo-elastic material.

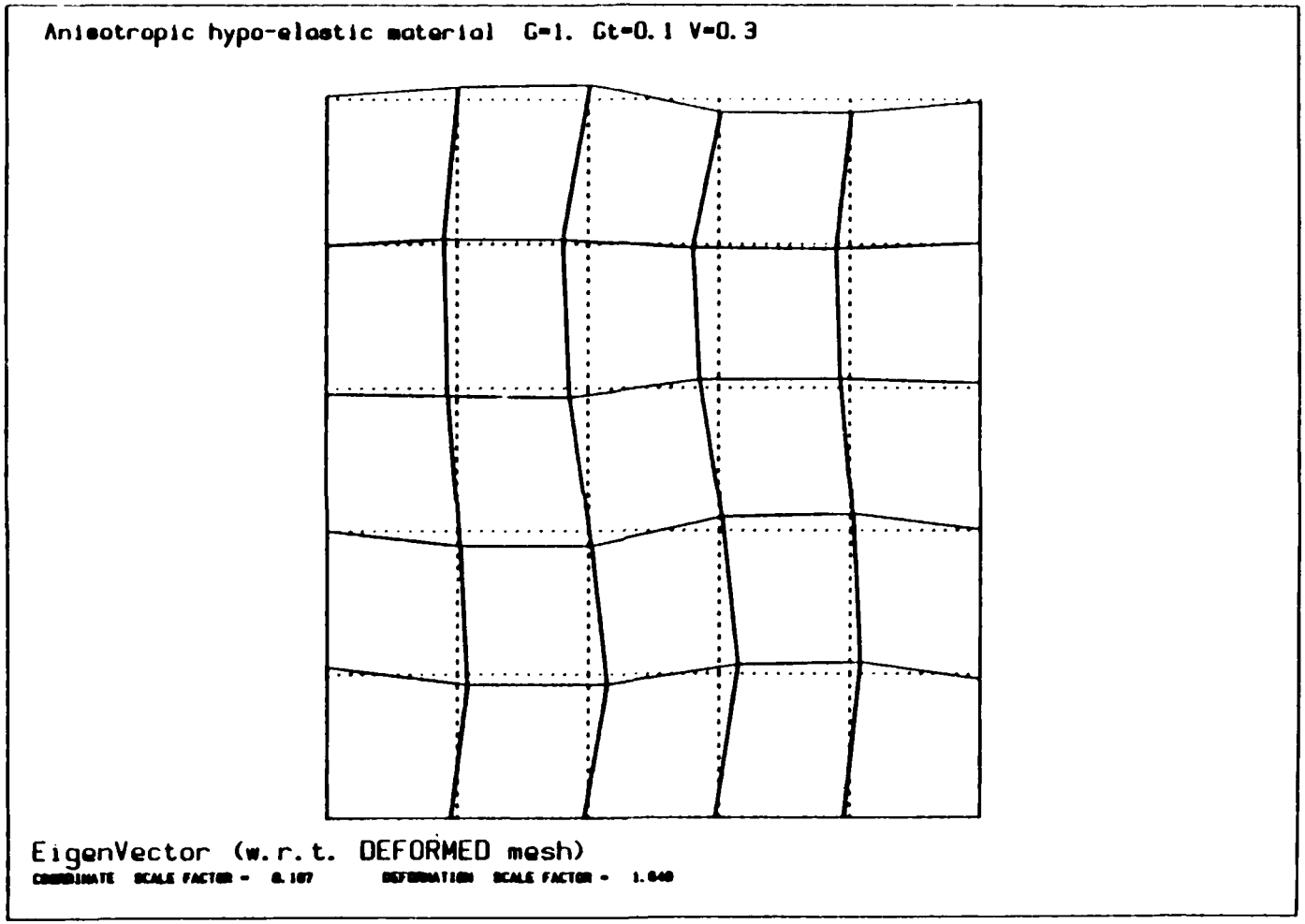

Figure 91. Twelfth eigenmode for a 25 elements model of anisotropic hypo-elastic material.

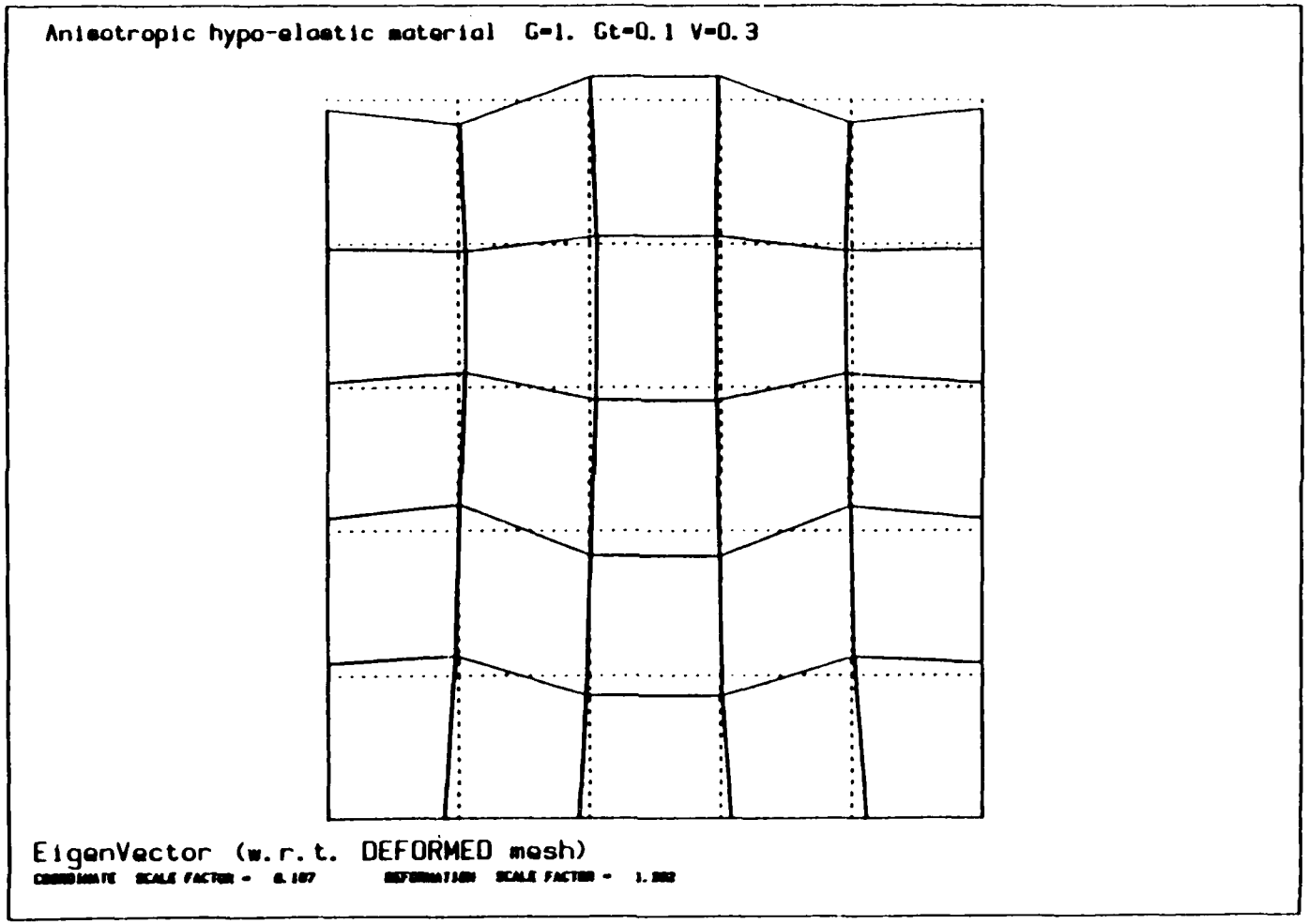

Figure 9m. Thirteenth eigenmode for a 25 elements model of anisotropic hypo-elastic material.

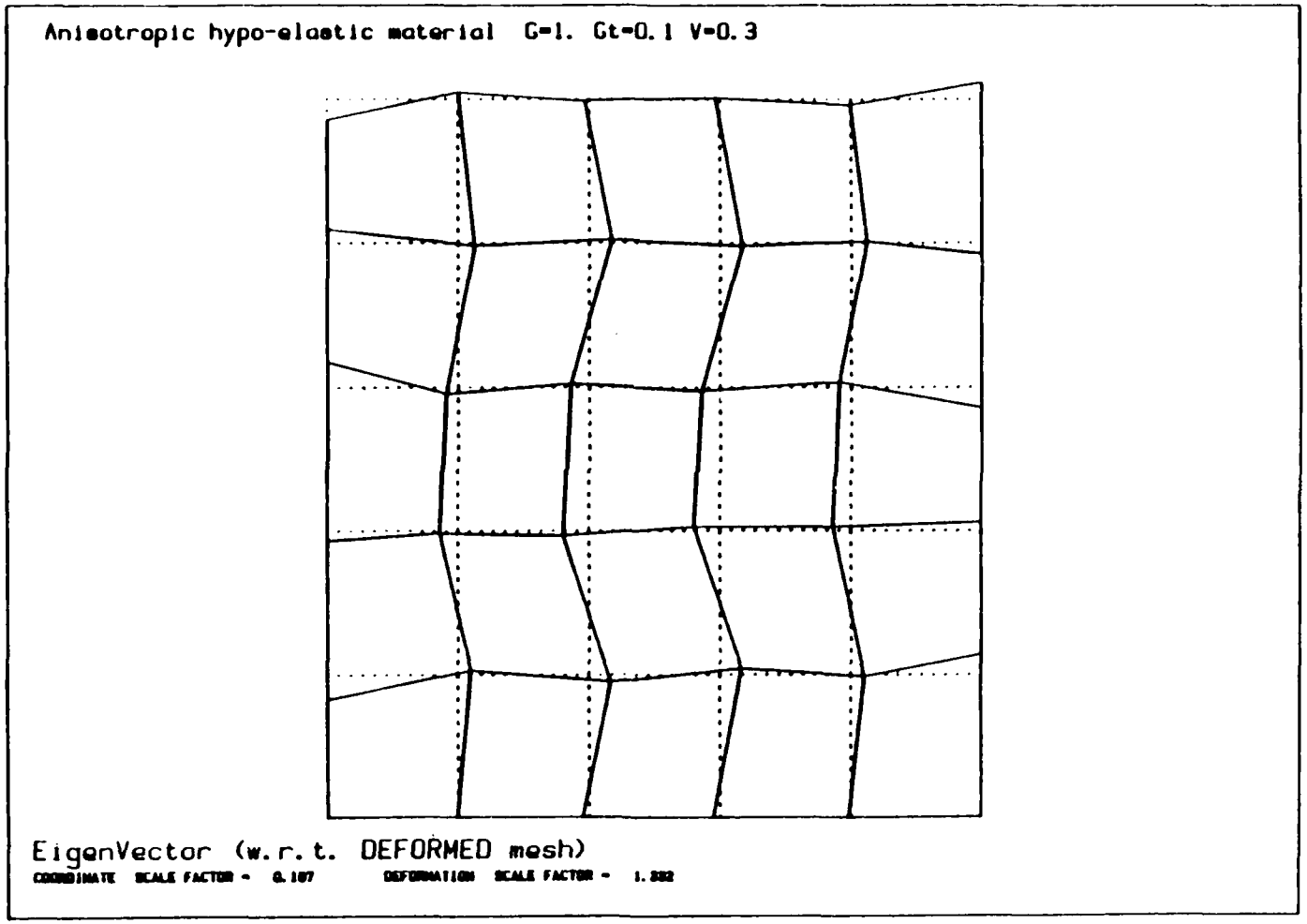

Figure 9n. Fourteenth eigenmode for a 25 elements model of anisotropic hypo-elastic material.

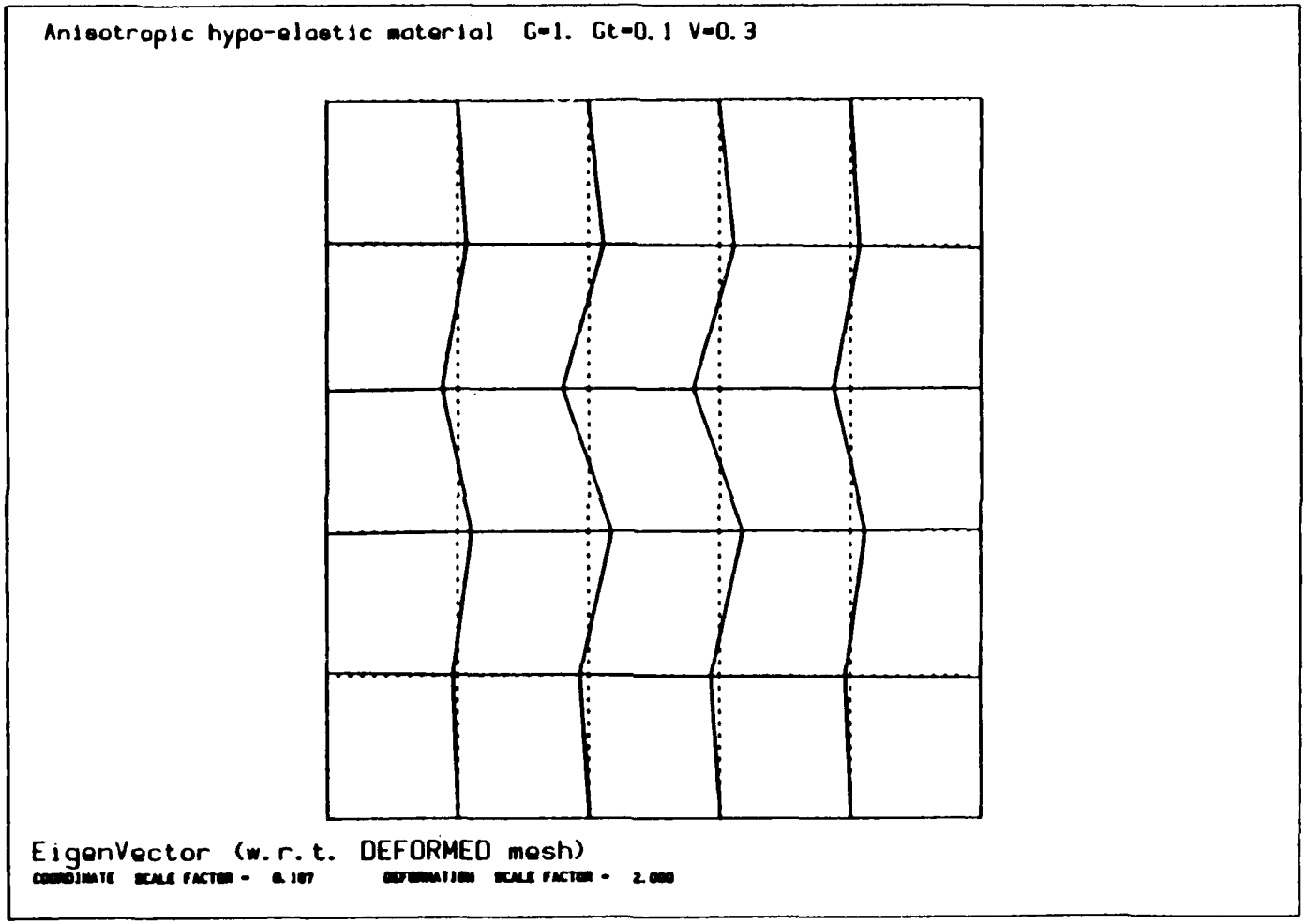

Figure 9o. Fifteenth eigenmode for a 25 elements model of anisotropic hypo-elastic material.

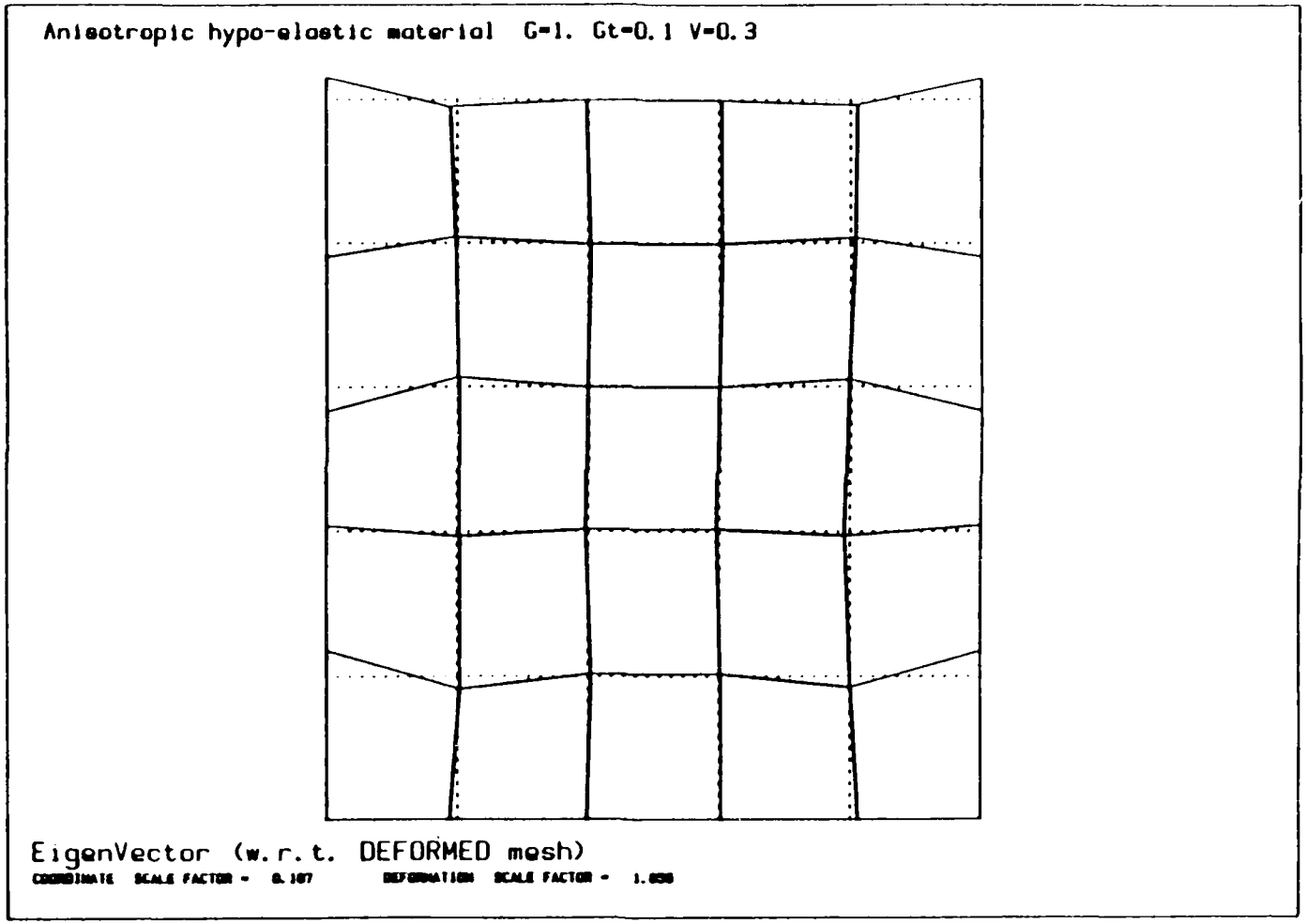

Figure 9p. Sixteenth eigenmodes for a 25 elements model of anisotropic hypo-elastic material.

away from each corner in the x_1 and x_2 directions, which was not observed in the case of the half-space. Following these two first modes, four surface modes similar to the ones found by Biot, 1965, are shown in Figs 9c to 9f. The surface wave has the shortest wave length in Fig.9c. This minimum wave length, which is associated with the lowest eigenvalue, is directly related to the number of nodes on the free surface. Following the surface modes, four unexpected modes, which are not mentioned in any analytical work, are shown in Figs. 9g to 9i. These unexpected modes are associated with edges and not with the top free surface. As shown in Figs 9g to 9i each edge of the block has a similar mode. In order to designate this new type of mode, a new term has been coined - edge mode. Following these edge modes, the volume modes are shown in Figs 9j to 9p. The volume modes correspond to wavy amplitude within the volume of the block, which does not decrease within the material volume. Biot (1965) calls these volume modes internal buckling modes. The correspondence between the eigenvalues of Table 5 and the types of mode is summarized on the real axis of Fig.10, which has been blown up between 0 and 1. As shown in Table 5 and Fig.10, all the eigenvalues are real. The minimum and maximum values are 0.01397 and 14.28, respectively. In a bifurcation analysis, all these modes are not meaningful and only the modes with the eigenvalues close to zero, are important. However, as it is shown in Fig.6, there may be several modes with closely spaced eigenvalues, which may define several possible bifurcated branches for the discretized material. This multiple bifurcation is expected in the case of surface buckling. Biot, 1965, found that there is an infinite number of surface waves which contribute to the surface buckling.

In the case of the anisotropic hypo-elastic material, the six first surface modes may contribute to the instability. According to the presence and the relative rank of surface modes with

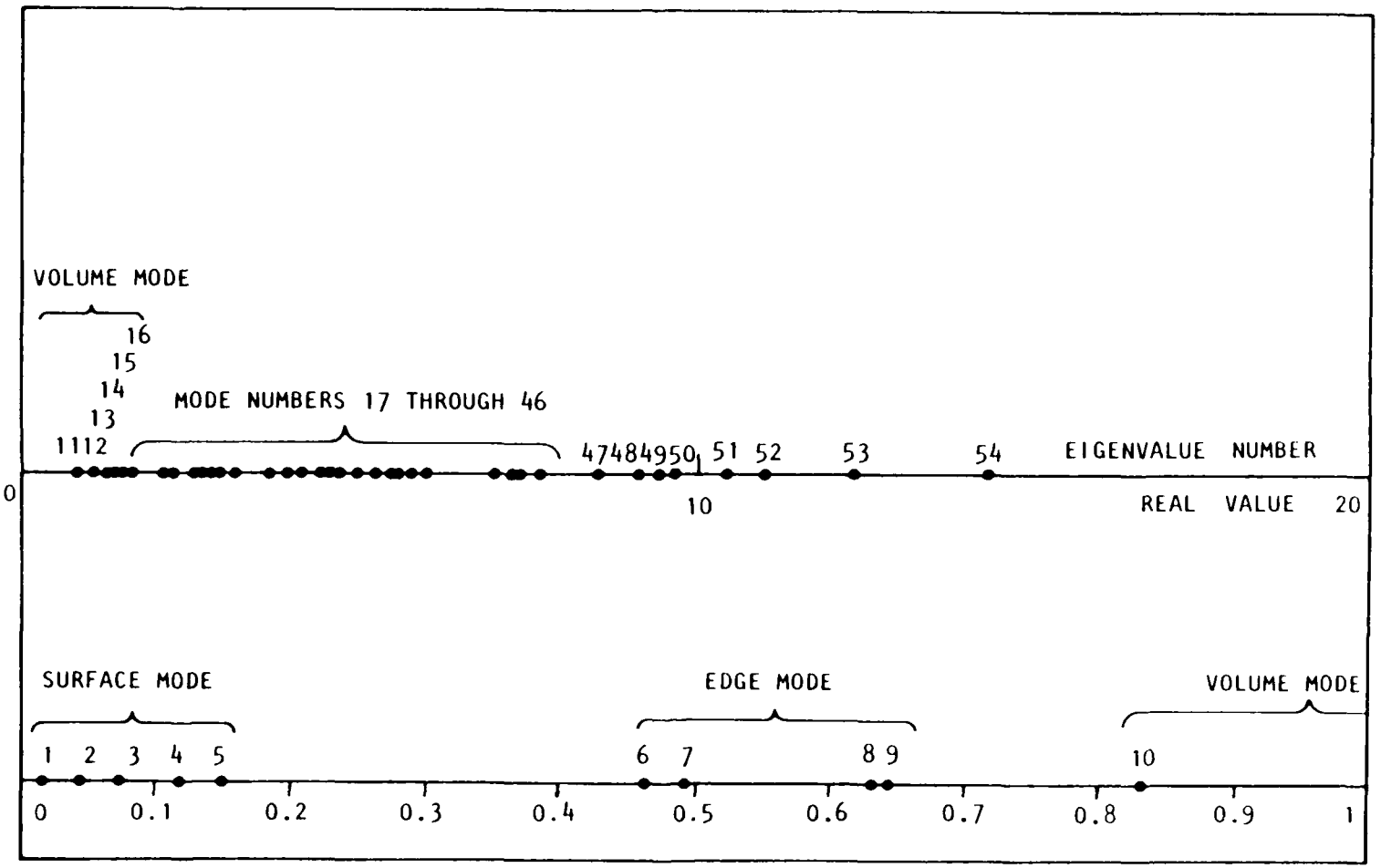

Figure 10. Spectrum of the eigenvalues for 25 elements model of anisotropic hypo-elastic material.

respect to other types of modes, it may be concluded that isotropic and anisotropic hypo-elastic materials are prone to surface instability during the wedge test. However, a similar conclusion cannot be reached in the case of the particular elastoplastic model which was selected in the previous section.

Table 4. Eigenvalues of the stiffness matrix at the onset of surface instability for a 4 elements models of isotropic hypo-elastic material.

Mode No	Eigenvalues	Figure No	Mode No	Eigenvalues	Figure No
1	-0.07849	8a	6	3.315	
2	0.2902	8b	7	6.838	
3	0.05912	8c	8	9.320	
4	0.8506	8d	9	18.99	8e
5	1.320				

Table 5. Eigenvalues of the stiffness matrix at the onset of surface instability for a 25 elements models of anisotropic hypo-elastic material.

Mode No	Eigenvalues	Type	Mode No	Eigenvalues
1	0.01397	surface	28	2.748
2	0.03961		29	2.795
3	0.07393		30	2.880
4	0.1136		31	3.078
5	0.1469		32	3.617
6	0.4620	edge	33	3.872
7	0.4941		34	4.076
8	0.6301		35	4.399
9	0.6417		36	4.471
10	0.8335	volume	37	4.880
11	1.031		38	5.183
12	1.077		39	5.454
13	1.131		40	5.525
14	1.229		41	5.684
15	1.246		42	5.920
16	1.330		43	6.998
17	1.561		44	7.212
18	1.620		45	7.351
19	1.654		46	7.582
20	2.017		47	8.503
21	2.073		48	9.119
22	2.094		49	9.455
23	2.138		50	9.625
24	2.230		51	10.40
25	2.348		52	11.00
26	2.472		53	12.31
27	2.648		54	14.28

SECTION 4

INFLUENCE OF MATERIAL MODELLING ON SURFACE INSTABILITY

The present section describes the influence of the modelling of material behavior on the surface instability of the wedge test. The following constitutive equations have been used to simulate the material behavior:

1. fully isotropic hypo-elastic materials, with two material constants
2. transversely isotropic hypo-elastic material, with three material constants
3. isotropic elastoplastic model derived from the flow theory of plasticity with five material constants

The parametric study, which consisted of estimating the influence of various models and their respective material constants on the buckling load of the wedge test, has been carried out by using the computer program BIF. Before presenting the principles of the program BIF, the analysis of plane strain surface instability is summarized in the form introduced by Horii and Nemat-Nasser (1982). Mathematical derivations can be found in the paper by Horii and Nemat-Nasser (1982).

4.1 PLANE-STRAIN SURFACE INSTABILITY OF HALF-SPACE.

In order to abbreviate the mathematical notations, it is convenient to define the following coefficients:

$$d_1 = C_{1111} - \tau_1 \tag{16a}$$

$$d_2 = C_{2222} - \tau_2 \tag{16b}$$

$$d_3 = C_{1212} - (\tau_1-\tau_2)/2 \qquad (16c)$$

$$d_4 = C_{1212} - (\tau_1+\tau_2)/2 \qquad (16d)$$

$$d_5 = C_{1212} + (\tau_1-\tau_2)/2 \qquad (16e)$$

$$d_6 = C_{1212} + (\tau_1+\tau_2)/2 \qquad (16f)$$

$$d_7 = C_{1122} \qquad (16g)$$

$$d_8 = C_{2211} \qquad (16h)$$

τ_1 and τ_2 are the components of the Kirchhoff stress. C_{ijkl} are the coefficients of the rate type constitutive equations. By using the coefficients d_i's, the equilibrium equations of incremental stress in plane strain condition are:

$$d_1 v_{1,11} + d_3 v_{1,22} + (d_4+d_7) v_{2,12} = 0 \qquad (17a)$$

$$d_5 v_{2,11} + d_2 v_{2,22} + (d_4+d_8) v_{1,12} = 0 \qquad (17b)$$

v_1 and v_2 are the velocity components. The subscript "," represents spatial derivative:

$$v_{k,ij} = \frac{\partial^2 v_k}{\partial x_i \partial x_j} \qquad i,j,k=1,2 \qquad (17c)$$

The geometry of the half-space under compressive stress is shown in Fig.11. It is supposed to be infinite in the vertical direction. Note that the coordinates axis x_1-x_2 have been replaced by x-y axis. On the edges x= ±a, a uniform stress τ_1 is prescribed in the x direction without shear traction. A uniform and constant stress τ_2 is applied on the top surface (y=0). The notion of surface instability means that the deformation is confined close to the top surface, i.e., the velocity field is fading exponentially with x, vanishing at infinite distance from the top surface. Horii and Nemat-Nasser (1982) assumed that the inception of instable deformation is defined by the following velocity

field:

$$v_1 = A\, e^{i\alpha x}.e^{-\alpha Z y} \tag{18a}$$

$$v_2 = B\, e^{i\alpha x}.e^{-\alpha Z y} \tag{18b}$$

α is real and positive. When the complex variable Z has a real part strictly positive, the velocity (v_1, v_2) varies as cosine or sine in the x-direction and its amplitude decays exponentially with the depth y. When Z is purely imaginary, the velocity (v_1, v_2) varies as cosine and sine in the x and y directions but its amplitude does not decay with depth. The former case corresponds to surface instability, while the latter case corresponds to volume instability.

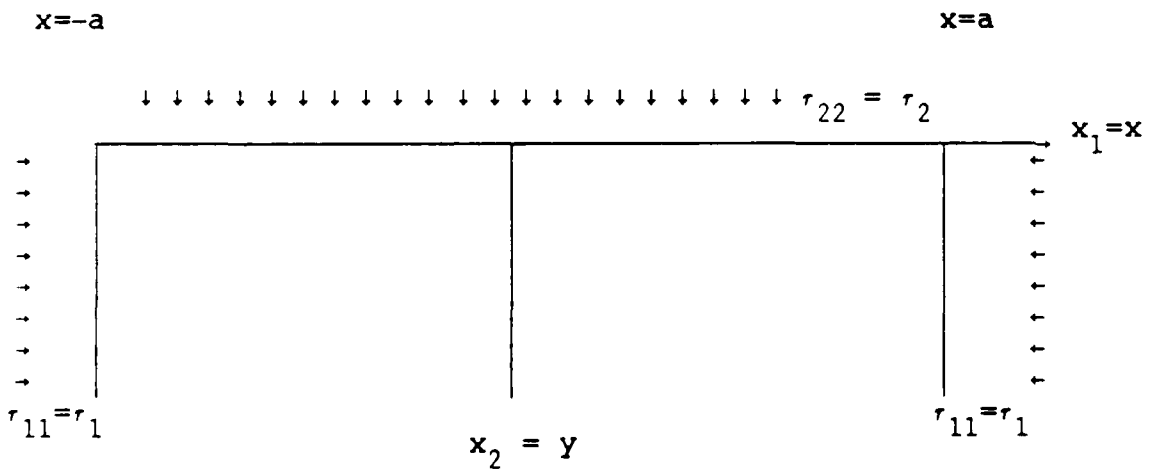

Figure 11. Half-space under compressive stress.

Since the velocity field must decay with depth for surface instability, the velocity field becomes:

$$v_1 = (A_2 e^{-\alpha Z_1 y} + A_4 e^{-\alpha Z_2 y}) e^{i\alpha x} \tag{19a}$$

$$v_2 = (-K_1 A_2 e^{-\alpha Z_1 y} - K_2 A_4 e^{-\alpha Z_2 y}) e^{i\alpha x} \tag{19b}$$

The coefficients Z_1, Z_2, K_1, and K_2 are found by substituting (19) into (17). Z_1 and Z_2 are the complex or real solutions with positive real part of the following equation:

$$aZ^4 + bZ^2 + c = 0 \tag{19c}$$

The coefficients of the quadratic equation (19c) are:

$$a = d_2 d_3 \tag{19d}$$

$$b = -d_3 d_5 - d_1 d_2 + (d_4+d_7)(d_4+d_8) \tag{19e}$$

$$c = d_1 d_5 \tag{19f}$$

The coefficients K_1 and K_2 are:

$$K_1 = \frac{-d_1 + Z_1^2 d_3}{iZ_1(d_4+d_7)} \qquad K_2 = \frac{-d_1 + Z_2^2 d_3}{iZ_2(d_4+d_7)} \tag{19g}$$

The imposition of the boundary conditions of Fig.11 leads to two linear equations with two unknowns A_2 and A_4:

$$(id_8 - d_2 K_1 Z_1) A_2 + (id_8 - d_2 K_2 Z_2) A_4 = 0 \tag{20a}$$

$$(-d_3 Z_1 + iK_1 d_4) A_2 + (-d_3 Z_2 + iK_2 d_4) A_4 = 0 \tag{20b}$$

In order to obtain a nontrivial solution, the determinant of this system must vanish. If r_2 is fixed and if the coefficients d_i are assumed to be function of r_1 only, then the determinant of (20) is

a function of τ_1:

$$f(\tau_1) = id_3(Z_1-Z_2)(d_5(d_8d_7-d_2d_1)-Z_1Z_2d_2(d_4^2-d_3d_5)) \qquad (21a)$$

The buckling stress of the half-space can be obtained by solving the following nonlinear equation of the variable τ_1

$$f(\tau_1) = 0 \qquad (21b)$$

In the case of hypo-elastic material, all coefficients d_i are functions of τ_1. However, this dependence does not hold for elastoplastic models due to the influence of τ_3. Horii and Nemat-Nasser (1982) solved this problem by assuming that there is no plastic flow in x_3 direction.

4.2 COMPUTATION OF BUCKLING LOAD WITH THE PROGRAM BIF.

Based upon the analytical development of Horii and Nemat-Nasser (1982), the program BIF calculates the buckling stress of the half space and plots the corresponding buckling eigenmode. BIF does not discretize the half space in finite elements but solves by iteration the nonlinear buckling equation of the infinite half space for various material models. That is to say that BIF provides analytical results which can be compared to our finite element results. In order to solve the nonlinear equation (21) the computer program increases the applied stress τ_1 in a segment $[\tau_{min}, \tau_{max}]$ which is specified by the user. Starting from τ_{min} and moving by increment $\Delta\tau = (\tau_{max}-\tau_{min})/n$ where n is a specified integer, it detects the stress level for which the real or imaginary part of the equation (21) changes sign, then iterates by using Regula-Falsi method until the equation (21) is satisfied. After the calculation of the buckling stress, the buckling

eigenmode can be plotted in a way similar to finite element post-processing.

The following sections summarize for each model the influence of the material constants on surface instability.

4.3 SURFACE INSTABILITY OF ISOTROPIC HYPO-ELASTIC MODEL.

Isotropic hypo-elastic material have two material constants:

G shear modulus

ν Poisson's ratio

If the stress on the free surface is zero $\tau_2=0$, the coefficients d_1 to d_8 are:

$$d_1 = 2G + \lambda - \tau_1 \quad (22a)$$

$$d_2 = 2G + \lambda \quad (22b)$$

$$d_3 = G - \tau_1/2 = d_4 \quad (22c)$$

$$d_5 = G + \tau_1/2 = d_6 \quad (22d)$$

$$d_7 = d_8 = \lambda \quad (22e)$$

As shown in Fig.12, the buckling stress τ_{11}, which is normalized by the shear modulus G, increases with Poisson's ratio and depends on the stress applied on the surface of the half-space. As it is to be expected, compressive stresses acting on the half-space surface increase the buckling load while tensile stresses decrease it. Note that the buckling stress is larger than the shear modulus G, which is unrealistic for most Rock Mechanics applications. The eigenmodes or buckling modes, which describe the velocity field at the inception of surface instability, have been calculated by using BIF. The mathematical expression of these velocity fields can be found in Table.6. Three buckling modes of the half-space are plotted in Figs.13a to 13c for three different values of the wave length parameter α : $\pi/2a$, $3\pi/2a$, and $5\pi/2a$. The eigenmodes are only plotted inside a square window of depth 2a

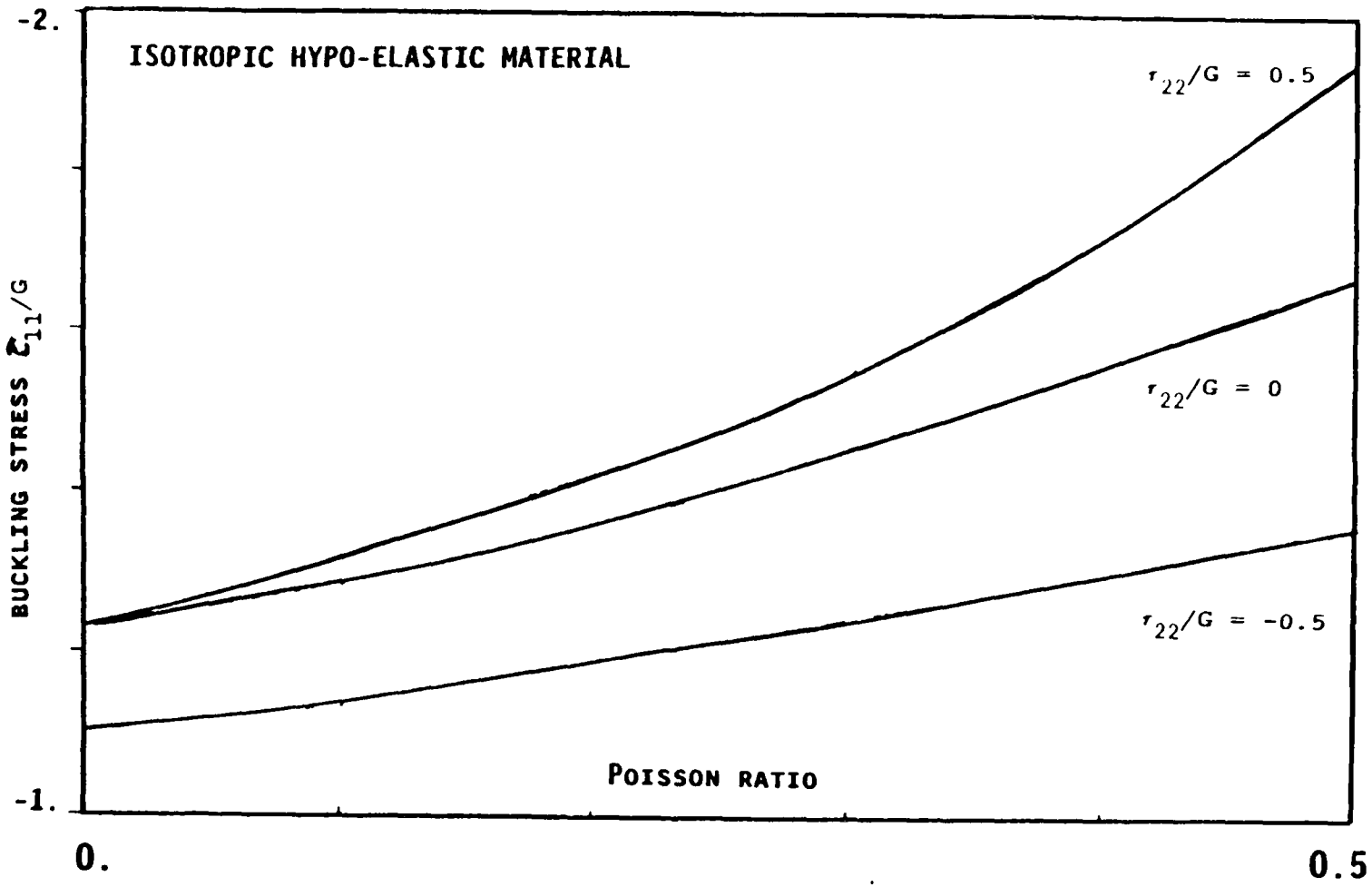

Figure 12. Analytical buckling stress τ_{11}/G of elastic half-space versus Poisson ratio ν for various applied pressure on free surface.

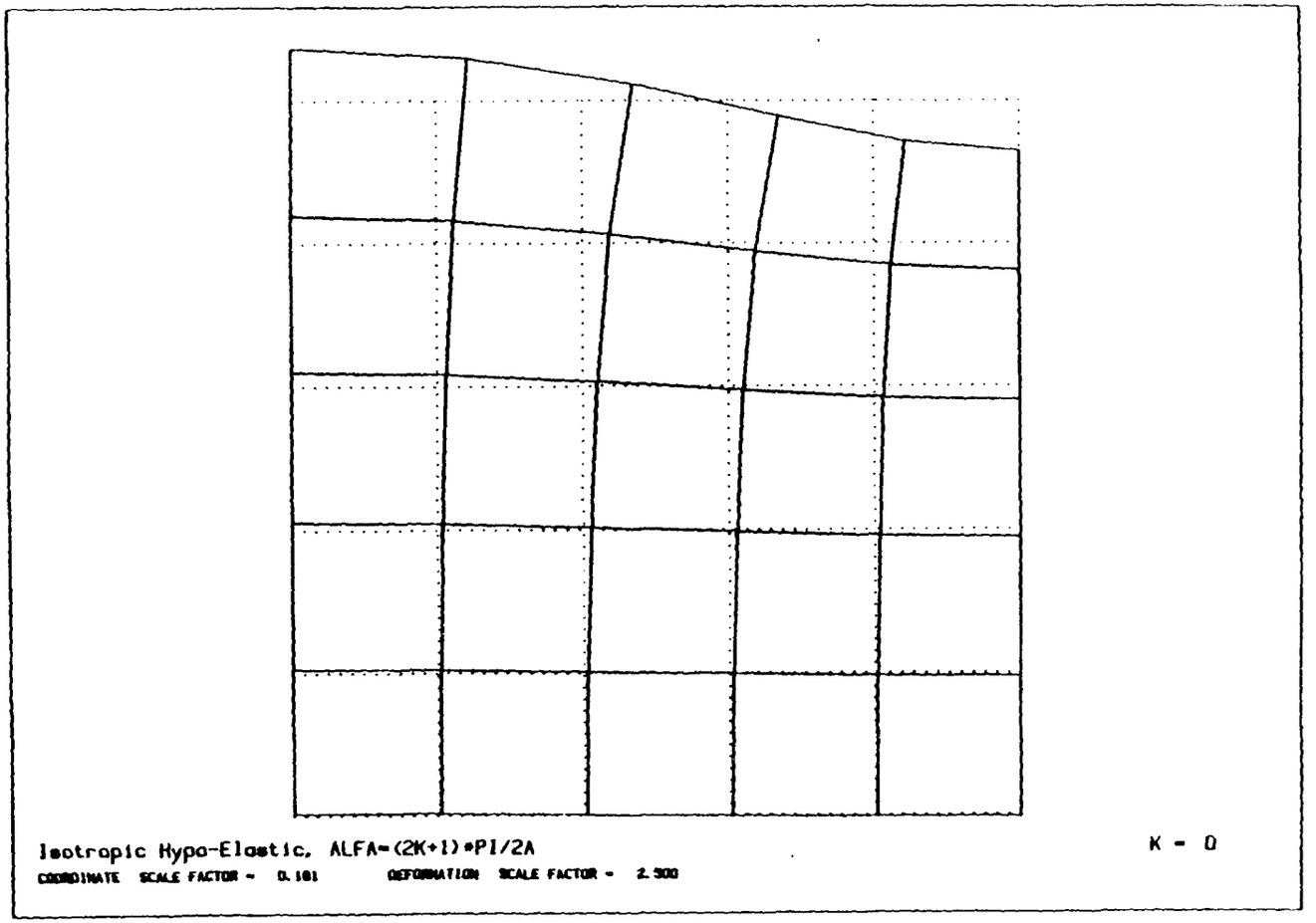

Figure 13a. First eigenmode of the half space for isotropic hypo-elastic model.

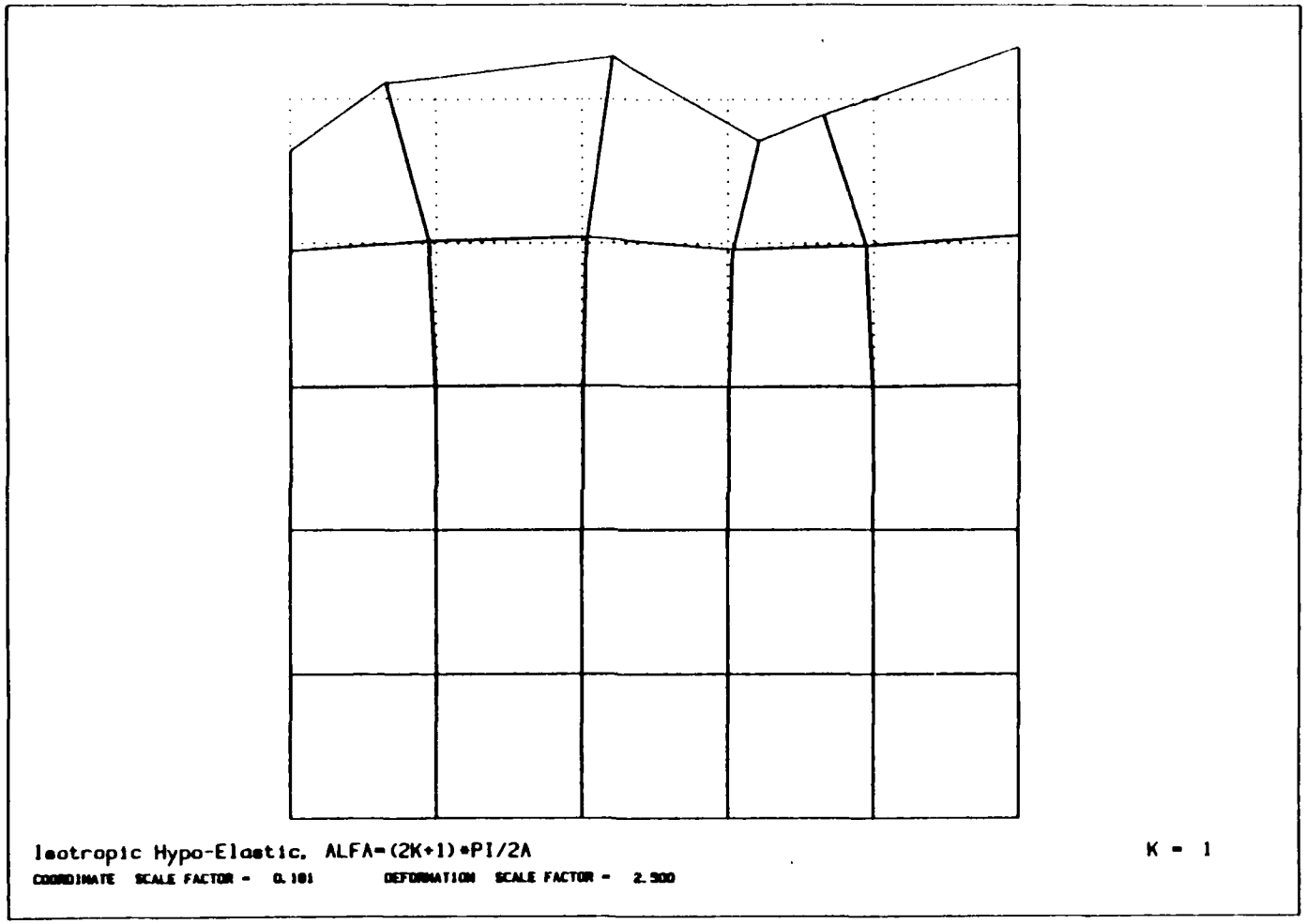

Figure 13b. Second eigenmode of the half space for isotropic hypo-elastic model.

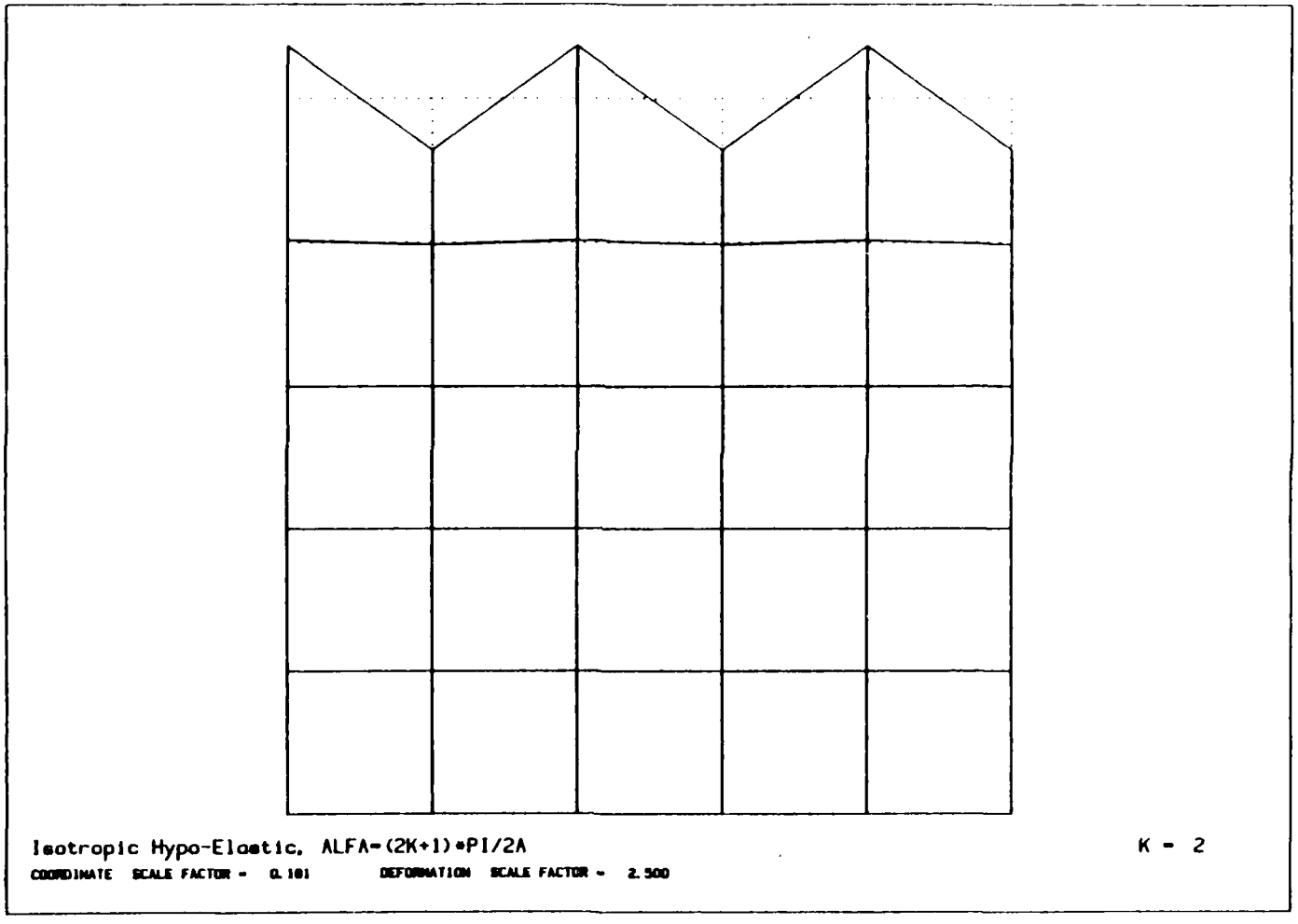

Figure 13c. Third eigenmode of the half space for isotropic hypo-elastic model.

which is centered on the y-axis. The dashed and full lines represent the positions of a uniform grid before and after the emergence of surface instability, respectively. As shown in Figs.13, the velocity amplitude decays rapidly with the depth y. The smaller the surface wave length is, the faster the velocity amplitude decays with depth. Note that the eigenmodes of the half-space shown in Figs.13 obey almost perfectly the boundary conditions of the wedge test of Fig.2, although they are not required to do so. The boundary conditions are slightly violated at the lower boundary of Fig.13a: the first mode of the half-space interferes more than the other modes with the boundary conditions of a finite block. In the absence of an analytical solution for the surface instability of block of finite size, this incompatibility between eigenmode and boundary conditions may explain some of the observations made during the finite element analysis of the wedge test. It may explain why the surface modes have distinct eigenvalues and why the lowest eigenvalues of the stiffness matrix correspond to the smallest surface wave length.

4.4 SURFACE INSTABILITY OF ANISOTROPIC HYPO-ELASTIC MODEL.

Anisotropic hypo-elastic have three material constants:

G, G_t shear moduli in the plane of isotropy and in a plane normal to the plane of isotropy, respectively

ν Poisson's ratio

As shown in Fig.14, the normalized buckling stress decreases when the transverse shear modulus G_t decreases. The case $G/G_t = 1$ corresponds to the isotropic case. When the ratio G/G_t becomes very large, which corresponds to the case where the shear modulus G in the isotropy plane is quite larger than the transverse shear modulus G_t in a plane perpendicular to the half-space surface, the buckling stress decreases to zero but remains always smaller than

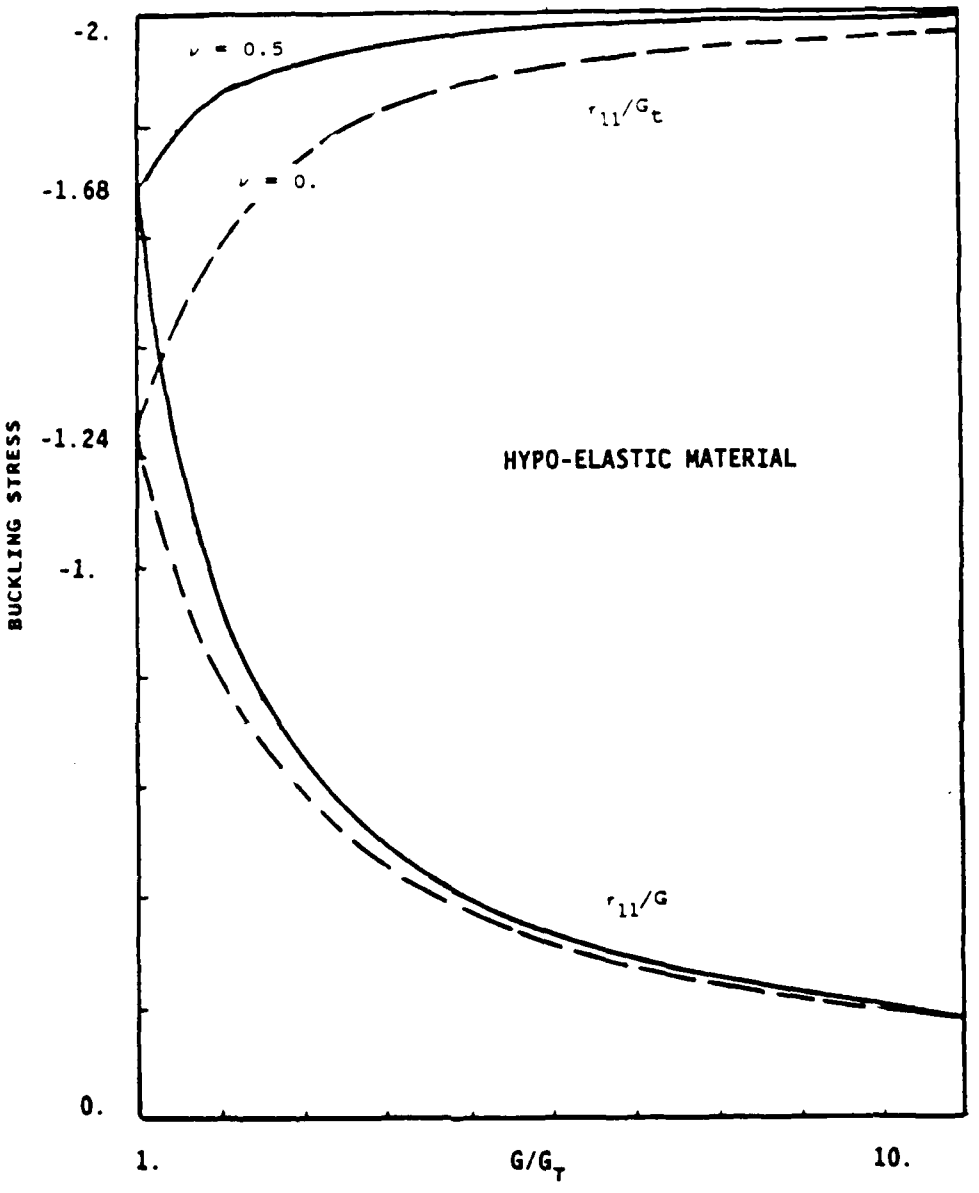

Figure 14. Analytical buckling stress τ_{11}/G of anisotropic half space versus ratio of shear moduli G/Gt for Poisson ratio ν = 0 and 0.5.

twice G_t. The buckling modes have been calculated in Table.6 and plotted in Figs.15 in the same way as the eigenmodes of the isotropic case. The velocity amplitude of Figs.15a and 15b decays faster with depth than in Figs.13, which results in a better compatibility between the buckling modes of the half space and the boundary conditions of the block of finite size of Fig.2. Note that the modes of Fig.15c and Fig.13c are identical. However, the eigenmodes of the half space of Fig.15 exhibit a larger amplitude decay with depth than the finite element eigenmodes of Figs 9c to 9f. This slight difference between analytical and numerical modes is certainly caused by the spatial discretization used in the finite element model, and could be reduced by refining the finite element mesh in the vicinity of the top surface.

4.5 SURFACE INSTABILITY FOR ELASTOPLASTIC MODEL.

The elastoplastic model used in the analysis is an isotropic elastoplastic model derived from the flow theory of plasticity. It has five material constants:

- G elastic shear modulus
- ν elastic Poisson's ratio
- μ friction coefficient i.e. slope of yield surface in the stress space (σ,τ) where σ and τ the first and second deviatoric stress invariants, respectively.
- β dilatancy parameter, i.e. slope of the plastic potential surface in the stress space (σ,τ).
- H plastic modulus

Further detail on the elastoplastic models may be found in the paper of Rudnicki & Rice (1975), or Nemat-Nasser & Horii(1982). Nemat-Nasser and Horii (1982) applied the general elastoplastic theory to describe some particular experimental data obtained on sandstones. In this particular model, the plastic modulus H is a

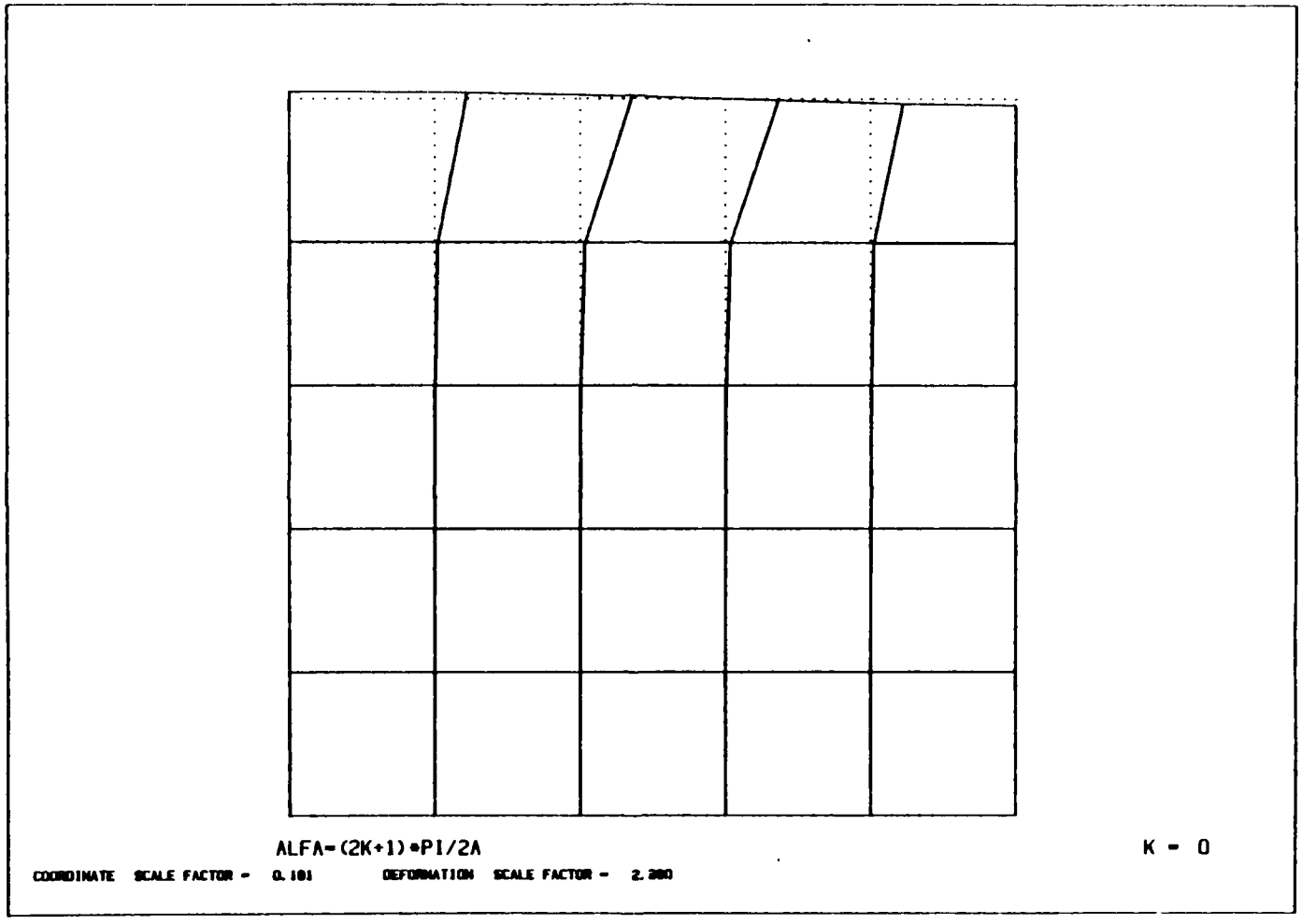

Figure 15a. First of the half space for anisotropic hypo-elastic model.

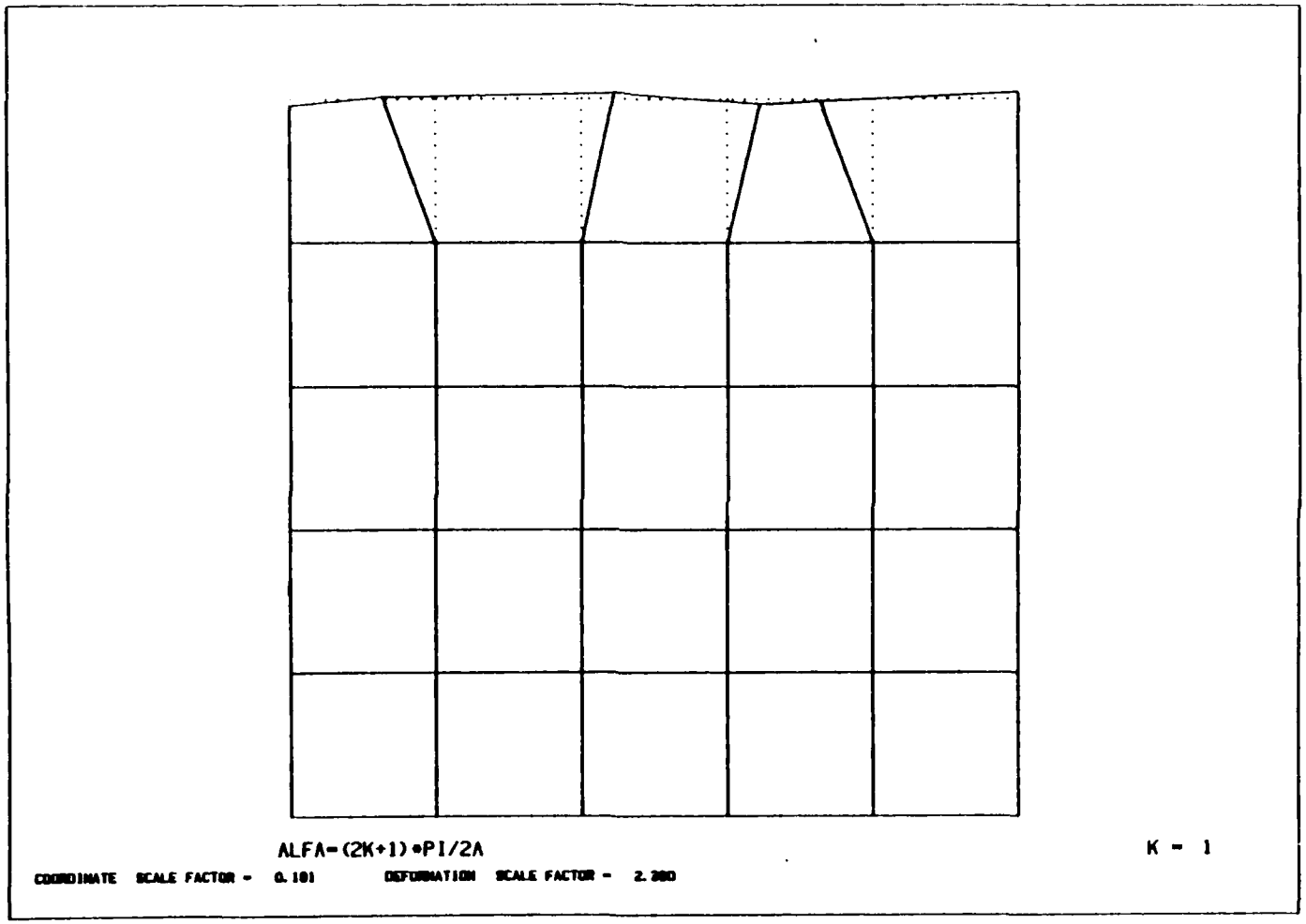

Figure 15b. Second of the half space for anisotropic hypo-elastic model.

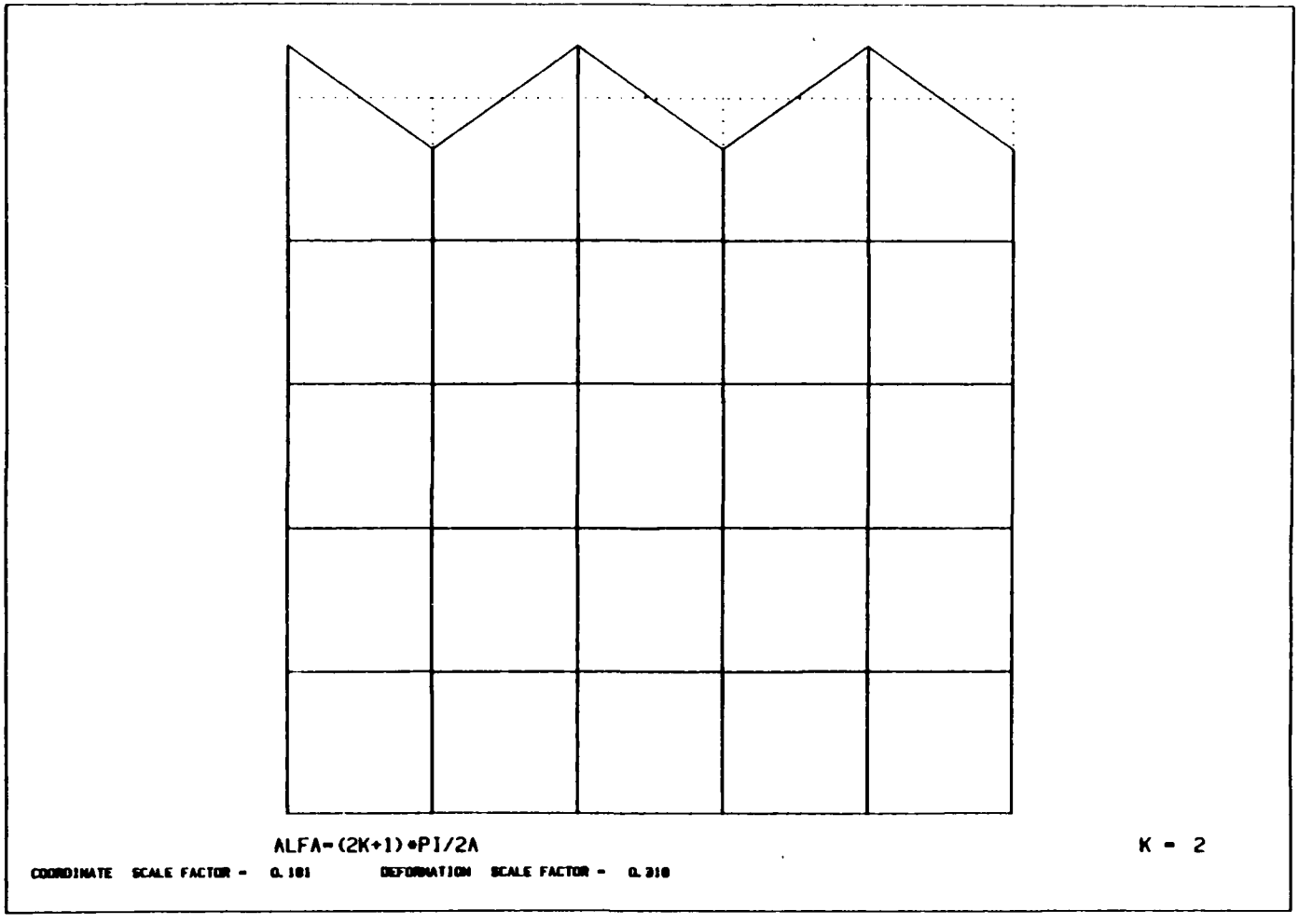

Figure 15c. Third of the half space for anisotropic hypo-elastic model.

function of the first stress invariant σ and the effective strain γ. The friction coefficient μ is a constant, while the dilatancy angle β depends on the stress level (see Horii and Nemat-Nasser, 1982, for further detail).

As shown in Fig.16, the buckling stress calculated by using elastic plastic model depends on the dilatancy angle β. For β = 0.39, which correspond to an associative flow rule since μ=0.39, the normalized buckling stress τ_1/G increases with the normalized plastic modulus H/G. In the same way as the eigenmodes of hypo-elastic models, the buckling modes of elastoplastic models have been calculated in Table.6 and plotted in Figs.17 and 18 for two values of the normalized plastic modulus H/G: 0.1 and 0.01. When H/G=0.1, the velocity amplitude of Figs.17a decays with depth but certainly not as quickly as in Figs.13 or 15. The eigenmodes of Figs.17 are not compatible with the boundary conditions of a block of finite size. When H/G=0.01, which corresponds to more plastic yielding than H/G=0.1, the eigenmodes of Figs.18 are found to exhibit a very slow decay of amplitude with depth. This slow decay with depth comes from the small real part of the root Z_1. In the case H/G=0.01 the eigenmodes of the half-space are even more incompatible with the boundary conditions of the wedge test. The wave length parameter α must be very large to compensate for the low part of the roots Z_1 and Z_2. However, in contrast to analytical solutions, finite elements are unable to increase the wave length parameter α in order to compensate for the slow amplitude decay resulting from the small real parts of Z_1 and Z_2, since the minimum wave length of the discrete system is controlled by the number of nodes on the surface as it was pointed out in Fig.9c. The combined presence of a small amplitude decay and a limited wave length parameter α explains why the surface instability of a block of finite size is difficult to obtain in presence of large plastic yielding within a discretized system.

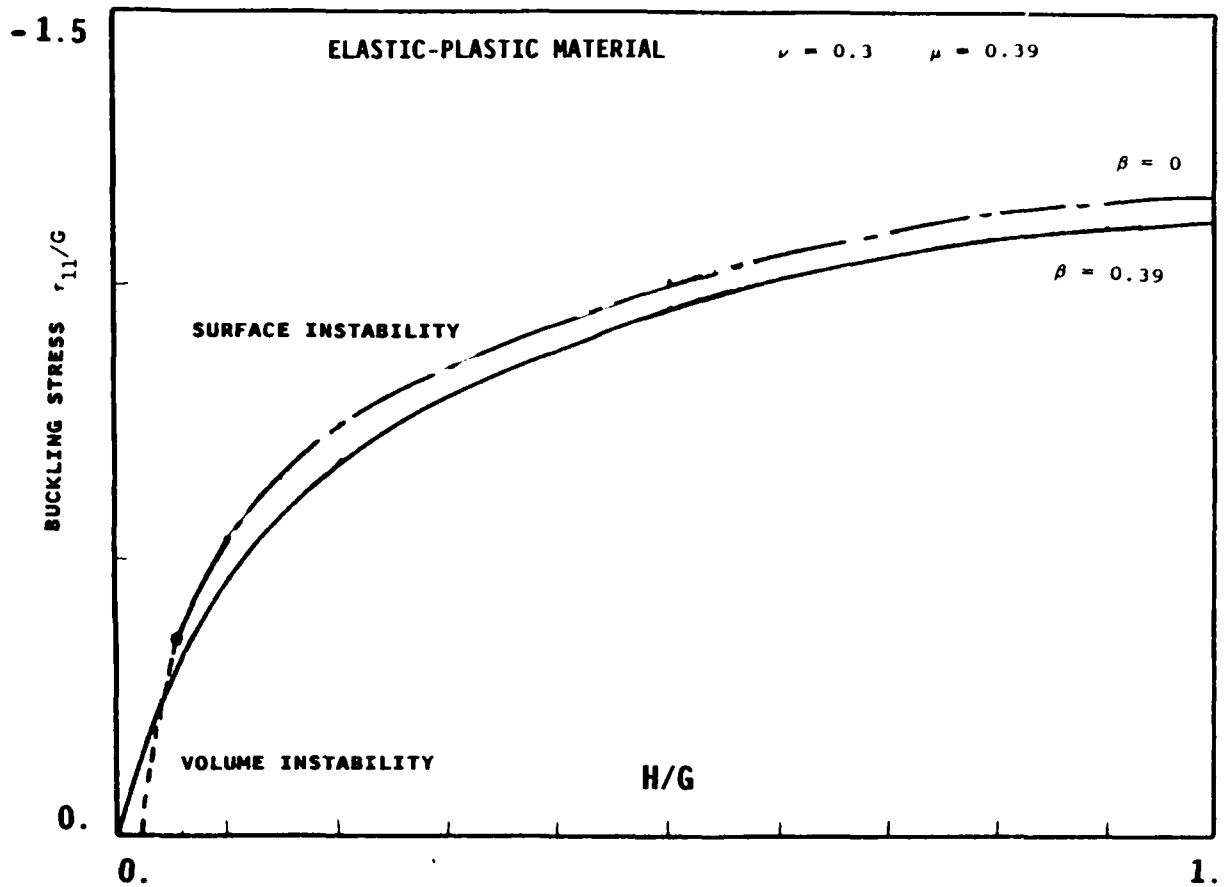

Figure 16. Buckling stress τ_{11}/G of elastoplastic Nemat-Nasser model versus normalized plastic modulus H/G for various values of dilatancy parameter β (μ friction coefficient, ν Poisson ratio).

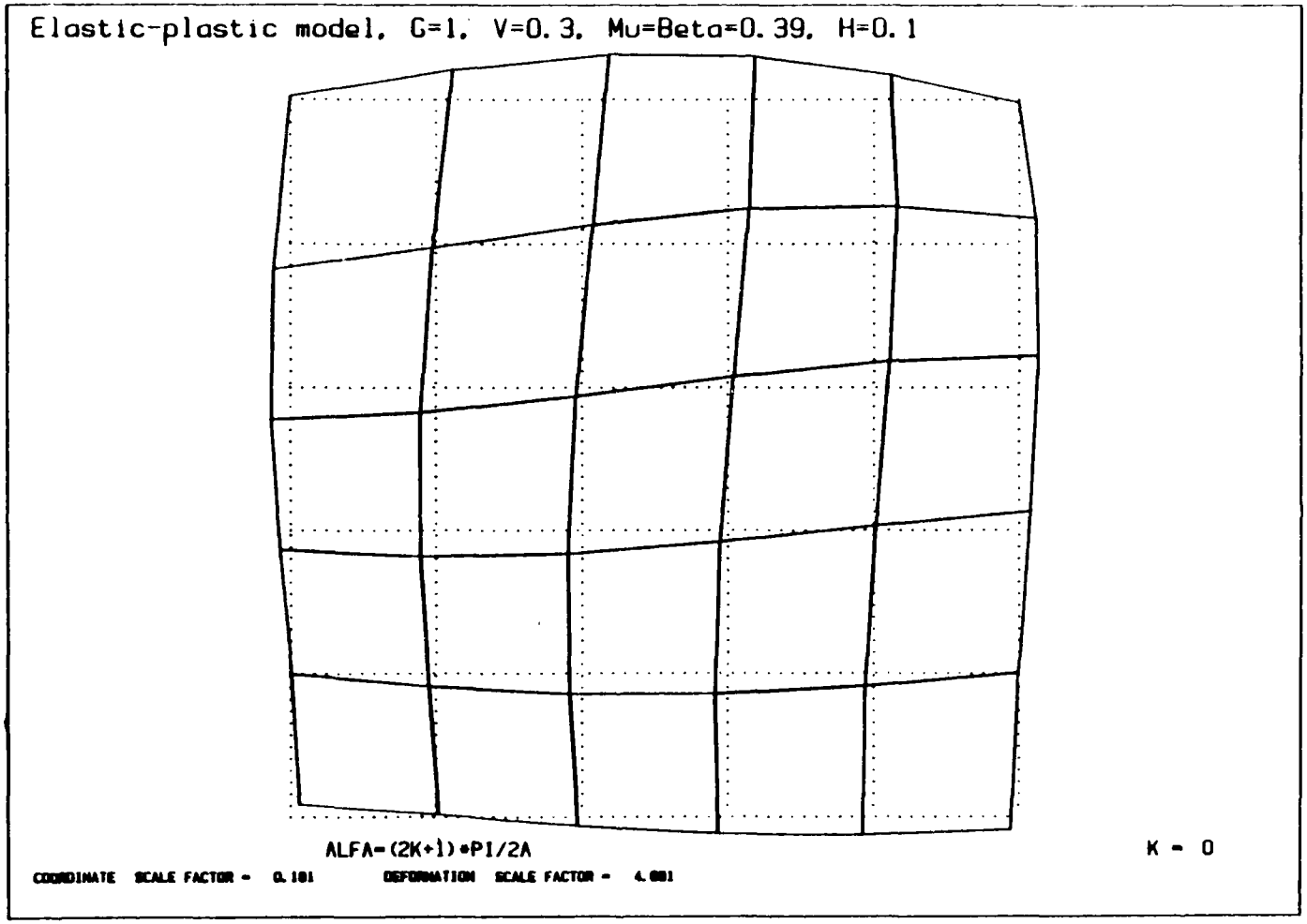

Figure 17a. First eigenmode of the half space for elastoplastic model ($\mu=\beta=0.39$, $H/G=0.1$).

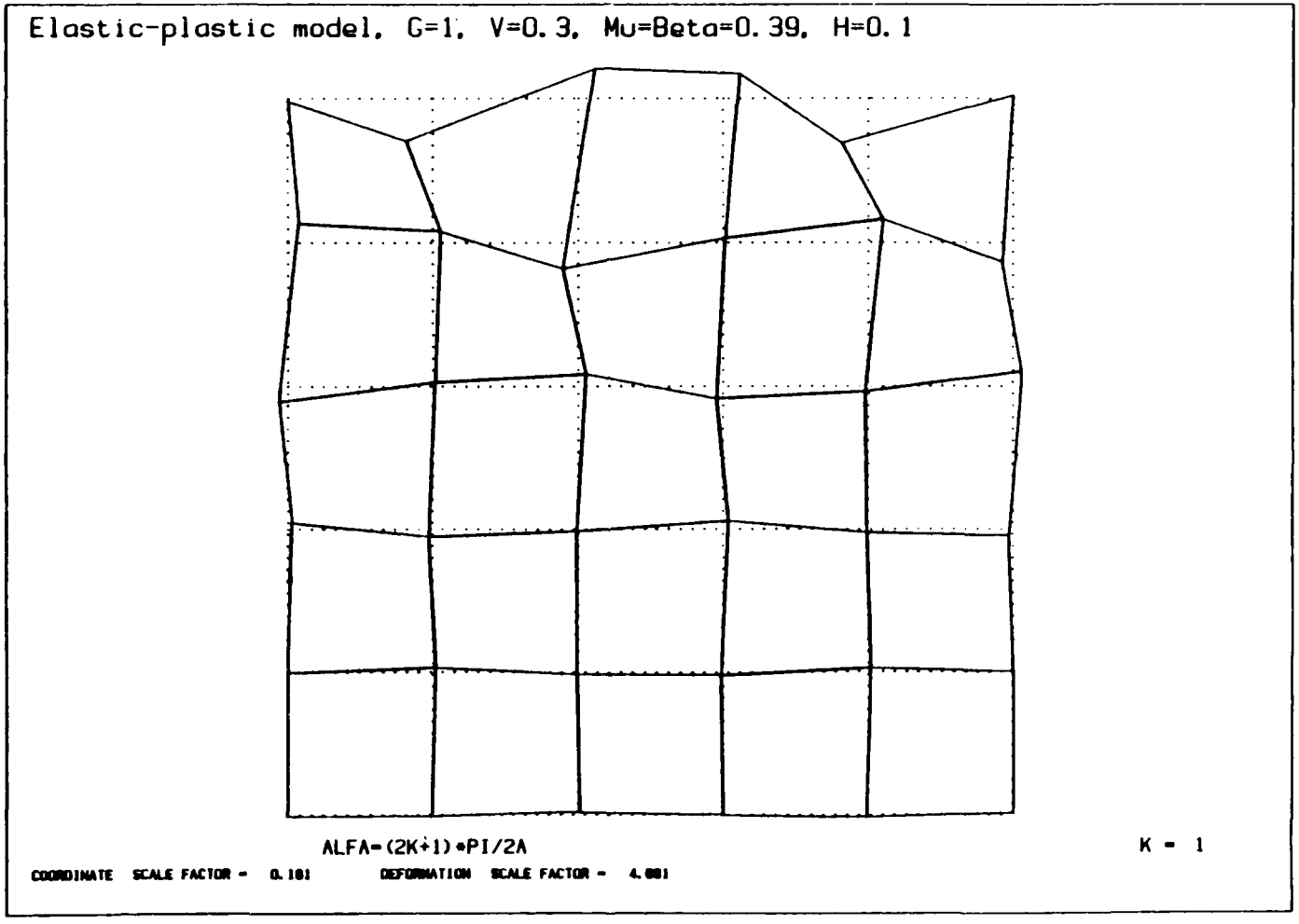

Figure 17b. Second eigenmode of the half space for elastoplastic model($\mu=\beta=0.39$, $H/G=0.1$).

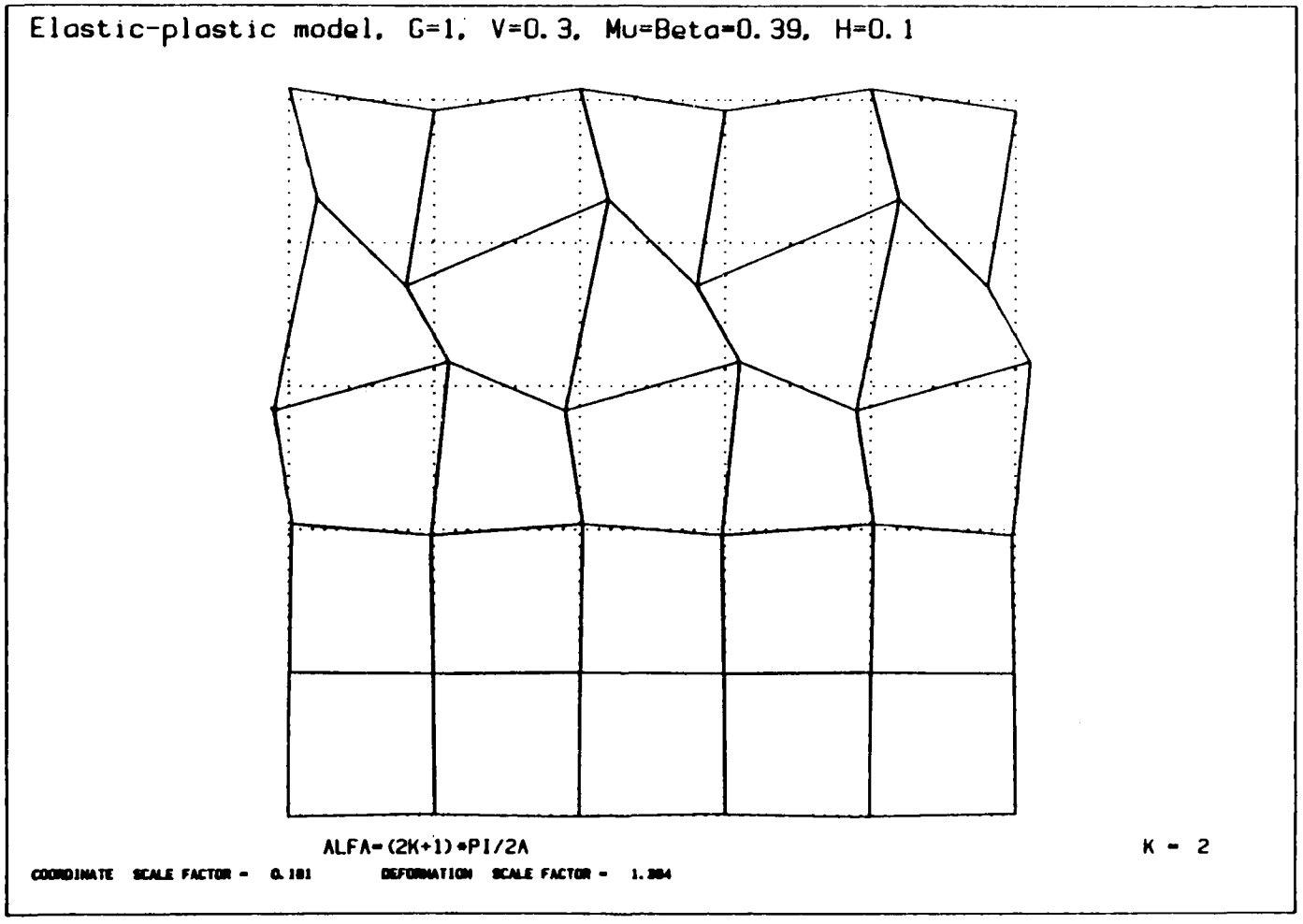

Figure 17c. Third eigenmode of the half space for elastoplastic model ($\mu=\beta=0.39$, $H/G=0.1$).

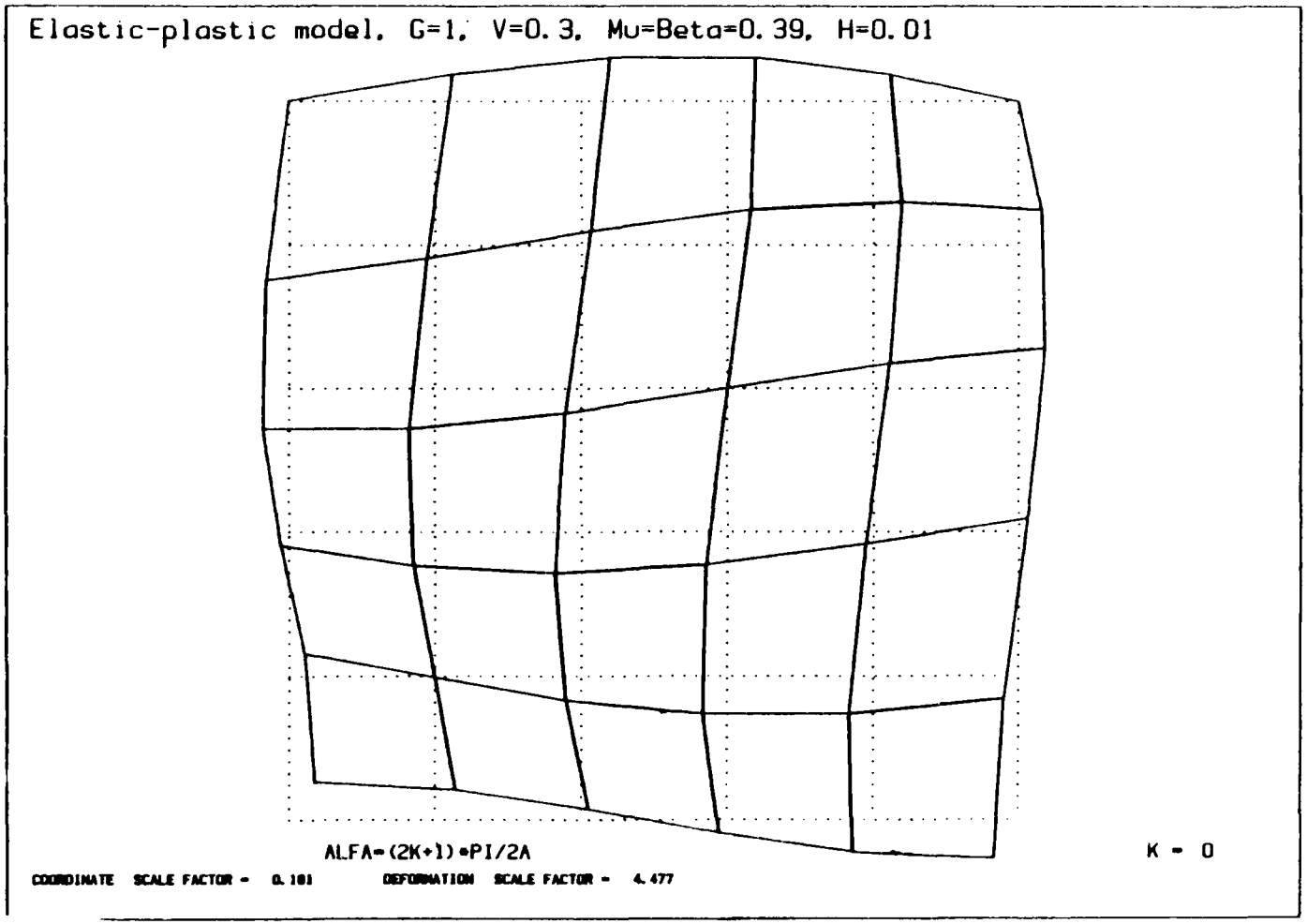

Figure 18a. First eigenmode of the half space for elastoplastic model ($\mu=\beta=0.39$, $H/G=0.01$).

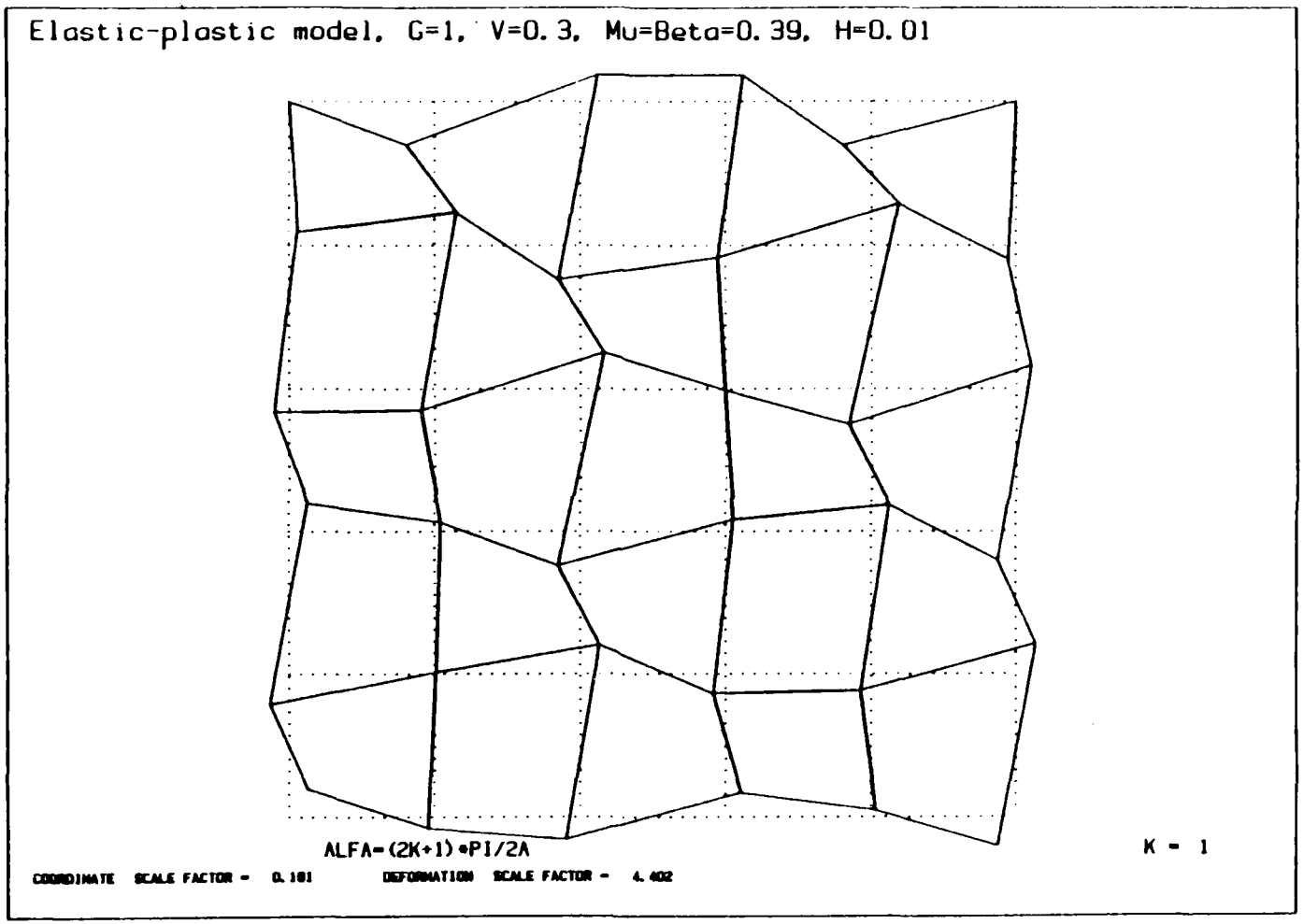

Figure 18b. Second eigenmode of the half space for elastoplastic model ($\mu=\beta=0.39$, $H/G=0.1$).

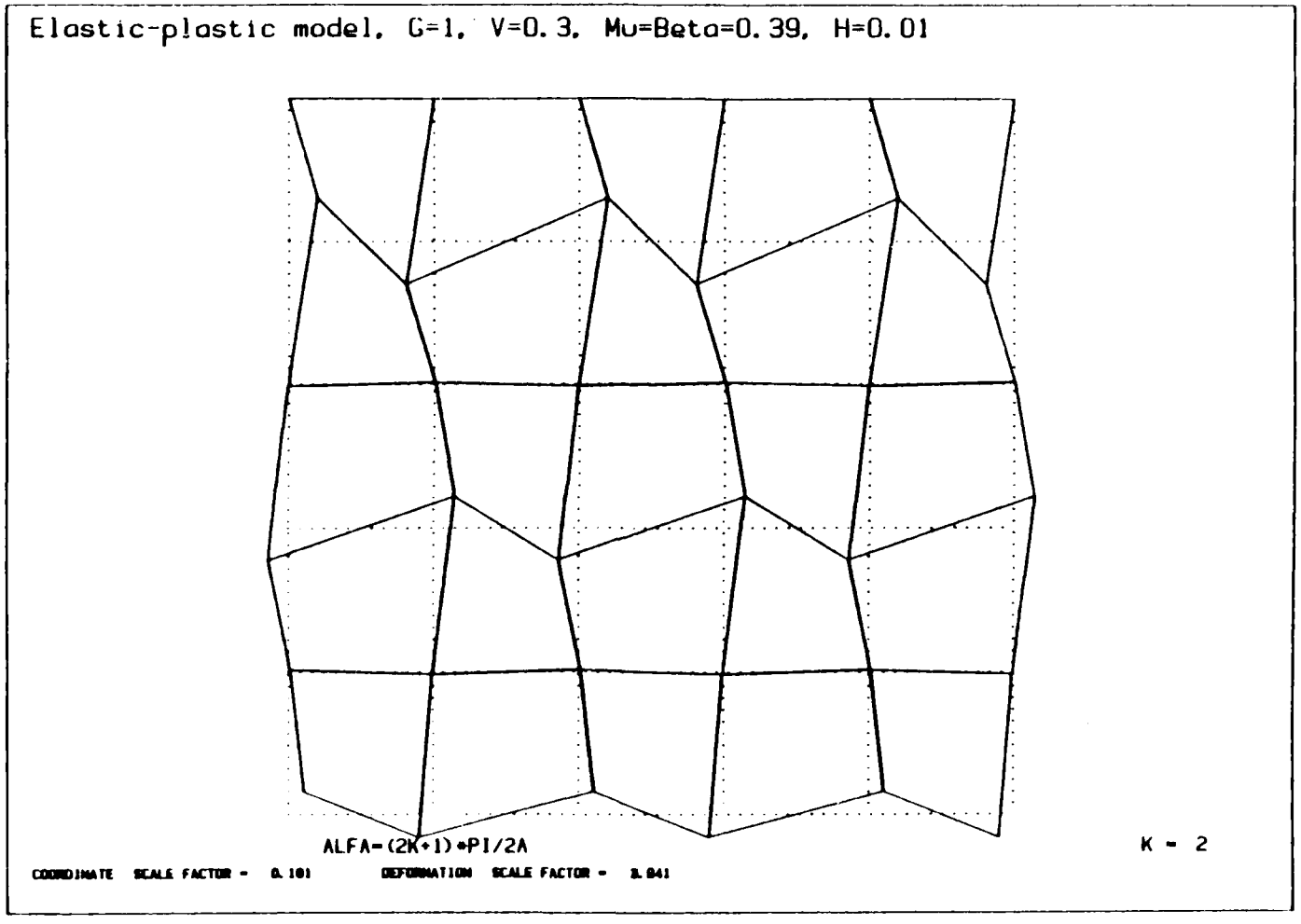

Figure 18c. Third eigenmode of the half space for elastoplastic model ($\mu=\beta=0.39$, $H/G=0.1$).

AD-A192 145 NUMERICAL ASSESSMENT OF ROCKBURSTING(U) AGBABIAN ASSOCIATES EL SEGUNDO CA J P BARDET 27 MAY 87 R-8618-6171 DNA-TR-87-158 DNA001-86-C-0059 2/2

UNCLASSIFIED F/G 8/9 NL

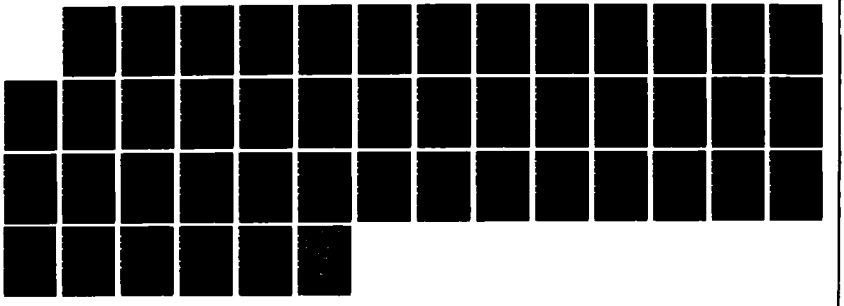

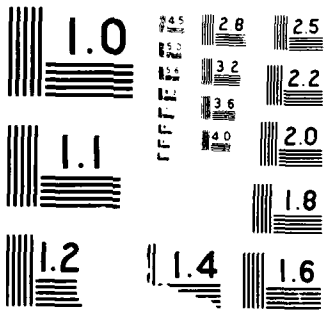
1.0
1.1
1.2
1.4
1.6
1.8
2.0
2.2
2.5
2.8
3.2
3.6
4.0
4.5

The influence of non-associative flow rule has also been investigated in Figs.19, by setting the dilatancy parameter β equal to zero. In this case, surface instability is found to be only possible when the normalized plastic modulus H/G is larger than about 0.055. For value smaller than 0.055 the roots Z_1 and Z_2 of equation (20) are pure imaginary, which implies that the amplitude of the velocity field does not decay with depth. The eigenmodes corresponding to H/G=0.05 are plotted in Figs.19. These eigenmodes, which show no sign of amplitude decay with depth, are incompatible with the boundary condition of the wedge test and of the half-space. From the results of Fig.16, it may be concluded that surface instability will be only possible when stresses reach a value in the order of the elastic shear modulus, which is unlikely to take place due to plastic yielding. This resistance to surface buckling which was encountered during the finite element analysis of elastoplastic material subjected to the wedge test was therefore to be expected. These observations are in agreement with the results of Hutchinson and Tvergaard (1980) but in disagreement with the results of Horii and Nemat-Nasser(1982). The origins of such a disagreement need to be investigated in more detail in future research.

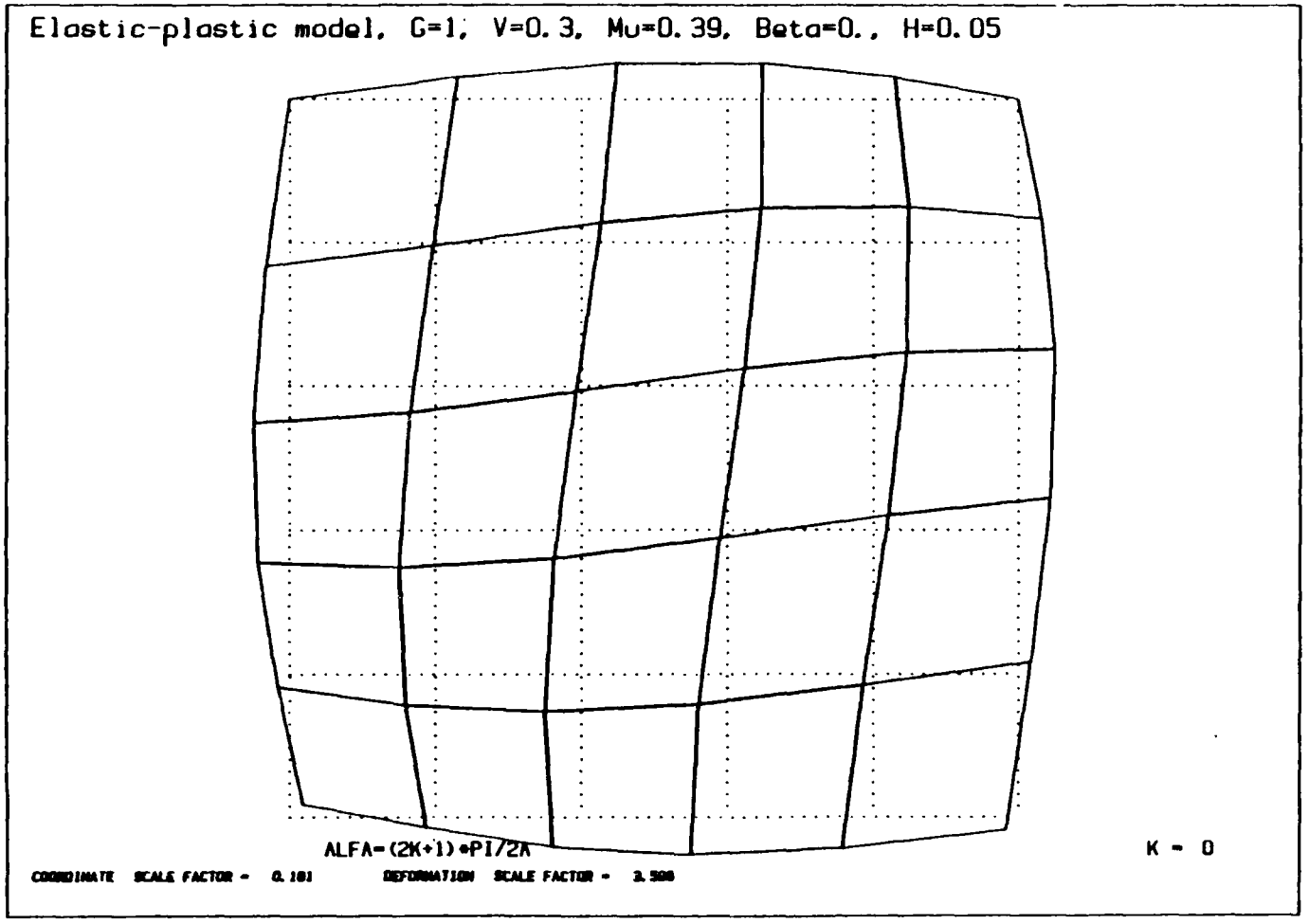

Figure 19a. First eigenmode of the half space for elastoplastic model (μ=0.39, β=0., H/G-0.05).

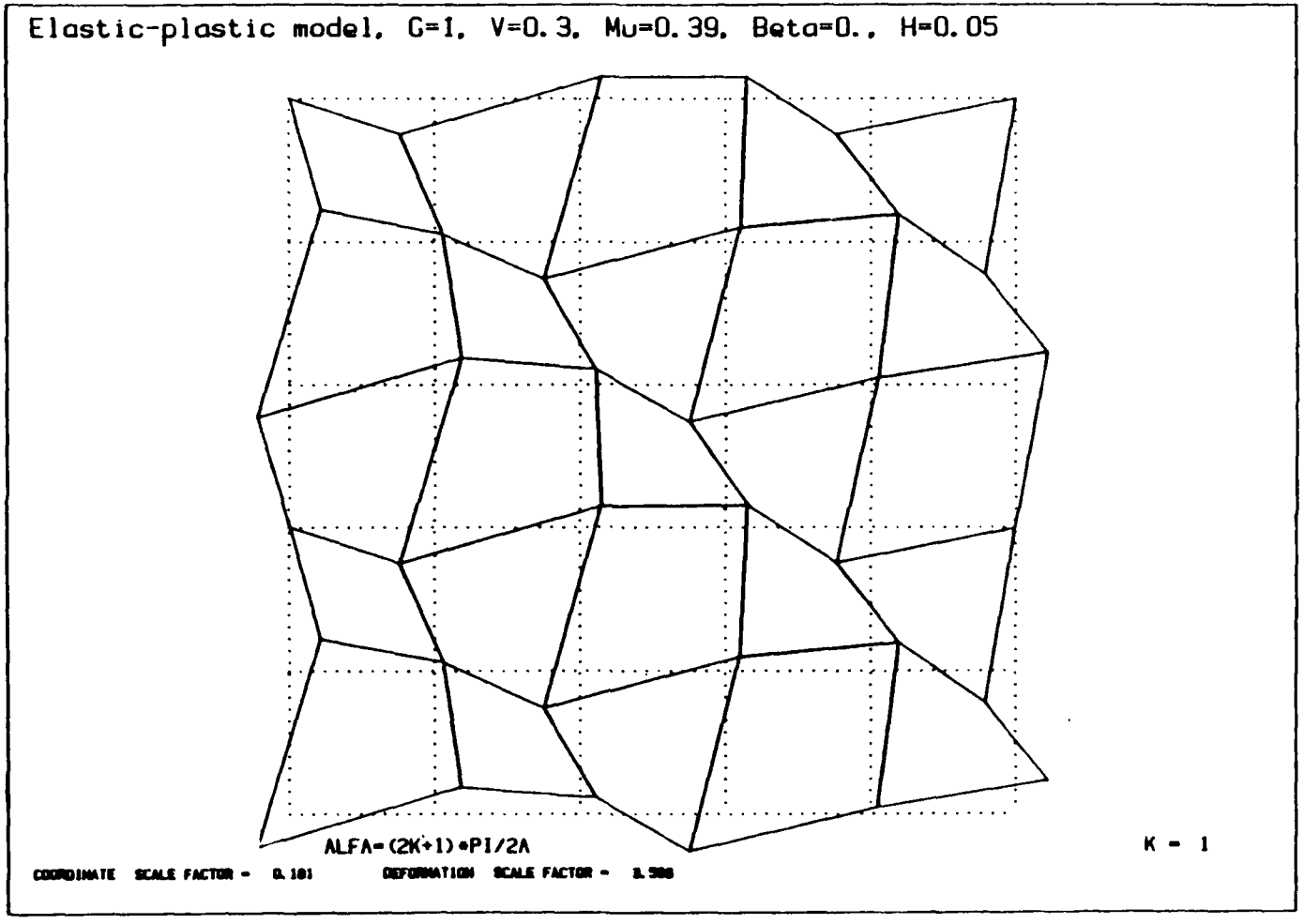

Figure 19b. Second eigenmode of the half space for elastoplastic model (μ=0.39, β=0., H/G=0.05).

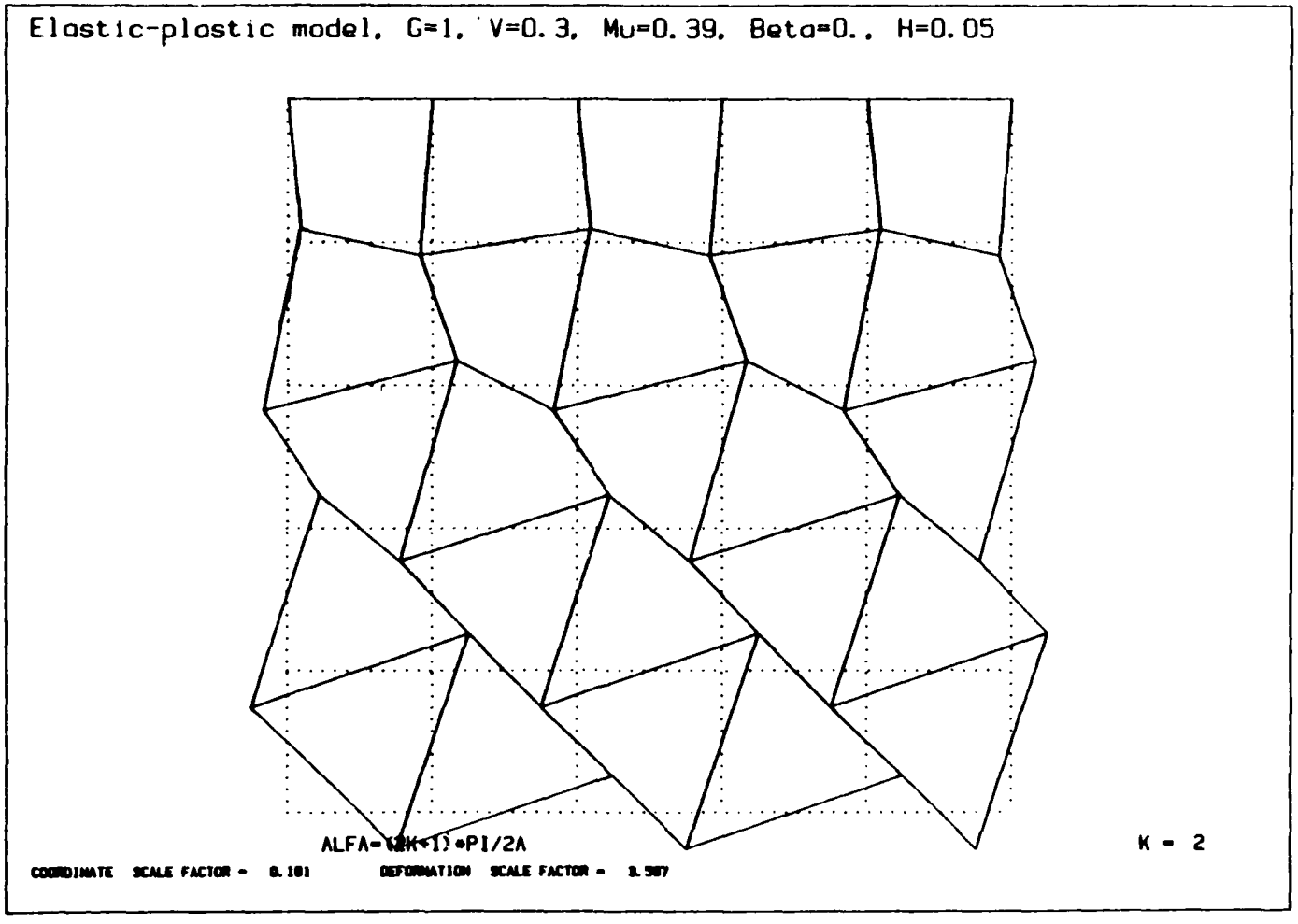

Figure 19c. Third eigenmode of the half space for elastoplastic model (μ=0.39, β=0., H/G=0.05).

Table 6. Velocity field at the inception of surface instability

$$v_1 = (e^{-\alpha Z_1 y} + C_1 e^{-\alpha Z_2 y}) . e^{i\alpha x}$$

$$v_2 = (C_2 e^{-\alpha Z_1 y} + C_3 e^{-\alpha Z_2 y}) . e^{i\alpha x}$$

No.	σ_{11}/G	Z_1	Z_2	C_1	C_2	C_3
1	-1.44832	(1.,0.)	(0.476,0.)	(-0.580,0.)	(0.,1.)	(0.,-1.724)
2	-0.19823	(3.80,0.)	(0.018,0.)	(-0.0326,0.)	(0.,0.128)	(0.,-3.926)
3	-0.47157	(0.29,1.27)	(0.29,-1.27)	(-0.071,0.997)	(1.658,0.118)	(0.,-1.662)
4	-0.07942	(0.05,1.49)	(0.05,-1.49)	(-0.007,0.999)	(1.555,0.011)	(0.,-1.555)
5	-0.30146	(0.,1.1146)	(0.,1.11598)	(-0.996,0.)	(1.0347,0.)	(-1.030,0.)

where

No.1 - Isotropic hypo-elastic (Figs.13a to 13c)

$G = 1$, $G_t = 1$, $\nu = 0.3$

No.2 - Anisotropic hypo-elastic (Figs.15a to 15c)

$G = 1$, $G_t = 0.1$, $\nu = 0.3$

No.3 - Elastoplastic model (Figs.17a to 17c)

$G = 1$, $\nu = 0.3$, $\mu = \beta = 0.39$, $H = 0.1$

No.4 - Elastoplastic model (Figs.18a to 18c)

$G = 1$, $\nu = 0.3$, $\mu = \beta = 0.39$, $H = 0.01$

No.5 - Elastoplastic model (Figs.19a to 19c)

$G = 1$, $\nu = 0.3$, $\mu = 0.39$, $\beta = 0.$, $H = 0.05$

SECTION 5

INFLUENCE OF NONUNIFORM STRESS FIELD ON SURFACE INSTABILITY

The fourth task of the project was to examine the effect of nonuniform stress distribution on the value of the buckling load. This influence has been investigated by restraining the vertical displacement of the nodes located on the left boundary of Fig.2. The nodal displacement are prescribed in both horizontal and vertical direction. This prescribed displacement boundary condition corresponds to the case of no slippage between the material and the left loading plate. Besides the vertical displacement conditions on the left boundary, the geometry and boundary conditions of the model are similar to the ones shown in Fig.2. The deformed mesh at the onset of surface instability is shown in Fig.20. As shown in Fig.21, the stress-displacement response is almost identical to the frictionless case; however the introduction of friction tends to make the material response slightly stiffer than in the absence of friction. Figs.22a, b, and c represent the contour of the various components of stress σ_{11}, σ_{33}, and σ_{12} which characterize the degree of nonuniformity of the stress field. The horizontal stress σ_{11} varies between -0.270 and -0.241, the stress σ_{33} between -0.058 and +0.0036, and the shear stress σ_{12} between -0.00182 and 0.00629. All stresses can be considered dimensionless since the shear modulus G has been selected equal to 1. The detection of the bifurcation can be performed in the same way as in the absence of friction. The variation of the minimum eigenvalues of the stiffness matrix versus the applied displacement u_1 is shown in Fig.23. This figure also indicates that the minimum eigenvalue of the tangential stiffness matrix with friction is always larger that the one

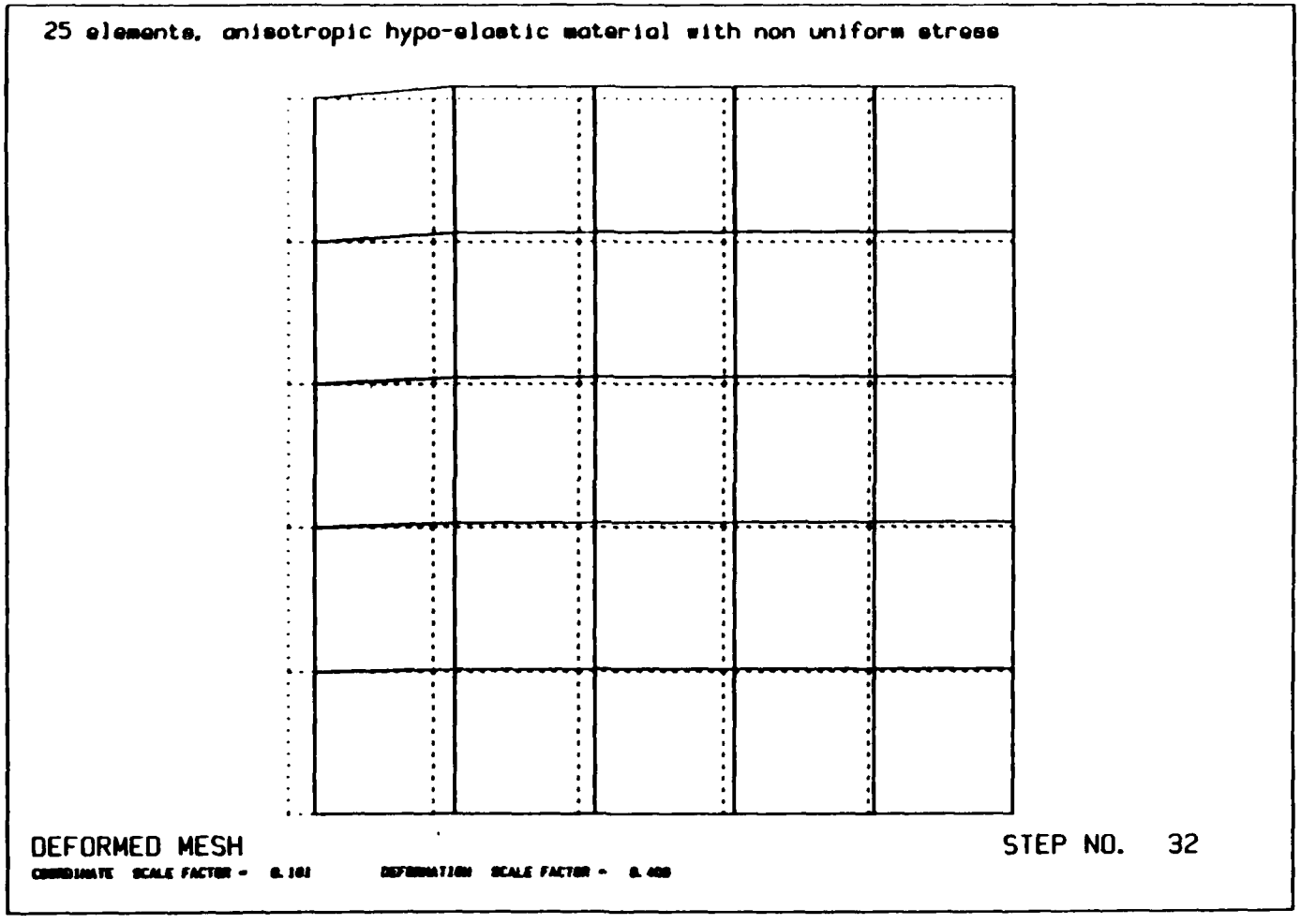

Figure 20. Deformed mesh at the onset of surface instability of anisotropic hypo-plastic material in presence of friction on the left boundary.

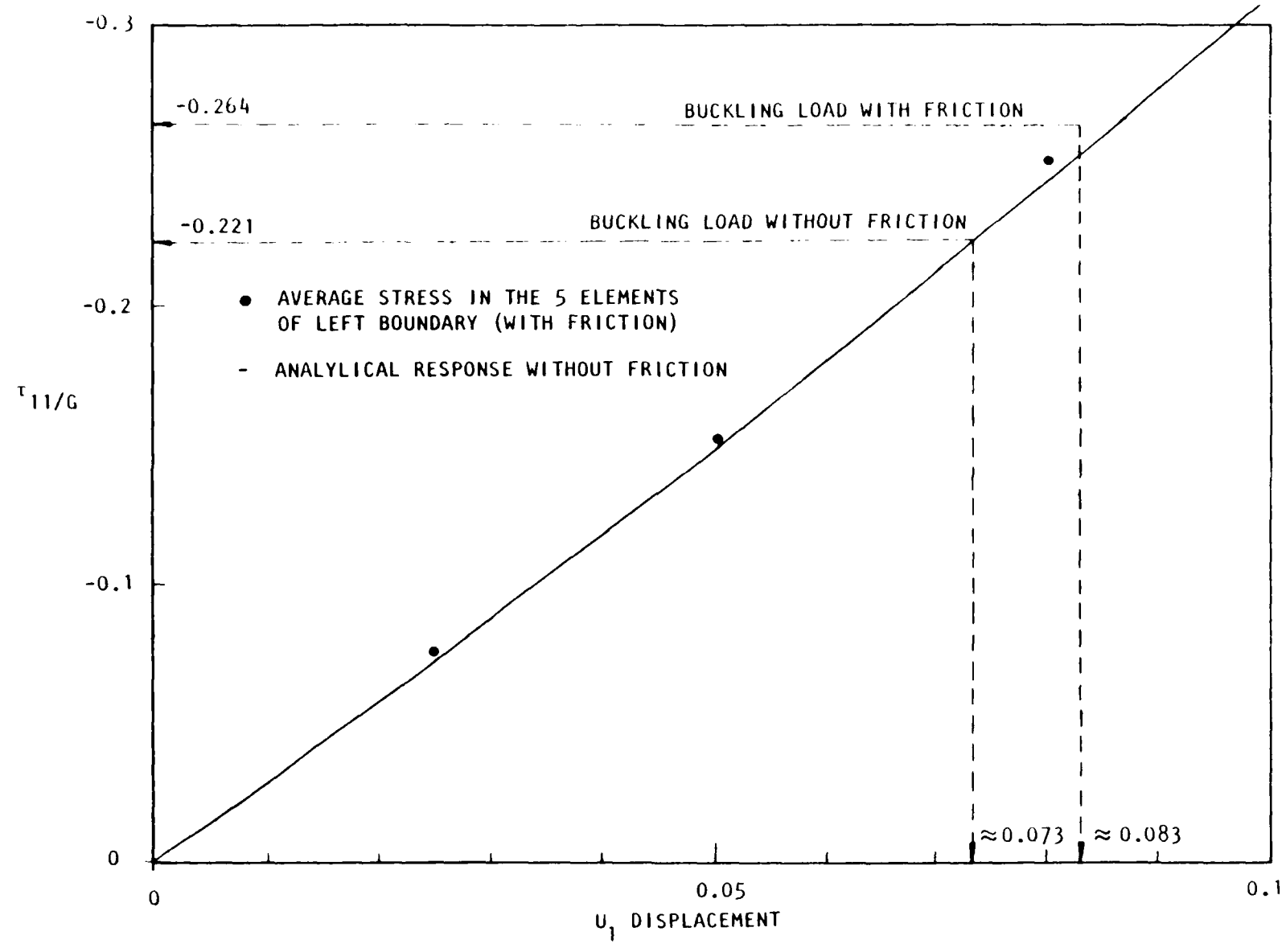

Figure 21. Stress-displacement responses with and without friction for anisotropic hypo-elastic material.

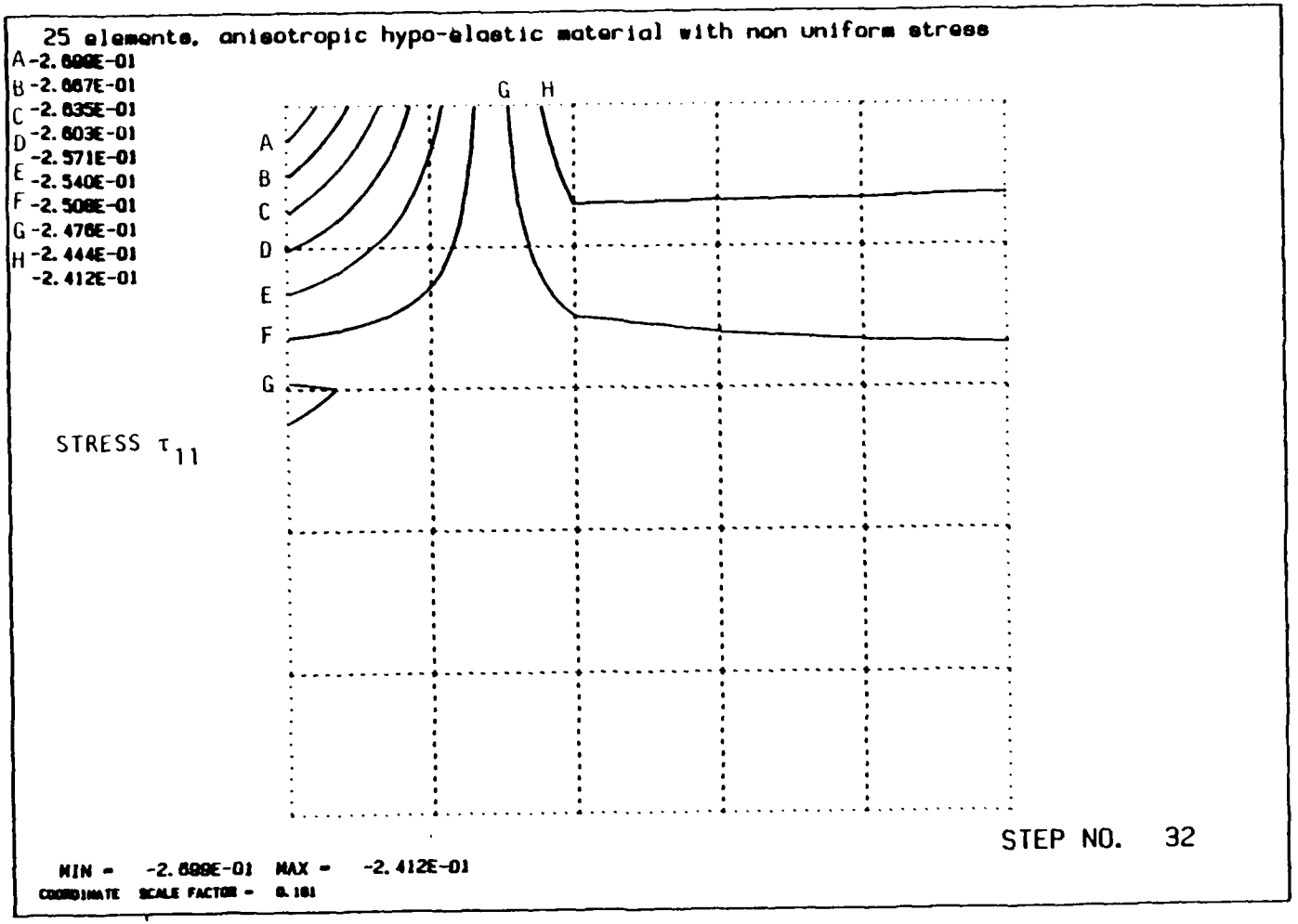

Figure 22a. Contours of stress, τ_{11}, in presence of friction for anisotropic hypo-elastic material.

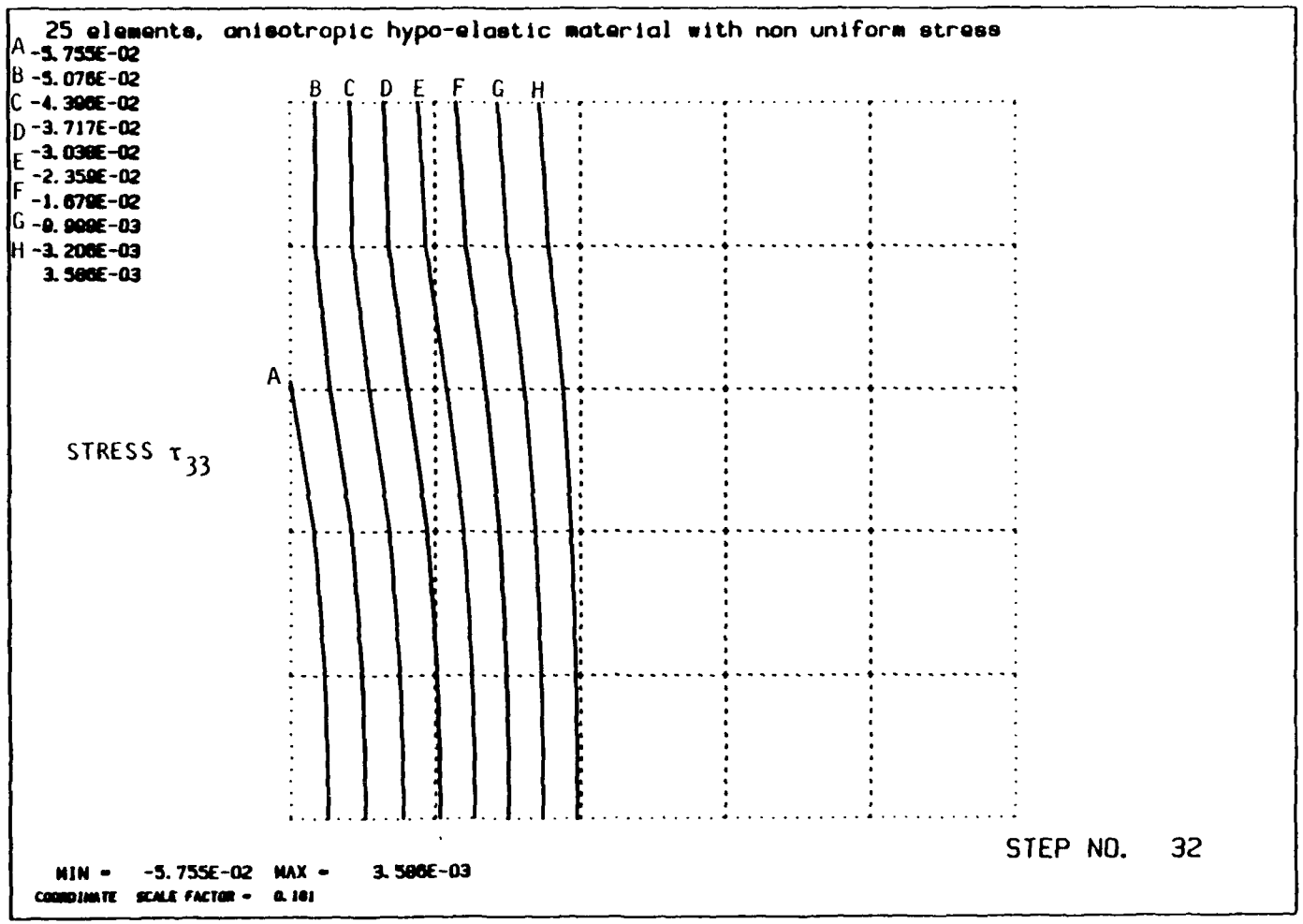

Figure 22b. Contours of stress, τ_{33}, in presence of friction for anisotropic hypo-elastic material.

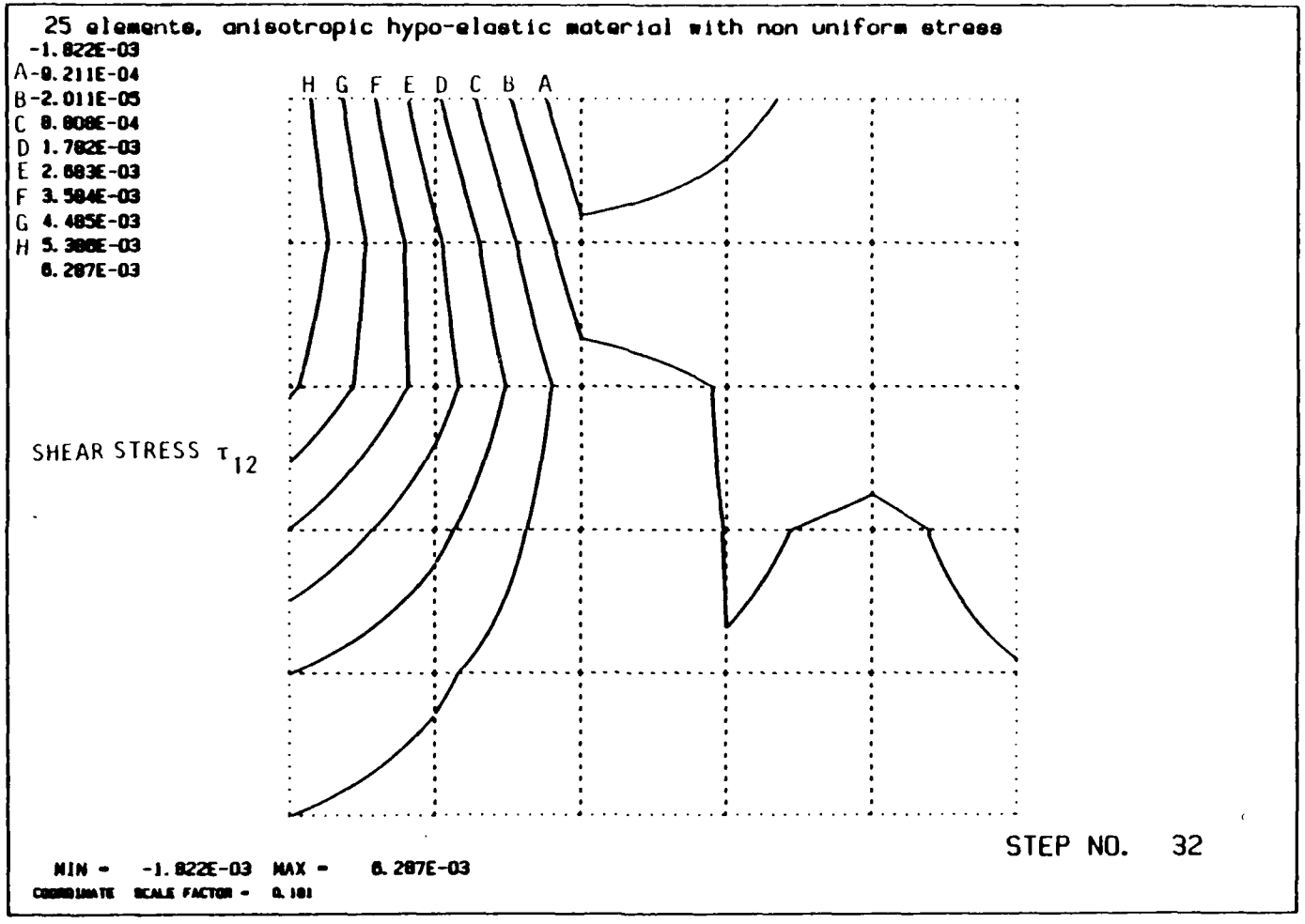

Figure 22c. Contours of stress, τ_{12}, in presence of friction for anisotropic hypo-elastic material.

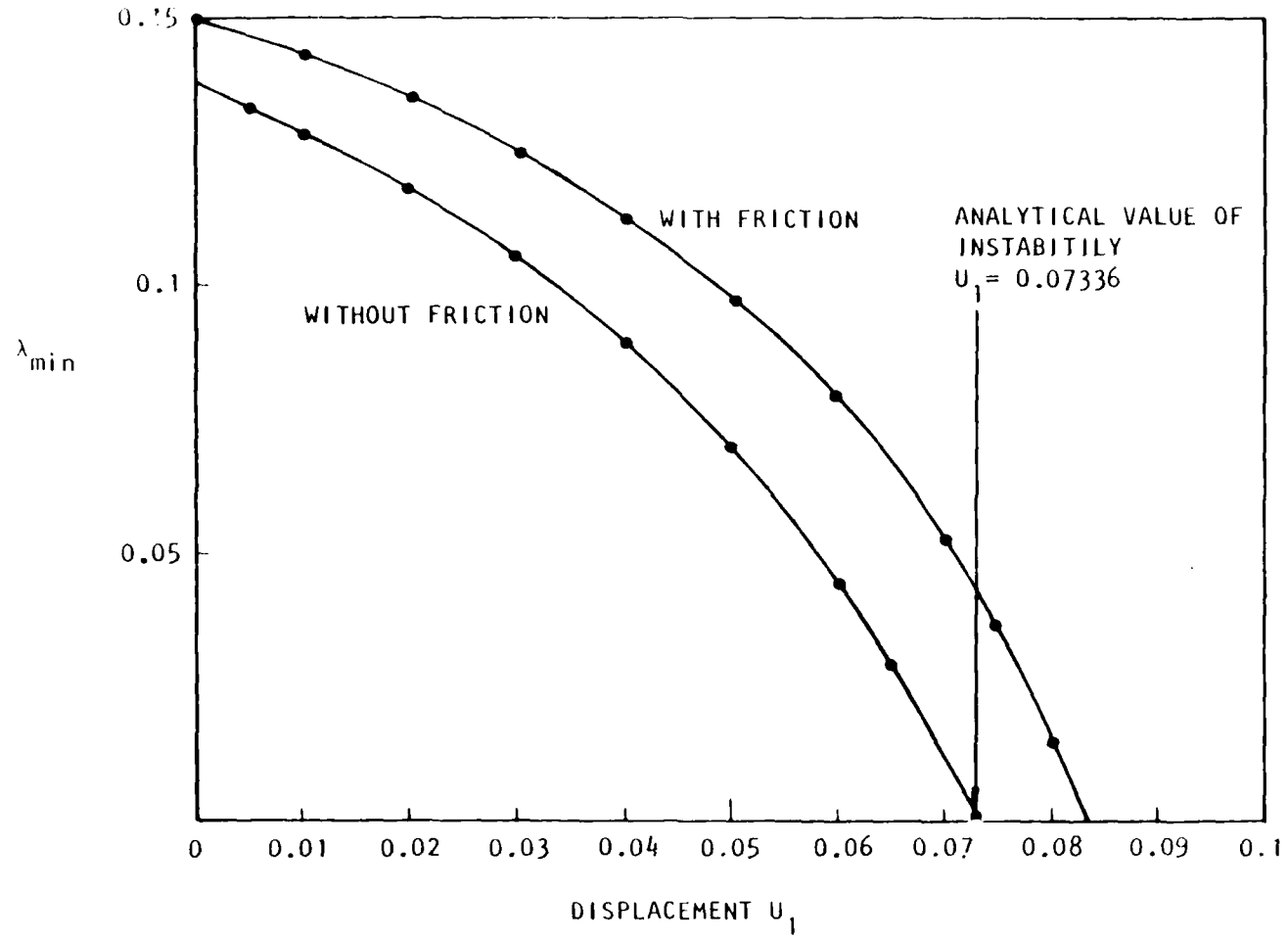

Figure 23. Minimum eigenvalue λ_{min} of the stiffness matrix in presence of friction for a 25 elements model of anisotropic hypo-elastic material.

without friction. Therefore introducing friction on the boundary increases the buckling load. The eigenvectors associated with the eigenvalues of Table 7 are shown in Figs.24a to 24i. The eigenmodes are similar to the ones obtained in the absence of friction, with the difference that the amplitude on the left boundary are zero. The mode associated with the lowest eigenvalue is quite similar to the second mode which was obtained for the frictionless conditions of Figs.9. The similitude pertains for the surface modes of Figs. 24b to 24e and for the edge modes of Figs. 24f to 24h. Two edge modes of Figs.9 are missing due to the kinematic constraints imposed at the left boundary of Fig.2. The buckling load increases as friction is introduced since the kinematic constraints prevent the buckling modes from being activated.

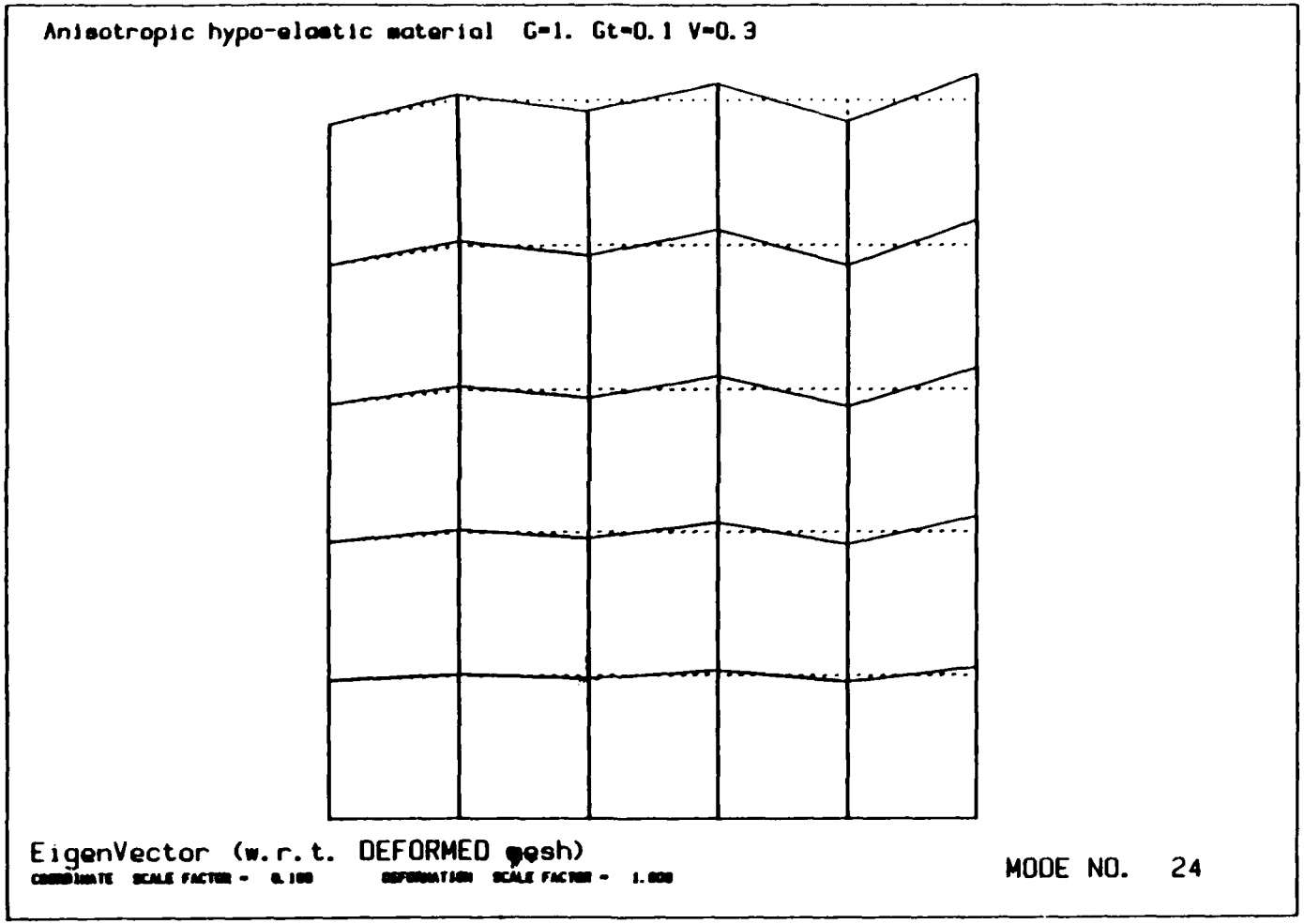

Figure 24a. First eigenmode with friction for a 25 elements model of anisotropic hypo-elastic material.

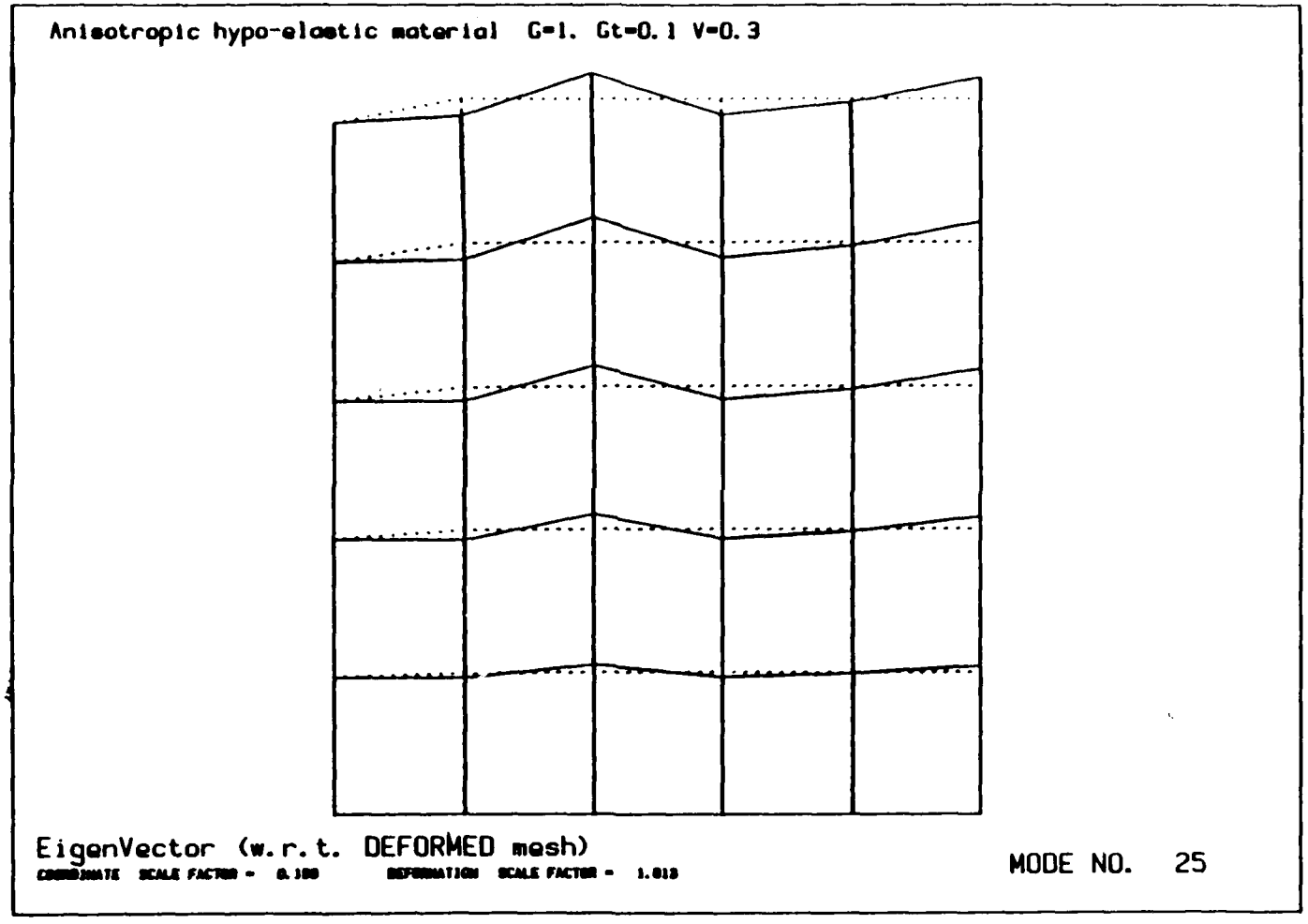

Figure 24b. Second eigenmode with friction for a 25 elements model of anisotropic hypo-elastic material.

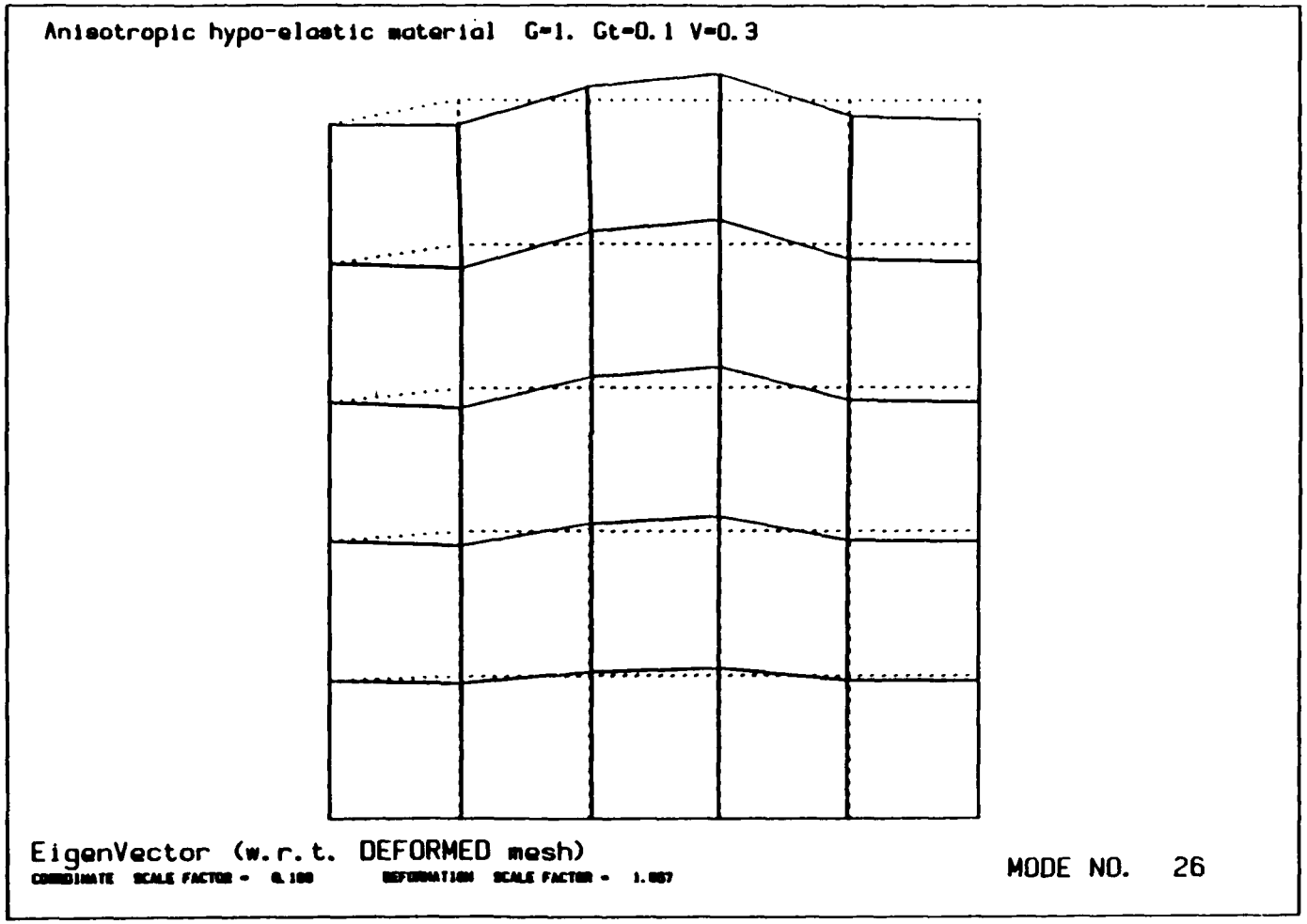

Figure 24c. Third eigenmode with friction for a 25 elements model of anisotropic hypo-elastic material.

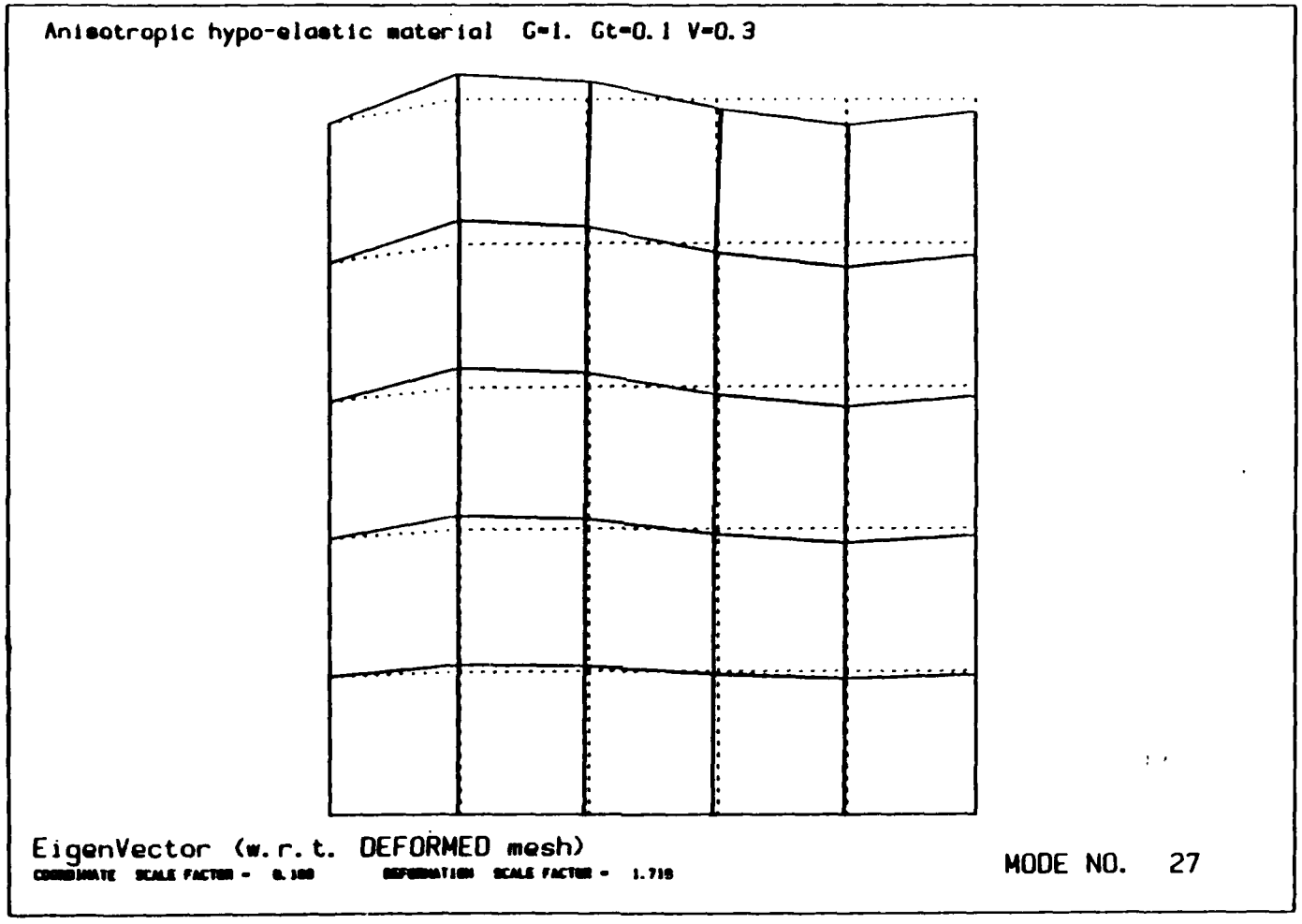

Figure 24d. Fourth eigenmode with friction for a 25 elements model of anisotropic hypo-elastic material.

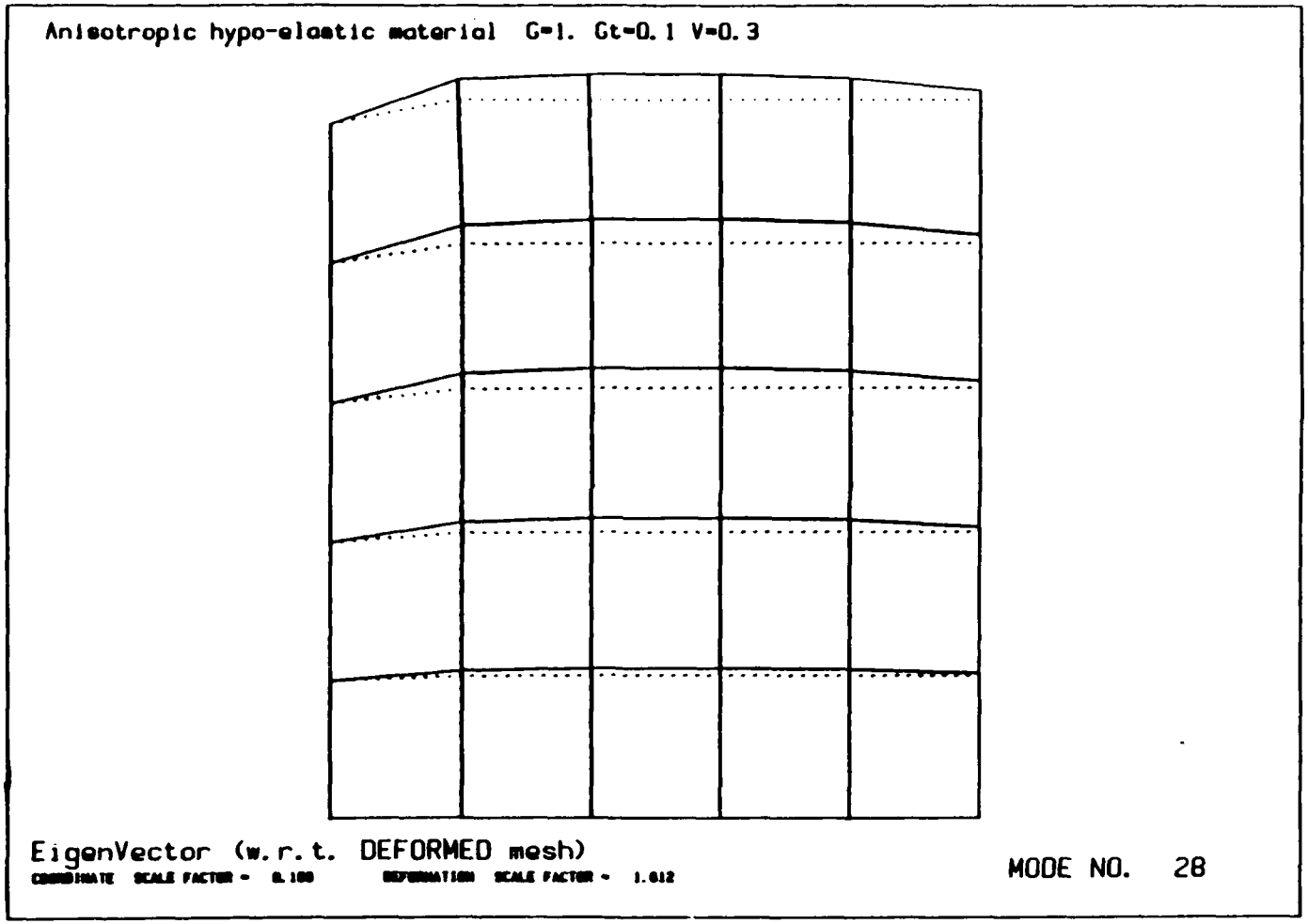

Figure 24e. Fifth eigenmode with friction for a 25 elements model of anisotropic hypo-elastic material.

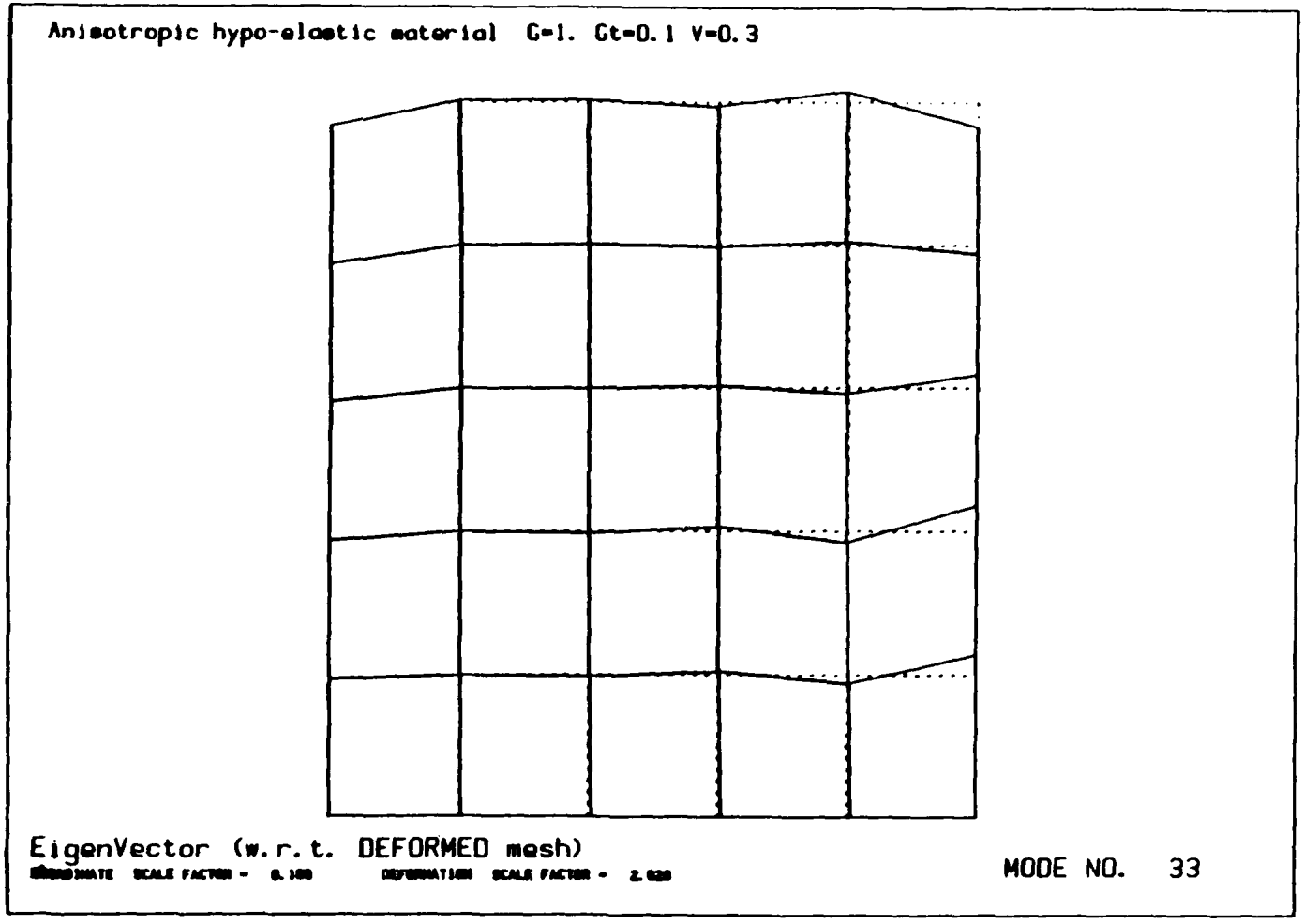

Figure 24f. Sixth eigenmode with friction for a 25 elements model of anisotropic hypo-elastic material.

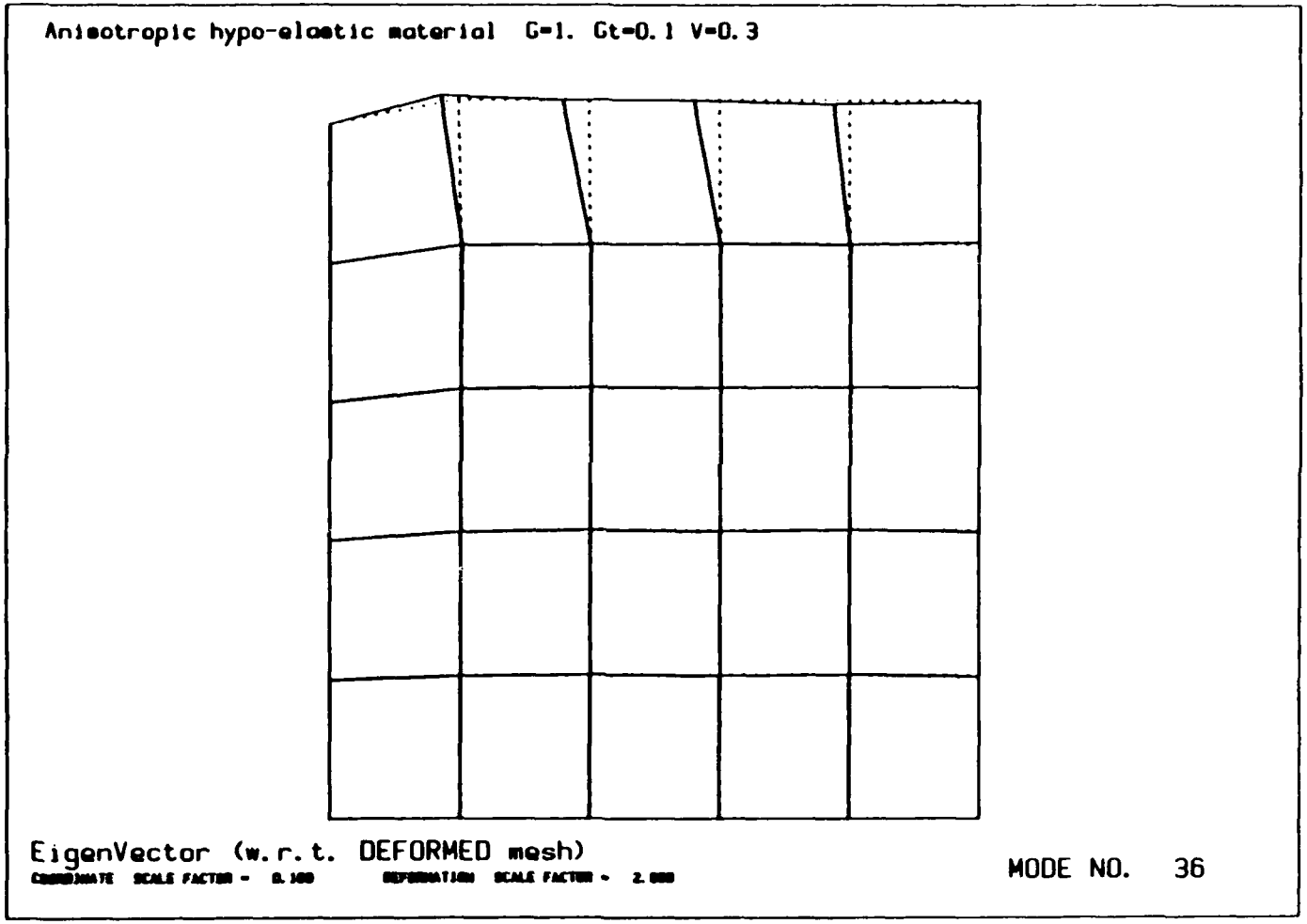

Figure 24g. Seventh eigenmode with friction for a 25 elements model of anisotropic hypo-elastic material.

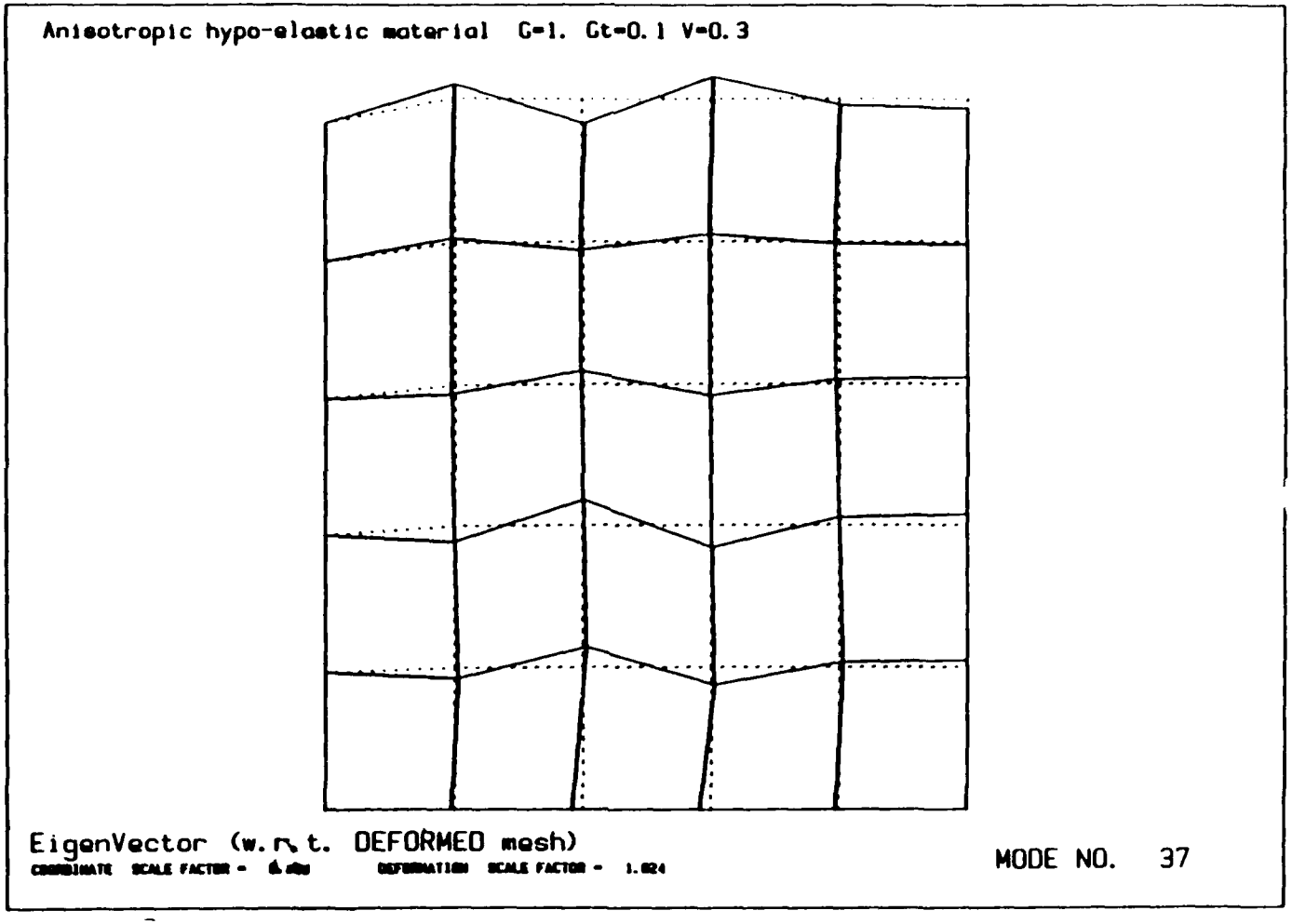

Figure 24h. Ninth eigenmode with friction for a 25 elements model of anisotropic hypo-elastic material.

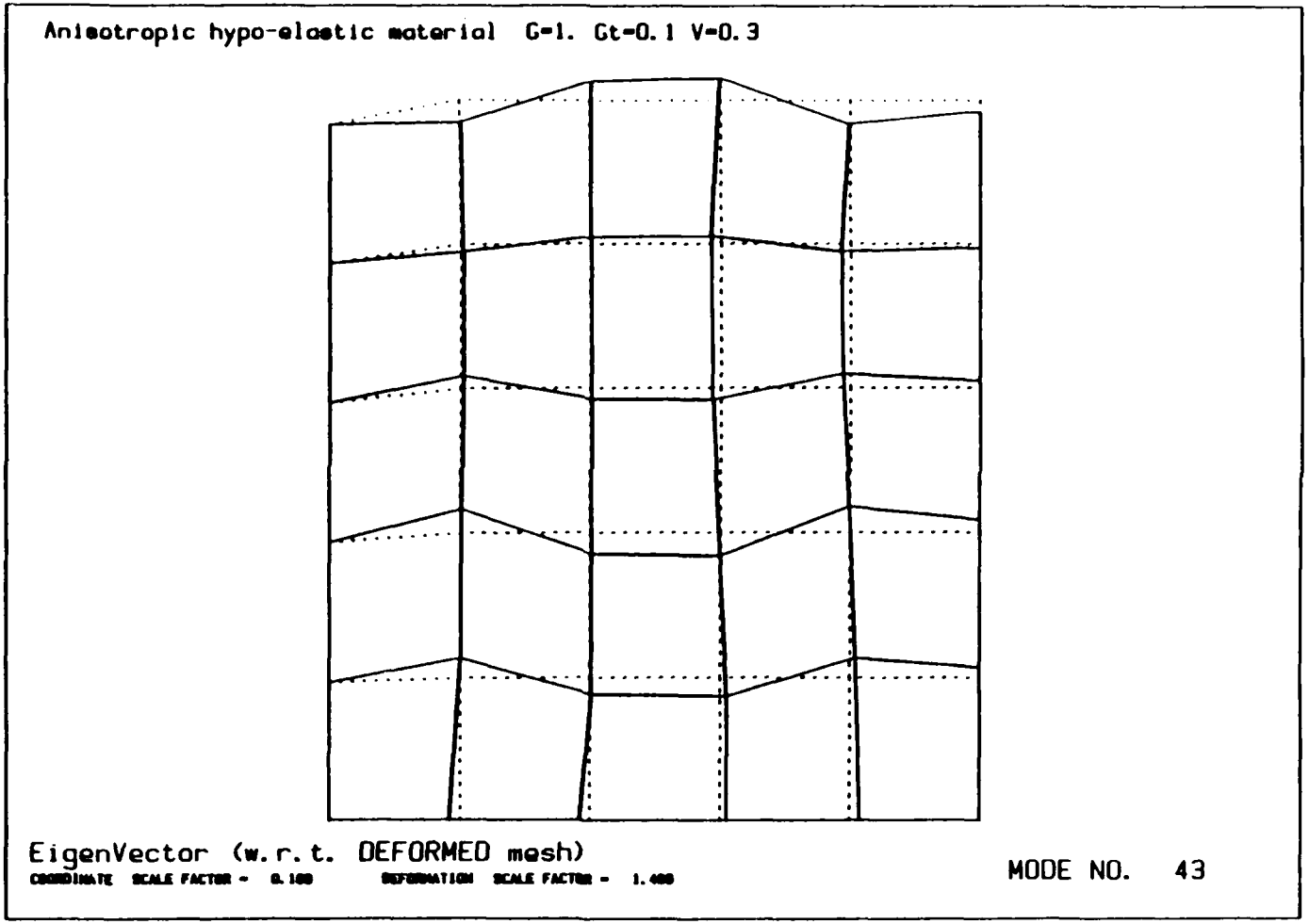

Figure 24i. Tenth eigenmode with friction for a 25 elements model of anisotropic hypo-elastic material.

Table 7. Eigenvalues of the stiffness matrix at the onset of surface instability for a 25 elements model of anisotropic hypo-elastic material in presence of friction.

Mode No	Eigenvalue	Type	Mode No	Eigenvalue
1	0.01455	surface	26	3.008
2	0.04254		27	3.390
3	0.08934		28	3.878
4	0.1359		29	3.958
5	0.2274		30	4.415
6	0.4679	edge	31	4.815
7	0.6216		32	4.872
8	0.6433	volume	33	4.872
9	0.7814		34	5.203
10	1.030		35	5.465
11	1.039		36	5.715
12	1.171		37	5.746
13	1.268		38	6.923
14	1.305		39	7.100
15	1.574		40	7.153
16	1.584		41	7.546
17	1.672		42	8.392
18	1.959		43	9.170
19	2.013		44	9.239
20	2.088		45	9.760
21	2.168		46	10.54
22	2.449		47	10.84
23	2.682		48	12.49
24	2.768		49	14.19
25	2.798			

SECTION 6

CONCLUSIONS AND RECOMMENDATIONS

6.1 CONCLUSIONS.

A general numerical approach has been developed to assess the phenomenon of rockbursting, based upon the assumption that rockbursting is a surface instability of bulky material masses. The general approach has been calibrated in the case of a simple boundary value problem: the wedge test.

The analysis has been carried out in four steps:

1. Using nonlinear finite element methods similar to the ones employed in structural dynamics, finite element computer program modules have been developed for analyzing surface instability of material masses.
2. The modules have been used to analyze a simple boundary value problem: the wedge test. The numerical solutions have been compared with analytical solutions in the case of isotropic and anisotropic hypo-elastic materials.
3. Three constitutive equations formulated in terms of large deformation have been used to describe the material behavior: isotropic and anisotropic hypo-elastic, and elastoplastic models. The influence of their respective material constants on the surface instability during the wedge test has been evaluated.
4. The influence of the friction on surface instability has also been estimated in the case of the wedge test.

Surface instability has been treated as a bifurcation phenomenon, which emerges from the loss of uniqueness of the

partial differential equation of incremental stress equilibrium. In the context of finite elements, the bifurcation point is detected when the tangential stiffness matrix becomes singular. Accurate finite element methods have been required in order to detect the bifurcation and to avoid numerical divergence. In the vicinity of a bifurcation point, finite element methods have been found to consider the computational errors, which are inherent due to any iterative techniques, as a geometrical imperfection of the finite element mesh. In some circumstances, these artificial imperfections were found to grow rapidly and to transform the uniform stress-strain state into highly heterogeneous stress and strain field leading to numerical divergence. These artificial geometrical imperfections have the same effect as the eccentricity in the buckling problem of Euler beams. From another point of view, these artificial imperfections render difficult the approach of bifurcation point by transporting the numerical solution on a bifurcated branch of solution far away from the analytical bifurcation point.

Isotropic and anisotropic hypo-elastic models were found to be simple to use in estimating the buckling load and eigenmode of the wedge test. For such hypo-elastic materials, numerical and analytical solutions were in excellent agreement, which demonstrated that our numerical methods and implementation were appropriate to describe surface instability. The elastoplastic models of the flow theory of plasticity which are used in this analysis are found to be resistant to surface instability during the finite element analysis of the wedge test. A more detailed analytical investigation corroborated these finite element observations. This analysis revealed that a slice of the half space made of the same elastoplastic models is prone to volume instability for low stress level and to surface instability for high stress level. In other words, this analysis pointed out that

surface instability may be impossible for some combinations of material parameters or loading conditions since plastic yielding prevents stress from reaching values of the same order as elastic shear modulus. These observations on the influence of material modeling on surface instability are in agreement with Hutchinson and Tvergaard conclusions (1980) but in disagreement with Nemat-Nasser and Horii results (1982).

6.2 RECOMMENDATIONS.

In order to clarify the problems encountered in the wedge test of elastoplastic model, it is recommended to extend the methods used in the program BIF from the half-space to block of finite length. This extension will provide a valuable approach for the investigation of surface instability in the case of block of finite size made of elastoplastic material.

The numerical methods which have been developed in this work have only been applied to the simple boundary value problem of the wedge test. According to the good agreement between numerical and analytical results in the case of the wedge test, it is recommended to extend the method to the more complex boundary problems encountered in real excavations. A direct application of this generalization is to estimate the risk of rockbursting of real excavations.

The present work analyzed only the emergence of surface instability but did not examine how the phenomenon evolve afterwards. In order to extend the solution in the post-bifurcation range, it is recommended to use the computational techniques of structural mechanics known as continuation techniques or imperfection approach.

Finally it is suggested to perform careful experiments on material prone to surface instability and to develop constitutive models which are more realistic than the ones used in this work. Extreme care must be exercised in the development of such material models. The anisotropic hypo-elastic model used in this analysis has clearly indicated that surface instability may be dependent on material behavior which are not apparent in the stress-strain response prior to the buckling phenomenon. It is recommended to develop models based upon vertex plasticity or the deformation theory of plasticity.

SECTION 7

LIST OF REFERENCES

1 Avershin, S.G., Mosinets, V.N. and Cherepanov, G.P., (1972) "Nature of a shock bump in mines," Soviet Physics, 17:5.

2 Bathe, K.G., (1982) "Finite Element Procedures in Engineering Analysis," Prentice-Hall, New Jersey.

3 Bergan, P.G. and Clough, R.W. (1973) "Larger deflection analyses of plates and shallow shells using the finite element method," Int. Jnl. Num. Methods in Eng., Vol.5, pp 543-556.

4 Biot, M., (1965) "Mechanics of incremental deformations," John Wiley & sons.

5 Budiansky, B., (1959) "A Reassessment of deformation theories of plasticity," Jnl. Appli. Mech., Vol.26, pp 259-264

6 Burgert, W. and Lippmann, H., (1981) "Models of translatory Rock Bursting in Coal," Int. Jnl. Rock Mech. Min. Sci. and Geomechanics, Vol.18, pp 285-294.

7 Chen, W.F., and A.F. Saleeb, (1982) "Constitutive equations for engineering materials," Vol.1, John Wiley & sons.

8 Dorris, J.F., and S. Nemat-Nasser, (1980) "Instability of a Layer on a half space," Journal of Applied Mechanics, Vol.47, pp 304-312.

9 Drescher, A., and I. Vardoulakis, (1982) "Geometric softening in triaxial tests in granular material," Geotechnique, 32, pp 291-303.

10 Freudenthal, A.M., (1977) "Stresses around Spherical and Cylindrical Cavities in Shear Dilatant Elastic Media," 18th U.S. Rock Mech. Symp.

11 Fujikake, M., (1985) "A simple approach to bifurcation and limit point calculations," Int. Jnl. Num. Meths. Engr., Vol.21, pp 183-191

12 Hill, R., and J.W. Hutchinson, (1975), "Bifurcation phenomenon in the plane strain tension test," J. Mech. Phys. Solids, Vol.23, pp 239-264.

13 Horii, H., and S. Nemat-Nasser, (1982) "Instability of a half-space with frictional materials," J. Applied Math. & Phys., Vol.33, pp 1-16.

14 Hughes, T.R.J., and J. Winget, (1981) "Finite roatation effects in numerical integration of rate constitutive equations arising in large deforamtion analysis, Int. Jnl. Num. Meths. Engr.

15 Hutchinson, J.W., and V. Tvergaard, (1980) "Surface instabilities on statically strained plastic solids," Int. J. Mech. Sci., Vol.22, pp 339-354.

16 Ishizahi, T., and Bathe, K.J., (1980) "On finite element large displacement and elastic-plastic dynamic analysis of shell structures," Jnl. Comp. and Struc., Vol.12, pp 309-318.

17 Jaeger, J.C., and Cook, N.G.W. (1977) "Fundamentals of Rock Mechanics," John Wiley, New York.

18 Koiter, W.T., (1945) "On the stability of elastic equilibrium," Delft.

19 Lippmann, H., (1978) "The mechanics of translatory rockbursting," Advances in analysis of geotechnical instabilities, Waterloo, SM study No 13, p 25-63.

20 McMeeking, R.M. and J.R. Rice, (1975) "Finite element formaulation for problems of large elastic-plastic deformation," Int. Jnl. Solids Struc., Vol.11, pp 601-616.

21 Needleman, A., (1979) "Non-normality and bifurcation in plane strain tension and compression," J. Mech. Phys. Solids, Vol.27, pp.231-254.

22 Nemat-Nasser S. and H. Horii, (1979) "Compression-Induced Nonplanar crack extension with Application to Splitting, Exfoliation and Rockburst," Journal of Geophysical Research, Vol. 87, No B8, pp 6805-6821.

23 Nemat-Nasser,S. , and A. Sokooh, (1980) "On finite plastic flows of compressible materials with internal friction," Int. Jnl. Solids Struc., Vol.16, pp 495-514.

24 Ortlepp, W.D., (1978) "The mechanism of a rockburst," Proc. 19th U.S. Symp. on Rock Mech., Reno, NV.

25 Pariseau, W.G., (1979) "A finite element approach to strain softening and size effects in rock mechanics," 3rd Int. Conf. Num. Methods in Geomechanics.

26 Pietruszczak, S. and Z. Mroz, (1980) "Numerical analysis of elastic-plastic compression of pillars accounting for material hardening and softening," Int. Jnl. Rock Mech. Min. Sci. and Geomechanics, Vol.17, pp 199-207.

27 Rudnicki, J.W., and Rice, J.R., (1975) "Conditions for the localization of deformation in pressure sensitive dilatant material," J. Mech. Phys. Solids, Vol.23, pp.371-394.

28 Salomon, M.D.G., (1974) "Rock Mechanics of underground excavations," Proc. 3rd congress of Int. Soc. for Rock Mech., Denver.

29 Smith, B.T., J.M. Boyle, J.J. Dongara, B.S. Garbow, Y. Ikebe, V.C. Klema, and C.B. Moler, (1976) "Matrix Eigensystem Routines- EISPACK Guide," Second edition, Springer-Verlag, Berlin, Heidelberg, New York.

30 Thompson, J.M.T. and A.C. Walker, (1969) "The branching analysis of perfect and imperfect discrete natural systems, "Jnl. Mech. and Phys. Solids, Vol.17.

31 Vardoulakis, I., 1984, "Rockbursting as a surface instability phenomenon," Int. J. Rock. Mech. Min. Sci. & Geomech. Abstr., Vol.21, No.3, pp. 137-144.

32 Vardoulakis, I., and H.B. Muhlaus, "Local Rock Surface instabilities," to appear in Int. J. Rock Mech. Min. Sci. & Geomech. Abstr.

33 Walker, A.C., (1969) "A non-linear finite element analysis of shallow circular arches," Int. Jnl. Solids Struc., Vol.5, pp 97-107.

APPENDIX A

BIOT'S APPROACH TO SURFACE INSTABILITY

The following section presents Biot's approach to investigate the problem of the surface instability of an elastic half-space subjected to finite deformation. It is a simple illustration for the understanding of the phenomenon of surface instability from the point of view of continuum mechanics. The problem was initially formulated by Biot in his book "Mechanics of incremental deformation," John Wiley & Sons, Inc. 1965, page 159. This pioneer work defines the problem of surface instability in a very simple but rigorous way.

Biot describes the material behavior with incompressible finite deformation elasticity:

$$\sigma = \mu_0 G - p.\delta \tag{1a}$$

σ is Cauchy stress, μ_0 the only material constant, p the mean pressure, δ is Kroneker's symbol with components δ_{ij}:

$$\delta_{ij} = 1, \text{ if } i=j; \quad \text{and} \quad \delta_{ij} = 0, \text{ if } i \neq j \tag{1b}$$

G is related to the deformation gradient **F**:

$$\mathbf{G} = \mathbf{F}.\mathbf{F}^{T} \qquad F_{ij} = \frac{\partial x_i}{\partial X_j} \tag{2}$$

where **x** and **X** are the initial and present positions of a particle, respectively. The constitutive equation (1) can be written in incremental form:

$$\hat{\sigma} = \mu_0 \, (\mathbf{D}.\mathbf{G}+\mathbf{G}.\mathbf{D}) - p.\delta \qquad \text{or} \qquad \hat{\sigma}_{ij} = C_{ijkl} \, D_{kl} \tag{3}$$

D is the rate of deformation:

$$D_{ij} = \left(\frac{\partial u_i}{\partial x_j} + \frac{\partial u_j}{\partial x_i} \right)/2 \tag{4}$$

where **u** is the velocity at location **x**

$\hat{\sigma}$, Jauman's rate and, $\overset{\circ}{\sigma}$ material time derivative of Cauchy stress σ are related (see page 32 of Biot's book, 1965)

$$\overset{\circ}{\sigma} = \hat{\sigma} - \sigma.W + \mathbf{W}.\sigma \tag{5a}$$

$$\overset{\circ}{\sigma}_{ij} = \hat{\sigma}_{ij} + \sigma_{ik} \, W_{jk} + \sigma_{jk} \, W_{ik} \tag{5b}$$

W is the spin tensor

$$W_{ij} = \left(\frac{\partial u_i}{\partial x_j} - \frac{\partial u_j}{\partial x_i} \right)/2 \tag{6}$$

The incremental constitutive matrix in the relation (3) is

$$C_{ijkl} = A \, \delta_{ij}\delta_{kl} + (s_{ik}\delta_{lj} + s_{il}\delta_{jk} + s_{jl}\delta_{ik} + s_{jk}\delta_{il})/2 \tag{7}$$

s_{ij} is the deviator stress

$$s_{ij} = \sigma_{ij} - \sigma_{kk}/3\delta_{ij} \tag{8}$$

A is an arbitrary large number, which accounts for incompressibility.
The problem formulated by Biot is shown in Fig.25.

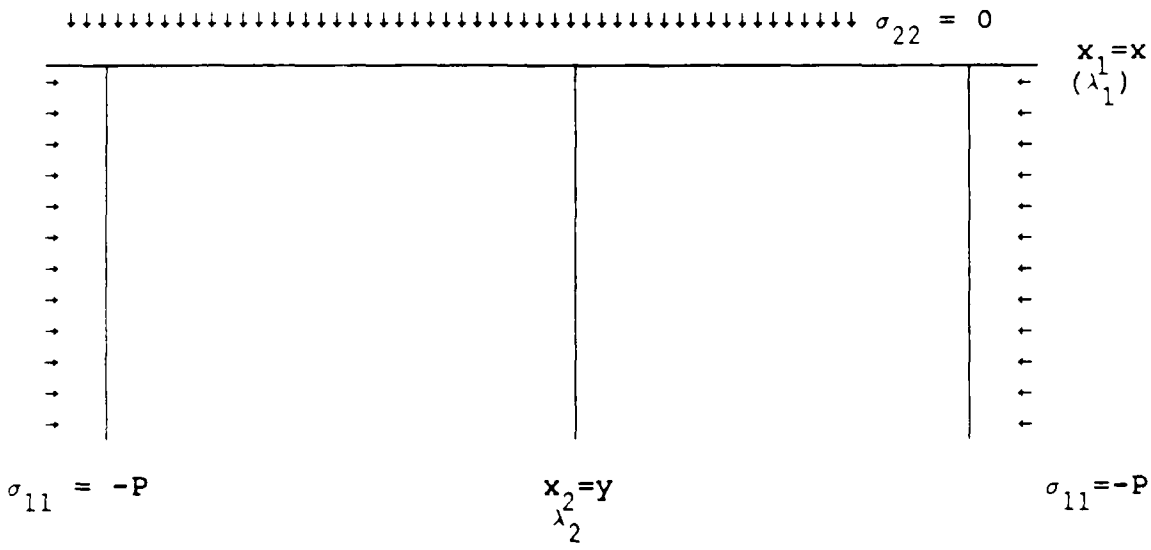

Figure 25. Half-space under compressive stress.

The trivial solution of the problem of Fig.25 is a uniform displacement field, with homogeneous strain. According to the material incompressibility and plane strain condition, the stretches in the 1, 2 and 3 directions, λ_1, λ_2, and λ_3 are such as:

$$\lambda_1\lambda_2 = 1 \qquad \lambda_3 = 1 \tag{9}$$

Using the constitutive equation (1), the stresses are

$$\sigma_{11} = \mu_0\lambda_1^2 - p = -P \tag{10}$$

$$\sigma_{22} = \mu_0\lambda_2^2 - p = 0 \tag{11}$$

$$\sigma_{33} = \mu_0 - p \tag{12}$$

By substracting (10) from (11), the applied stress P is:

$$P = -\mu_0(\lambda_1^2-\lambda_2^2) \tag{13}$$

Using the incremental constitutive relation (3), the increment of convected stress, which is Jauman's rate of Cauchy stress, is

$$\hat{\sigma}_{11} - \hat{\sigma} = 2\mu D_{11} \tag{14}$$

$$\hat{\sigma}_{22} - \hat{\sigma} = 2\mu D_{22} \tag{15}$$

$$\hat{\sigma}_{12} = 2\mu D_{12} \tag{16}$$

Since the material is incompressible $D_{11}+D_{22}=0$. $\hat{\sigma}$ is found by adding (14) and (15):

$$\hat{\sigma} = (\hat{\sigma}_{11}+\hat{\sigma}_{22})/2 \tag{17}$$

The modulus μ is

$$\mu = \mu_0 (\lambda_1^2 + \lambda_2^2)/2 \tag{18}$$

Biot derives the equilibrium conditions for the incremental stress field:

$$\frac{\partial\hat{\sigma}_{11}}{\partial x} + \frac{\partial\hat{\sigma}_{12}}{\partial y} - P\frac{\partial W_{12}}{\partial y} = 0 \tag{19}$$

$$\frac{\partial\hat{\sigma}_{12}}{\partial x} + \frac{\partial\hat{\sigma}_{22}}{\partial y} - P\frac{\partial W_{12}}{\partial x} = 0 \tag{20}$$

The constraint of incompressibility is satisfied by introducing a stream function $\varphi(x,y)$:

$$u_1 = -\frac{\partial \varphi}{\partial y} \qquad u_2 = \frac{\partial \varphi}{\partial x} \tag{21}$$

After some calculations, Biot found equations (19) and (20) become:

$$\left(\frac{\partial^2}{\partial x^2} + \frac{\partial^2}{\partial y^2}\right)\left((\mu - P/2)\frac{\partial^2 \varphi}{\partial x^2} + (\mu + P/2)\frac{\partial^2 \varphi}{\partial y^2}\right) = 0 \tag{22}$$

The usual solution of (22) is the uniform displacement field with homogeneous deformation. However there is a solution which is sinusoidal along the x direction and vanishes at infinite depth ($y=-\infty$):

$$\varphi = \frac{1}{l^2}(C_1 e^{ly} + C_2 e^{kly}) \sin lx \tag{23}$$

C_1 and C_2 are two constants, l is inversely proportional to length, and k is

$$k = \lambda_1/\lambda_2 \tag{24}$$

By enforcing the fact that the surface y=0 is free of stress, Biot finds that the solution (23) exists when:

$$\xi^3 + \xi^2 - 2 = 0 \quad \text{with} \quad \xi = (1-k^2)/(1+k^2) \tag{25}$$

which has one real solution $\xi = 0.839$ (k=0.295). The extension ratio corresponding to surface instability for this case is

$$\lambda_1 = 0.544 \tag{26}$$

and the applied compressive stress is

$$P = 3.08\ \mu_0 \tag{27}$$

APPENDIX B

ANALYTICAL SOLUTION OF THE RESPONSE OF AN HYPO-ELASTIC SOLID SUBJECTED TO FINITE PLANE STRAIN COMPRESSION

Consider the plane strain problem of Fig.26.

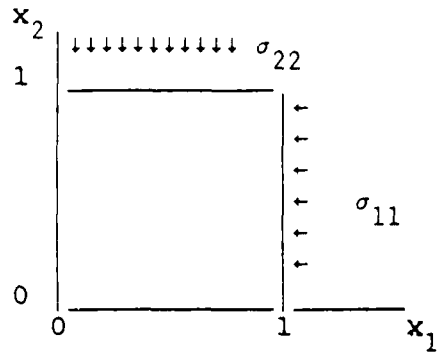

Fig.26. Block of finite size subjected to the wedge test.

The constraints imposed by the plane strain loading on the rate of deformation are:

$$D_{33} = D_{12} = D_{23} = D_{31} = 0 \qquad (1a)$$

$$W_{ij} = 0 \quad i,j=1,2,3 \qquad (1b)$$

The constitutive equation is expressed in term of the Jauman rate of Cauchy stress:

$$\hat{\sigma} = \mathbf{C}.\mathbf{D} - \sigma \, \mathrm{trace}(\mathbf{D}) \qquad (1c)$$

where σ is Cauchy stress, and **C** the constitutive matrix of transversely anisotropic elasticity, the plane of isotropy being normal to the x_2 direction. According to (1b) Jauman's rate is identical to the material time derivative

$$\hat{\sigma} = \overset{\circ}{\sigma} \tag{1d}$$

The general constitutive (1a) becomes:

$$\overset{\circ}{\sigma}_{11} = \frac{2G}{1-2\nu}((1-\nu)D_{11} + \nu D_{22}) - \sigma_{11}(D_{11}+D_{22}) \tag{2a}$$

$$\overset{\circ}{\sigma}_{22} = \frac{2G}{1-2\nu}(\nu D_{11} + (1-\nu)D_{22}) - \sigma_{22}(D_{11}+D_{22}) \tag{2b}$$

$$\overset{\circ}{\sigma}_{33} = \frac{2G}{1-2\nu}(\nu(D_{11}+D_{22})) - \sigma_{33}(D_{11}+D_{22}) \tag{2c}$$

$$\overset{\circ}{\sigma}_{12} = G_t D_{12} = 0 \tag{2d}$$

If the stress on the free surface $x_2=0$ remains equal to zero:

$$\sigma_{22} = 0 \quad \text{and} \quad \overset{\circ}{\sigma}_{22} = 0 \tag{3a}$$

then the relation (2b) reduces to:

$$D_{22} = \frac{-\nu}{1-\nu} D_{11} \tag{3b}$$

and the relation (2a) becomes

$$\frac{\overset{\circ}{\sigma}_{11}}{2G - \sigma_{11}(1-2\nu)} = \frac{D_{11}}{1-\nu} \tag{4}$$

The relation (4) can be integrated with respect to time t assuming that $\sigma_{11} = 0$ and $D_{11} = 0$ at time t =0

$$\int_0^t D_{11}\, dt = -\frac{1-\nu}{1-2\nu} \mathrm{Ln}\left(1-(1-2\nu)\frac{\sigma_{11}}{2G} \right) \tag{5a}$$

But the integral of D_{11} is related to the displacement in the x_1-direction u_1 which is zero at time t=0

$$\int_0^t D_{11}\, dt = \mathrm{Ln}(1+u_1) \tag{5b}$$

The material response is:

$$\sigma_{11} = \frac{2G}{1-2\nu}\left[1 - (1+u_1)^{-\frac{1-2\nu}{1-\nu}}\right] \tag{5c}$$

$$\sigma_{33} = \nu\, \sigma_{11} \tag{5d}$$

$$u_2 = -1 + (1+u_1)^{-\nu/(1-\nu)} \tag{5e}$$

Note that the material response is independent of the modulus G_t since there is no shear. The finite strain solution (5) is equal to the small strain solution if u_1 is small compared to 1

$$u_2 = -\nu u_1/(1-\nu) \tag{5f}$$

$$\sigma_{11} = 2Gu_1/(1-\nu) \qquad (5g)$$

The response given by equation (5) is plotted in Figs.3 and 27 for the following values of the shear modulus and Poisson's ratio: G=1, ν=0.3

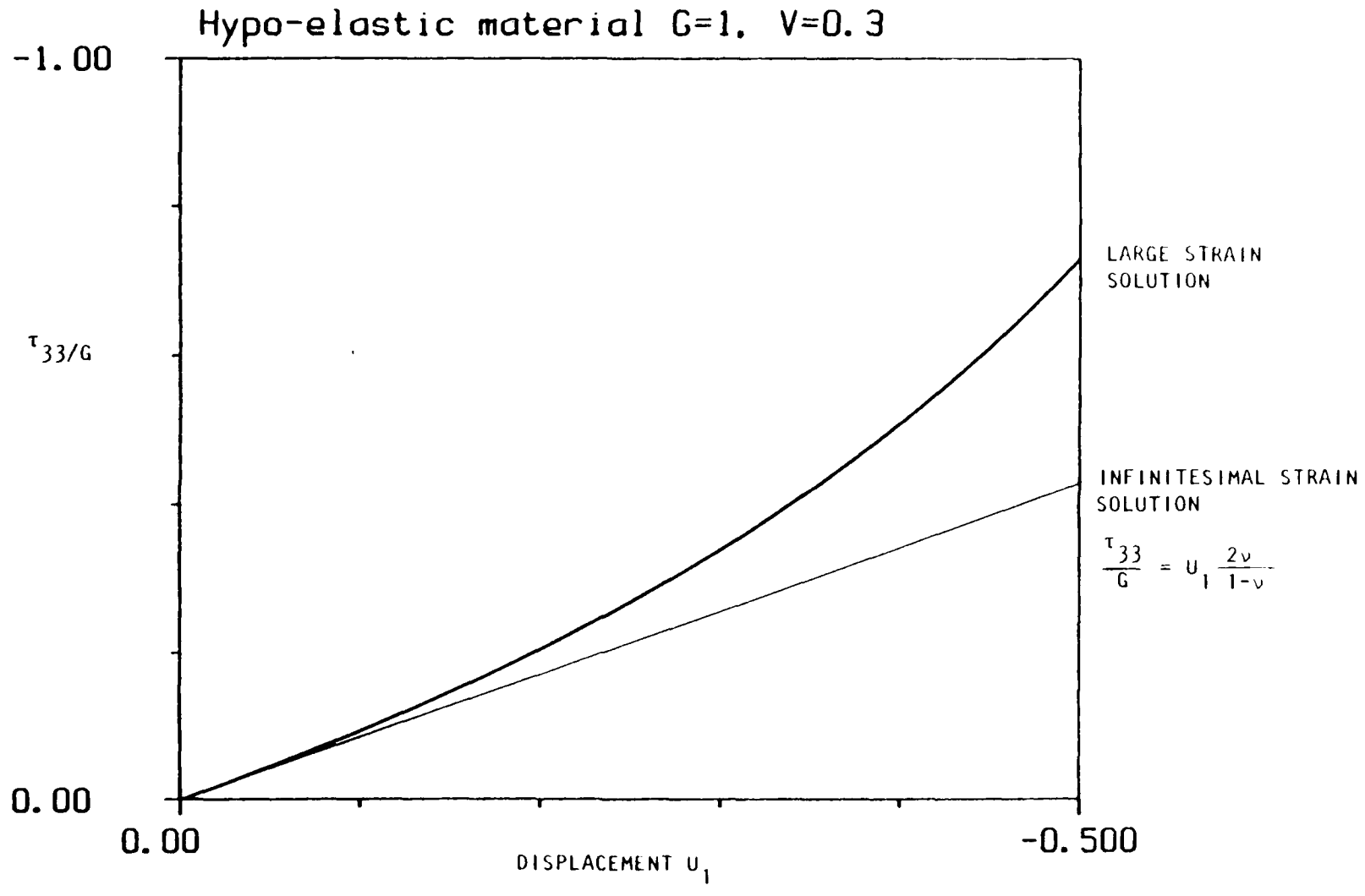

Figure 27a. Stress response of hypo-elastic material during the wedge test.

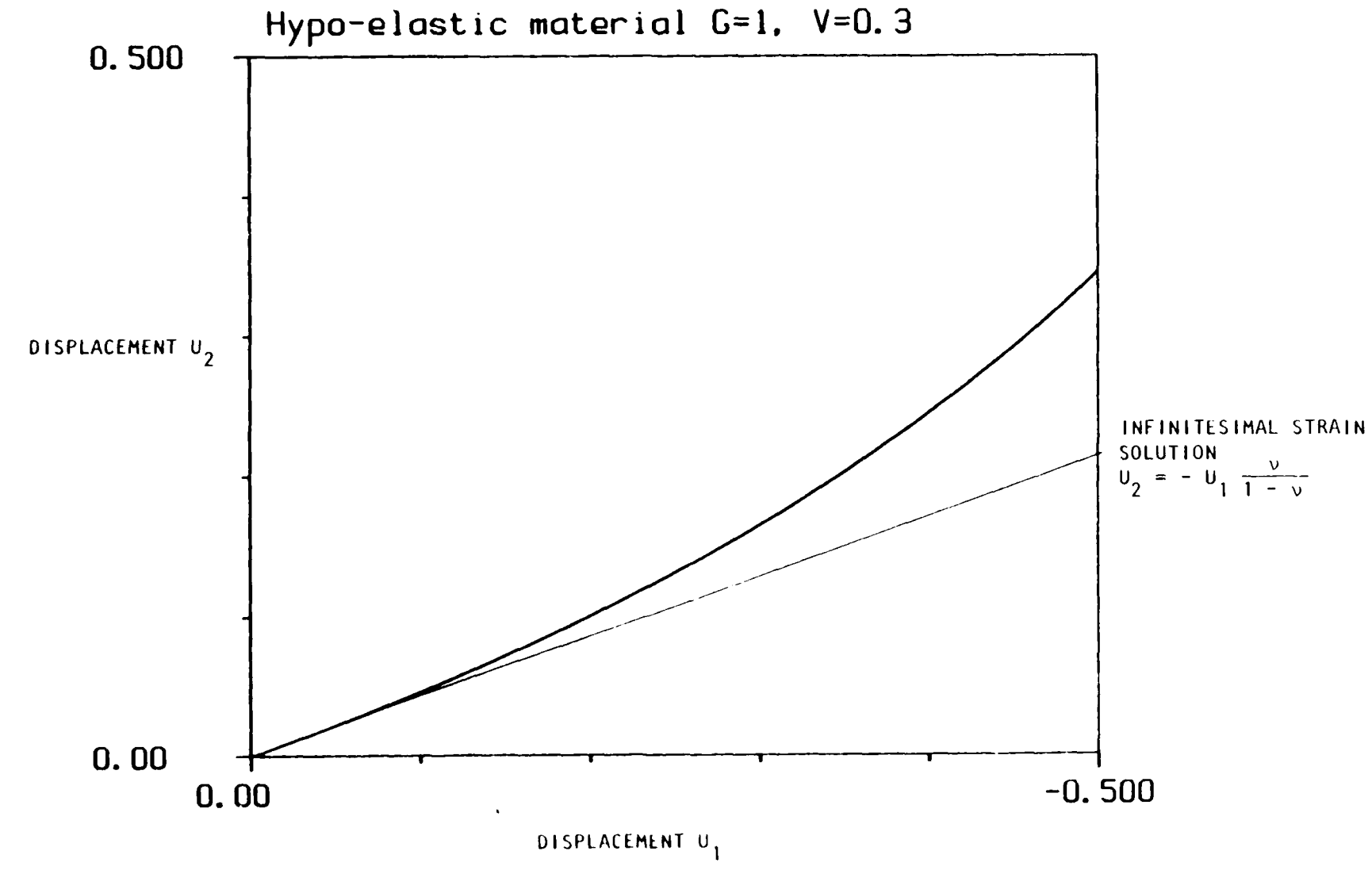

Figure 27b. Displacement response of hypo-elastic material during the wedge test.

DISTRIBUTION LIST

DEPARTMENT OF DEFENSE

DEFENSE INTELLIGENCE AGENCY
ATTN DB-6E2, C WIEHLE
ATTN RTS-2A (TECH LIB)
ATTN RTS-2B

DEFENSE NUCLEAR AGENCY
ATTN OPNA
ATTN OPNS
4 CYS ATTN SPSD
4 CYS ATTN TITL

DEFENSE TECHNICAL INFO CENTER
12CYS ATTN DD

FIELD COMMAND TEST DIRECTORATE
ATTN FCTBE/ L ASHBAUGH

DEPARTMENT OF THE ARMY

U S ARMY ENGINEER DIST OMAHA
ATTN MROED-S H (GAUBE)

U S ARMY ENGR WATERWAYS EXPER STA
ATTN D BANKS, WESGR
ATTN J JACKSON, WESSD
ATTN TECHNICAL LIBRARY
ATTN W MILLER

DEPARTMENT OF THE AIR FORCE

AIR FORCE OFFICE OF SCIENTIFIC RSCH
ATTN S WU

AIR FORCE WEAPONS LABORATORY
ATTN NTE
ATTN SUL

BALLISTIC MISSILE OFFICE
ATTN ENS
ATTN MY

HILL AIR FORCE BASE
ATTN TRW/DOC PROCESSING

DEPARTMENT OF ENERGY

LAWRENCE LIVERMORE NATIONAL LAB
ATTN L-53 TECH INFO DEPT LIB

LOS ALAMOS NATIONAL LABORATORY
ATTN J NEUDECKER
ATTN REPORT LIBRARY

OAK RIDGE NATIONAL LABORATORY
ATTN: CENTRAL RSCH LIBRARY

SANDIA NATIONAL LABORATORIES
ATTN: ED AND TECH LIB DIV

SANDIA NATIONAL LABORATORIES
ATTN: TECH LIB 3141 (RPTS RCVG CLK)

OTHER GOVERNMENT

CENTRAL INTELLIGENCE AGENCY
ATTN: OSWR/NED

DEPARTMENT OF THE INTERIOR
ATTN: TECH LIB

DEPARTMENT OF THE INTERIOR
ATTN: P SANDS

OFFICE OF TECHNOLOGY ASSESSMENT
ATTN: R STAFFIN

DEPARTMENT OF DEFENSE CONTRACTORS

AEROSPACE CORP
ATTN: LIB ACQUISITION M1/199

AGBABIAN ASSOCIATES
2 CYS ATTN: J P BARDET

ANALYTIC SERVICES, INC (ANSER)
ATTN: K BAKER

APPLIED RESEARCH ASSOCIATES, INC
ATTN: N HIGGINS

APPLIED RESEARCH ASSOCIATES, INC
ATTN: S BLOUIN

APPLIED RESEARCH ASSOCIATES, INC
ATTN M DAVISTER

APPLIED RESEARCH ASSOCIATES, INC
ATTN: R FRANK

BDM CORP
ATTN: F LEECH

BDM CORPORATION
ATTN: D BURGESS
ATTN: J MERRITT

BOEING CO
ATTN: H LEISTNER
ATTN: R J WOOD

CALIFORNIA RESEARCH & TECH, INC
ATTN: K KREYENHAGEN
ATTN: LIBRARY

FOSTER-MILLER INC
ATTN: W A. RIBICH/VICE PRES

H & H CONSULTANTS, INC
ATTN: E CORDING
ATTN: J HALTIWANGER
ATTN: J HENDRON

IIT RESEARCH INSTITUTE
ATTN: DOCUMENTS LIBRARY

INSTITUTE FOR DEFENSE ANALYSES
ATTN: CLASSIFIED LIBRARY

KAMAN SCIENCES CORP
ATTN: LIBRARY/B. KINSLOW

KAMAN SCIENCES CORPORATION
ATTN: DASIAC

KAMAN TEMPO
ATTN: DASIAC

MITRE CORPORATION
ATTN: TECH REPORT CENTER

NTS ENGINEERING
ATTN: R KENNEDY
ATTN: S SHORT

PACIFIC-SIERRA RESEARCH CORP
ATTN: A LAUPA
ATTN: H BRODE, CHAIRMAN SAGE

R & D ASSOCIATES
ATTN: J LEWIS
ATTN: TECH INFO CENTER

R & D ASSOCIATES
ATTN: D PIEPENBURG

RAND CORP
ATTN: P DAVIS

RAND CORP
ATTN: B BENNETT

S-CUBED
ATTN: R DUFF

SCIENCE APPLICATIONS INTL CORP
ATTN: M MCKAY
ATTN: TECHNICAL LIBRARY

SCIENCE APPLICATIONS INTL CORP
ATTN: TECHNICAL LIBRARY

SCIENCE APPLICATIONS INTL CORP
ATTN: W LAYSON

SOUTHWEST RESEARCH INSTITUTE
ATTN: A WENZEL

SRI INTERNATIONAL
ATTN: J COLTON

TERRA TEK, INC
ATTN: S GREEN

TRW INC
ATTN: TECH INFO CTR DOC ACQ

TRW SYSTEMS
ATTN: W WAMPLER

UTD, INC
ATTN: E FOSTER

WEIDLINGER ASSOC
ATTN: J ISENBERG

WEIDLINGER ASSOC, CONSULTING ENGRG
ATTN: M BARON

DISTRIBUTION LIST UPDATE

This mailer is provided to enable DNA to maintain current distribution lists for reports. We would appreciate your providing the requested information.

☐ Add the individual listed to your distribution list.

☐ Delete the cited organization/individual.

☐ Change of address.

NAME: _____

ORGANIZATION: _____

OLD ADDRESS	CURRENT ADDRESS
_____	_____
_____	_____
_____	_____

TELEPHONE NUMBER: ( ) _____

SUBJECT AREA(s) OF INTEREST:

_____ _____

_____ _____

_____ _____

DNA OR OTHER GOVERNMENT CONTRACT NUMBER: _____

CERTIFICATION OF NEED-TO-KNOW BY GOVERNMENT SPONSOR (if other than DNA):

SPONSORING ORGANIZATION: _____

CONTRACTING OFFICER OR REPRESENTATIVE: _____

SIGNATURE: _____

CUT HERE AND RETURN

END

DATE

FILMED

6-88

DTIC